

Particle Settling In Sheared non-Newtonian Fluids

*Submitted in partial fulfillment of
the requirements for the degree of*

Doctor of Philosophy

of the

Indian Institute of Technology Bombay, India

and

Monash University, Australia

by

Lavanya Sethuraman

Supervisors:

Prof. Shivasubramanian Gopalakrishnan (IIT Bombay)

Prof. Rajneesh Bhardwaj (IIT Bombay)

Prof. Murray Rudman (Monash University)

Dr. Andrew Chryss (CSIRO)



The course of study for this award was developed jointly by Monash University, Australia and Indian Institute of Technology, Bombay and was given academic recognition by each of them.

The programme was administrated by the IITB-Monash Research Academy

November 2019

© November 2019, by Lavanya Sethuraman

All rights reserved

Abstract

Many tailings slurries comprise of fine particles that are suspended in a carrier fluid. In concentrations levels that are high, the fines and water combine to form a non-Newtonian slurry. In a number of important applications, these slurries also contain larger, denser particles that are able to settle under shear. It results in inhomogeneity in the flow and can potentially significantly increase the pressure gradient required to drive it. A critical unanswered question is that of how the settling rate of large particles is related to the rheology of the fluid and the local shear in the vicinity of the particle. Although a small number of works on particle settling in non-Newtonian fluids exists in the literature, there is very little available on how imposed fluid shear modifies particle settling.

A computational fluid dynamics (CFD) model is developed that allows the prediction of the settling rate (and hence, the drag coefficient) for any particle size, density and fluid rheology. To validate the computational model, experimental measurements in a purpose-built shear rig were compared to the predictions of the settling rate by the model. Past findings about particle settling in unsheared and sheared mediums were compared and found to be in good agreement with the predictions. The CFD model is subsequently used to predict the settling rate across a wide range of particle sizes, densities and fluid rheologies (power-law and Herschel–Bulkley model).

In this numerical investigation, results are presented in two parts. In the first part, we considered the power-law fluids, and in the second part, we examined the fluid rheology that is fitted by Herschel–Bulkley fluids. The two parts are further divided into unsheared (or undisturbed) and sheared settling. The applied shear was increased to study the particle settling rate. The study is limited to the low-Reynolds number range ($Re \leq 1$), and a simple correlation that describes this relationship to accuracy is proposed. It can be used to predict the settling rate in simple laminar flows of power-law and yield stress fluids under unsheared and sheared conditions. This result has implications in the estimation of particle settling under transport and in the possible distance before complete stratification under laminar flow.

Declaration

I hereby declare that this thesis contains no material which has been accepted for the award of any other degree or diploma at any university or equivalent institution and that, to the best of my knowledge and belief, this thesis contains no material previously published or written by another person, except where due reference is made in the text of the thesis. This thesis includes one original paper published in peer reviewed conference. The core theme of the thesis is sheared settling in non-Newtonian fluids. The ideas, development and writing up of all the papers in the thesis were the principal responsibility of myself, the candidate, under the supervision of Prof. Murray Rudman and Prof. Shivasubramanian Gopalakrishnan. The inclusion of co-authors reflects the fact that the work came from active collaboration between researchers and acknowledges input into team-based research.

Lavanya Sethuraman

Date: 14 May 2020

(IITB ID: 134104001 Monash ID: 25557149)

Acknowledgements

I would like to thank IITB-Monash Academy and the Commonwealth Scientific and Industrial Research Organisation (CSIRO) for their financial support over the course of my PhD.

First and foremost, I would like to express my gratitude to my supervisors, Prof. Murray Rudman and Prof. Shiva Gopalakrishnan for their continued guidance, knowledge, and support, without which, this thesis would have been impossible. Working with them was an excellent learning experience.

A huge thanks to office mates, past, present and occasional for their much-needed help and support. I also thank Jane Moodie for her timely inputs on my technical writing and presentation skills. I would also like to thank all my friends for their support, through this time and many others. Special thanks to Sowmiya, Naresh, Jhumur, Sarang, Saurav, Bharat, Jagmohan, Thomas, Abinaya, Nia, Nithin and Rashmi for brightening up my PhD days. I would like to express my sincere gratitude to Swati for her encouragement and moral support to follow my yoga and meditation practices throughout my PhD journey. I extend my thanks to IITB Badminton club coach Shailender for training me and helping me see the sports in me. I also thank my badminton team friends Ishika, Vaishali, Vineet, Ankit, Aryan, Hrithik, and Atharv for their support during all the games.

Finally, my warm thanks to my parents, Sumathy and Sethuraman, for their unconditional love, encouragement and understanding me in all my endeavors. My sincere thanks to my brother, Senthil, and sister-in-law, Keerthi, for being supportive, when I was away from home. To my family and everyone mentioned here, I dedicate this thesis.

Contents

Acknowledgements	V
List of Figures	XI
List of Tables	XV
Nomenclature	XVII
1 Introduction	1
1.1 Overview of the thesis	2
2 Literature Review	3
2.1 Background	4
2.1.1 Rheology models	5
2.1.2 Choice of rheology	7
2.1.3 Single spherical particle	8
2.1.4 Drag coefficient	8
2.2 Particle settling in Power-law and Herschel–Bulkley fluids	9
2.2.1 Experimental studies	9
2.2.1.1 Bounded experiments	9
2.2.1.2 Unbounded experiments	10
2.2.1.3 Criterion for particle settling	11
2.2.1.4 Particle Interaction	11
2.2.2 Numerical studies	12
2.2.2.1 Yielded and unyielded region	13
2.3 Sheared settling	14

2.3.1	Sheared Newtonian fluid Stokes flow	15
2.3.2	Sheared settling in power-law and Herschel–Bulkley fluids	15
2.3.2.1	Experimental studies	15
2.3.2.2	Analytical study	16
2.3.2.3	Numerical study	16
2.4	Summary	17
3	Methodology	19
3.1	Governing equations for non-Newtonian fluids	20
3.2	The computational model	21
3.2.1	Setup for differences between unsheared and sheared cases	21
3.2.2	Boundary conditions	23
3.3	Archimedes number	24
3.4	Scaling analysis	25
3.5	Special cases in scaling	27
3.5.1	Case: 1 Scaling for plastic regime:	27
3.5.2	Case: 2 Scaling for Viscous regime:	28
3.5.3	Case: 3 Scaling for Intermediate regime	28
3.5.4	Case: 4 Scaling for imposed shear	28
3.6	Determination of settling velocity for a given $\Delta\rho$	29
3.7	Determination of particle rotation	30
3.8	Grid and domain independence	32
3.8.1	Grid generation	33
3.8.1.1	Grid resolution parameters	33
3.8.1.2	Number of surface cells	34
3.8.1.3	Expansion ratio	35
3.8.1.4	Setting up layers around the sphere	36
3.9	Mesh types	39
3.9.1	Levels of refinement	39
3.10	Grid resolution study at a different Re	41
3.11	Domain independence and grid resolution study for non-Newtonian fluids	42
3.12	Experimental methodology used by CSIRO	43

3.13 Summary	47
4 Settling in power-law fluid	49
4.1 Validation of unsheared power-law fluids	49
4.2 Validation of sheared power-law fluids	53
4.2.1 Validation of sheared settling with analytical prediction	53
4.2.2 Validation of sheared settling with experiments	55
4.3 Flow field	57
4.3.1 Unsheared settling	57
4.3.1.1 Flow separation	59
4.3.2 Sheared settling	61
4.3.2.1 Comparison between maximum and minimum Re / δ'	64
4.3.2.2 Effect of Reynolds number	65
4.3.2.3 Effect of imposed shear	67
4.4 Results	68
4.4.1 Non-dimensionalising imposed shear	68
4.4.2 Functional form for the settling rate in an unsheared medium	69
4.4.3 Functional form for the settling rate in a sheared medium	71
4.4.3.1 Ratio of sheared to unsheared settling velocity	72
4.4.4 Drag prediction	74
4.4.4.1 Drag prediction in the unsheared case	75
4.4.4.2 Unsheared Newtonian fluids	76
4.4.4.3 Unsheared power-law fluids	77
4.4.4.4 Sheared Newtonian fluids	78
4.4.4.5 Sheared Power-law fluids	79
4.5 Pressure and viscous force	83
4.5.1 Ratio of pressure to viscous force	86
4.6 Relationship between applied shear rate and ω	86
4.7 Comparison of results in terms of δ and δ'	88
4.8 Summary	89
5 Settling in Herschel–Bulkley fluids	91
5.1 Domain independence study	92

5.2	Critical particle size	94
5.2.1	Calculation of asymptotic force	95
5.3	Definition of Reynolds number	97
5.4	Flow field	99
5.4.1	Flow field under an unsheared condition	100
5.4.1.1	In terms of Herschel–Bulkley number	100
5.4.1.2	In terms of flow index	100
5.4.2	Flow field for sheared settling	102
5.5	Results	103
5.5.1	Unsheared settling	104
5.6	Drag prediction for sheared settling	105
5.7	Drag variation in terms of imposed shear	108
5.8	Drag variation in terms of Herschel–Bulkley number	112
5.9	In terms of flow index	113
5.10	Comparison with power-law results	113
5.11	Summary	115
6	Conclusions and Future Work	117
6.1	Future work	119
6.1.1	New rheology models	119
6.1.2	Orientation of planar shear/ geometry	119
6.1.3	Volume-fraction of solids	119
6.1.4	Unsteady flows	120
	Appendices	121
A	Appendix A	123
A.1	Expression for V_{Sh} for power-law fluids	123
A.2	Expression for V_{Sh} for Herschel–Bulkley fluids	124
A.3	Matlab code to determine V_{Sh} implicitly	125
A.4	Sample calculation to calculate $\Delta\rho$	126
	References	127

List of Figures

2.1	Different rheology models developed for non-Newtonian fluids	5
2.2	Coal (left) and copper (right) tailings depicts the highly viscous nature of the fluid V.Boger (2013).	7
2.3	Graphical representation of parameter space for mining slurries fitted to Herschel–Bulkley model	7
3.1	Schematic representation for unsheared settling	22
3.2	Schematic representation for sheared settling	23
3.3	Color code for domain walls’ boundary conditions demonstration in Table 3.4	24
3.4	Boundary conditions for each pair of domain walls.	24
3.5	Flow chart for determination of settling velocity for a given $\Delta\rho$	30
3.6	Flow chart for determination of particle rotation	32
3.7	Surface cells varied on the object-sphere (a) Coarse -200 cells (b) Medium-6000 cells (c) Refined -40,000 cells	34
3.8	Expanding of layers and total thickness (ΔL)	36
3.9	On the left image, zoomed view of the slice of 3D mesh used in the simulations. On the right, the layers around the particle surface widen according to the expansion ratio $r_e=1.3$	37
3.10	The grid resolution around the sphere was maintained constant and the box size was varied	38
3.11	Mesh type 1 - slice view: Level of refinement at 5 stages	40
3.12	Mesh type 2 -slice view : Intense refinement at a selected circular region - 2 times the particle diameter	41

3.13	Percentage difference with Stokes drag versus number of surface elements on the sphere, N_s	42
3.14	CAD drawing and photograph of the sheared settling rig developed at CSIRO.	44
3.15	Calibration curves for translating images to distance traveled. Both examples show high linearity, that is, no distortion with position.	46
4.1	Settling velocity as a function of density difference	51
4.2	Comparison with Graham and Jones (1994) for $0.2 \leq Re \leq 1$	52
4.3	Comparison of our numerical results with Dhole <i>et al.</i> (2006) for $5 \leq Re \leq 1$	52
4.4	Comparison of numerical results for $0.4 < n < 0.8$ with Childs (2013) for a range of $\Delta\rho$ (500 –4000)	55
4.5	Comparison between the experimental settling rate in sheared medium and that measured by the numerical study. Fluid rheology: $\tau_y = 9.76$ Pa, $k=2.41$ Pa s^n , $n=0.48$, $\rho_p = 8042$ kg/m ³ . The corresponding Re for the settling rate is denoted beside the solid marker.	56
4.6	Contours of y -component velocity for (a) $Re = 1$; $n=1$, (b) $Re = 1$; $n=0.5$, (c) $Re = 50$; $n=1$, and (d) $Re = 50$; $n=0.5$	58
4.7	Viscosity contours for $Re = 1$ (left) and $Re=50$ (right) for $n = 0.5$	59
4.8	Effect of Re on streamline contours for $n=0.5$ showing flow separation for higher values of Re	60
4.9	Flow separation map as a function of n and Re . Separated flow indicated by ‘o’ and the unseparated flows by ‘x’ at higher Reynolds number for various flow index.	61
4.10	Contours of (a) unsheared velocity y component (b) sheared velocity y component ($\delta' = 1$) (c) unsheared viscosity distribution (d) sheared viscosity distribution ($\delta'=1$) (for $Re = 1, n = 0.5$)	62
4.11	Velocity contour for $Re = 0.001$ and $Re=1$ at $\delta' = 1$ and $n = 1$	63
4.12	Velocity contour for $Re = 0.001$ and $Re=1$ at $\delta' = 1$ and $n = 0.9$	63
4.13	Velocity contour for $Re = 0.001$ and $Re=1$ at $\delta' = 1$ and $n = 0.7$	64
4.14	Velocity contour for $Re = 0.001$ and $Re=1$ at $\delta' = 1$ and $n = 0.7$	64

4.15 Comparison between contour of y - component of velocity at $Re=0.001$ and $Re=1.0$ for $\delta' = 0.1$	65
4.16 Comparison between contour of y - component of velocity at $Re=0.001$ and $Re=1.0$ for $\delta' = 1$	66
4.17 Comparison between contour of y - component of velocity at $\delta' = 0.1$ and $\delta' = 1$ for $Re=1$	67
4.18 Comparison with Dazhi and Tanner (1985) and our numerical measure- ments	70
4.19 Settling velocity as a function of density difference for different δ	72
4.20 V_{Sh}/V_U a function of δ (a) for flow index $0.3 < n < 1.0$ at constant $k=2.0$ (b) for $k=0.1$ and 2 Pas^n at constant $n=0.5$	73
4.21 Surface fit for V_{Sh}/V_U as a function of δ and n	74
4.22 X versus $\log Re$ for the range: $0.001 \leq Re \leq 1$	76
4.23 Comparison between predicted functional form in Equation 4.19 versus the numerical data for unsheared power-law fluid	77
4.24 Comparison between predicted the functional form in Equation 4.20 ver- sus the numerical data for sheared and unsheared Newtonian fluid	79
4.25 Comparison between the predicted functional form in Equation 4.25 ver- sus the numerical data for sheared and unsheared PL fluid $n = 0.9$	81
4.26 Comparison between predicted the functional form in Equation 4.25 ver- sus the numerical data for sheared and unsheared power-law fluid $n = 0.7$	82
4.27 Comparison between predicted the functional form in Equation 4.25 ver- sus the numerical data for sheared and unsheared power-law fluid $n = 0.5$	82
4.28 The prediction functional form for different conditions.	83
4.29 Predicted values of X/X_{Un} from Equation 4.25 versus actual values of X/X_{Un}	84
4.30 Z_p and Z_v values for $0.7 < n < 1$ under unsheared conditions	85
4.31 Z_p or Z_v values for for $n = 1, 0.9, 0.7$ and 0.5	86
4.32 C_p/C_v values for $n = 1, 0.9, 0.7$ and 0.5	87
4.33 Comparison between ω and $1/2(2W/D)$ -half the imposed shear for $0.001 \leq Re \leq 1$ and $0.5 \leq n \leq 1.0$	88

4.34 Comparison between the prediction in terms of δ (Eqn 4.13) and δ' (Eqn4.26)	89
5.1 Percentage difference of drag prediction with Tabuteau <i>et al.</i> (2007a) for increasing domain size.	92
5.2 Drag prediction for increasing domain size for yield-stress fluid $\tau_y = 8.133; k = 3.78; n = 0.373$ for imposed shear rate of $16.5s^{-1}$	93
5.3 Drag force asymptotes as the settling rate decreases for one mm particle for the fluid rheology, $\tau_y = 0.1 k = 0.1 n = 0.3$	96
5.4 Drag force asymptotes as the settling rate decreases for one mm particle for the fluid rheology, $\tau_y = 1 k = 0.1 n = 0.3$	96
5.5 Contour of y - component of velocity that represents the yielded and the unyielded regions for $n = 1.0$ and $n = 0.5$ for various HB covered in this study.	101
5.6 Contour of y - component of velocity that represents the yielded and the unyielded regions for range of n covered in this study at $HB = 10$	101
5.7 Contour of y - component of velocity for Bingham fluids for $0 \leq \delta' \leq 1$ at $HB=0.1$ and 10	102
5.8 Contour of y - component of velocity for $n=0.5$ for $0 \leq \delta' \leq 1$ at $HB=0.1$ and 10	103
5.9 Unsheared settling for various n and HB represented in terms of X/X_{Un} .	104
5.10 Comparison between model in Equation 5.12 and calculated data(*) . . .	106
5.11 Predicted values of X/X_{Un} from Equation 5.12 versus actual values of X/X_{Un}	107
5.12 Predicted values of X/X_{Un} from Equation 5.13 versus actual values of X/X_{Un}	108
5.13 Comparison between calculated data of X/X_{Un} and prediction model using Equation 5.13 for $n = 1.0$, various HB and δ'	109
5.14 Comparison between calculated data of X/X_{Un} and prediction model using Equation 5.13 for $n = 0.65$ and various HB and δ'	110
5.15 X/X_{Un} versus δ' for $0.1 \leq HB \leq 10$ for $n=1.0, 0.8, 0.65$, and, 0.5	111
5.16 X/X_{Un} versus HB for various δ' and n	112
5.17 $\log HB$ versus $\log X/X_{Un}$ for $n=1$ and $\delta' = 0 - 1$	113
5.18 X/X_{Un} versus n for $0 \leq \delta' \leq 1$ at various HB	114

List of Tables

3.1	Meshing input specification in OpenFOAM to increase the surface cells ranging between 200 -67000 cells	35
3.2	Layer thickness calculated using Equation 3.28 for a range of N_s studied .	38
3.3	Particle parameters used in the experiments.	45
3.4	Fluid rheology.	47
4.1	Value of fitting constants, α and β for the Equation 4.6 for various flow index given by Childs (2013)	54
4.2	The values of the drag correction factor X_{Un}	70
4.3	X_{Un} given by Dazhi and Tanner (1985) for unbounded flow	71
4.4	Fitting parameter β from the final functional form(Eqn 4.26 for varying power-law index n)	81
5.1	The values of the drag correction factor X_{Un}	99

Nomenclature

Greek Symbols

δ Dimensionless imposed shear scaled using unsheared settling rate

δ' Dimensionless imposed shear scaled using sheared settling rate

$\Delta\rho$ Density difference

Δ_n Layer thickness at the n^{th} layer on the particle surface

η, η_U Viscosity under unsheared conditions

η_{Sh} Viscosity under sheared conditions

ω Rotational velocity

ρ, ρ_f Fluid density

ρ_p Particle density

τ Shear stress

τ_y Yield stress

A Surface area of the spherical particle

Ar Archimedes number

Bi Bingham number

C_D Drag coefficient

C_p Pressure coefficient

C_v	Viscous coefficient
C_{St}	Stokes drag coefficient
D	Domain size
d	Particle diameter
$d_{critical}$	Critical particle size
F_B	Buoyancy force
F_D	Drag force
F_p	Pressure force
F_v	Viscous force
fLT	Final layer thickness
g	Acceleration due to gravity
HB	Herschel–Bulkley number
k	Consistency
L_s	Mean length scale
n	Flow index
N_s	Number of surface elements on the particle
r	Particle radius
r_e	Expansion ratio
Re	Reynolds number using power-law viscosity model
Re_{HB}	Reynolds number using Herschel–Bulkley model
V	Settling velocity
V, V_U	Unheated settling velocity

V_{sh}	Sheared settling velocity
W	Shearing wall speed
X	Drag correction factor
X_{Un}	Drag correction factor as a function of n
Y	Yield-gravity number
$\Delta\rho_{critical}$	Critical density difference
$\dot{\gamma}_T$	Total shear rate
$\dot{\gamma}_{applied}$	Applied shear rate
$\dot{\gamma}_{settling}$	Settling shear rate

Acronyms

CFD Computational Fluid Dynamics

Other Symbols

A', B, a, b, c, d, β Fitting constants

Chapter 1

Introduction

IN the mineral processing industry, the most common processes are grinding and milling of mineral ores. The mineral rocks are reduced to fine particles after they undergo various stages of crushing. In these processes, rock particles are usually mixed with a carrier fluid (normally water). This mixture moves through process equipment during processing. At this stage, when the mixture contains large rock particles, they are subjected to abrasion, chipping, compression, and most importantly, they accumulate inside the equipment. There would be significant cost reduction if there is a possibility to prevent the accumulation either by a pre-treatment to eliminate the stratified layer or by imposing an inlet force to the fluid medium so that it can prevent the particle from settling. However, the former (eliminating the stratified layer of settled particles) is preferred in mineral processing industries for two reasons. The first reason is the relatively low power consumption that is required to drive a homogeneous mixture. Secondly, there is a significant amount of mineral recovery when the stratified layer is recirculated to the initial stages of crushing. Prior to investigating the elimination of the stratified layer of large rock particles, a detailed understanding of particle motion in a slurry medium is crucial. In other words, information about how fast the large rock particles settle in the slurry medium is required initially to design the unit operation that would handle such complex slurries. Some of the specific applications that benefit from this current study are the transport of mine tailings in pipelines, removal of swarf in oil and gas well drilling, concrete pumping and transport of food materials with inclusions. Some of the suspensions of fine particles and slurries that is used in the mineral processing industries possesses non-Newtonian flow behaviour.

Large rock particles in the slurry medium respond differently to different shear rates; hence, an externally imposed shear is considered to impact particle settling. In slow settling particles, settling can be induced by imposing shear. This phenomenon is when there is an increase in the total shear rate around the particle. The orientation of the imposed shear also plays a prime role in influencing the particle settling. However, a planar shear along a Z-plane has been considered throughout the study. Through simulations, it is possible to determine whether the particle is influenced by the induced shear prior to being used in applications, which would save considerable time and money.

1.1 Overview of the thesis

The aim of this study is to demonstrate the settling particle in various complex rheologies and their associated flow fields that yield for different fluid rheology parameters, in particular settling in shear induced flows. This is achieved by solving a 3D computational model fluid flow by using the finite volume solver in OpenFOAM (open source CFD package). The solver predicts the settling velocity of the particle, and hence, its drag. This thesis begins with a review of the literature in Chapter 2, which is followed by a description of 3D model flows. The computational methods are described in Chapter 3 followed by results section.

Particle settling in non-Newtonian fluid that behaves as a power-law fluid is discussed in Chapter 4 in two categories. In the first category, particle settling in unsheared power-law fluid and the predictions by the model that are in accordance with the previous works. It was then extended to a wide range of rheology parameters related to mining slurries. Subsequent to that, in the second category, the investigation of particle settling in sheared power-law fluid and its predictions are discussed in Chapter 4.

Chapter 5 presents a study of particle settling in Herschel–Bulkley fluids, the critical particle size for settling and the settling behaviour under sheared conditions. The chapter also demonstrates that the unsetting particles begin to settle due to imposed shear. Finally, the key conclusions of this thesis and the future research directions are discussed in Chapter 6.

Chapter 2

Literature Review

NON-Newtonian fluids are identified by their complex fluid rheology. Several groups have studied particle transport in fluid flows in the past decades. The flow of past different bodies such as a sphere, a cylinder and an elliptical cylinder was studied to analyse the settling behaviour of such bodies and their interaction with other particles in the vicinity. The investigation commenced with an exploration of low Reynolds number flows and then used different non-linear viscosity models depending on the rheology of the fluid. New fluid rheology models which incorporate more fluid properties were developed (Shi and Napier-Munn (1996) and Wang *et al.* (2004)) for accurate prediction of fluid behaviour, which would lead to accuracy in the prediction of the particle settling.

The foundation of the fluid rheology is set by particle-particle and particle-fluid interaction and its inherent flow field during bulk flows. Although there are many rheology governing parameters, the non-Newtonian fluid flow attributes are characterized mainly into flow index (n), consistency (k) and yield stress (τ_y). For a range of low n ($0.1 < n < 1$), findings were recorded in the past (Chhabra *et al.* (1980)) and generally they observed that a particle settles faster than in Newtonian fluids. This is due to the increased strain rate around the particle, and hence has the ability to reduce its viscosity, allowing the particle to settle faster. Predictions in the past for a distinct range of Re are discussed in this chapter in detail in the order mentioned below.

After a brief introduction to the relevant background material in §2.1, the literature related to unsheared and sheared settling flows is discussed. Specific studies performed using analytical or experimental methodology can be categorised according to the rheol-

ogy model that is used to predict the viscosity of the fluid under flow. These categories will be discussed broadly in §2.2.

It will be shown that unsheared settling in power-law fluids and Herschel–Bulkley fluids are well understood since there is plethora of theory, experimental and numerical techniques that can be used to understand the particle settling in such fluids. On the contrary, there is lack of theory and a lack of knowledge of the mechanisms for sheared particle settling, which are more subsequential to settling. Only three citations on induced shear settling exist thus far, and they are reviewed extensively in §2.3.

2.1 Background

In the 1940s, it was observed that the viscous stress in a complex fluid depended non-linearly on the rate of deformation. Complex fluid flows have widespread applications in engineering and science, ranging from processes such as suspended food solid transport, drilling mud, concrete casting in natural phenomena such as debris flows and lava flows. Complex fluid flows can be present both in laminar and turbulent regimes. However, studies began with a simple laminar flow to illustrate the non-linearity and its interactions with different bodies. Due to the increased popularity of fluid applications, the phenomenon was analysed at a much deeper level through various experiments, and later on, through numerical techniques. Ever since then, research to discover more about complex fluid flows at different flow regimes and the interactions of those with other bodies has continued.

Different rheology models were brought up to the area of non-Newtonian fluids. The rheology model that depicts the fluids behaviour is discussed in §2.1.1. Out of the numerous rheology models, a few were found to be more prevalent in presenting the fluid rheology predictions. The two commonly generalised rheology models are Power-law and Herschel–Bulkley. These models exhibit the inherent fluid properties of most types of non-Newtonian fluids. This is due to the nature of the flow index: if their value is greater or lesser than one, it shows the shear-thickening or shear-thinning behaviour of the fluid. When fluids are highly viscous (when large particles are embedded in the fluid), they possess an inherent property termed ‘yield stress’. This property is accounted for in the Herschel–Bulkley model, it exists to be the primitive model, although many other

models were demonstrated to support the intrinsic changes in behaviour by adding an extra empirical constant into the functional form of the model.

2.1.1 Rheology models

A rheology model is used to predict the fluid behaviour and interactions of fluids such as mine tailings, oil and gas well drilling fluids, and other slurries, with other bodies. A detailed tabular representation of some of the most commonly used rheology models that were developed since 1920s is presented in Figure 2.1.

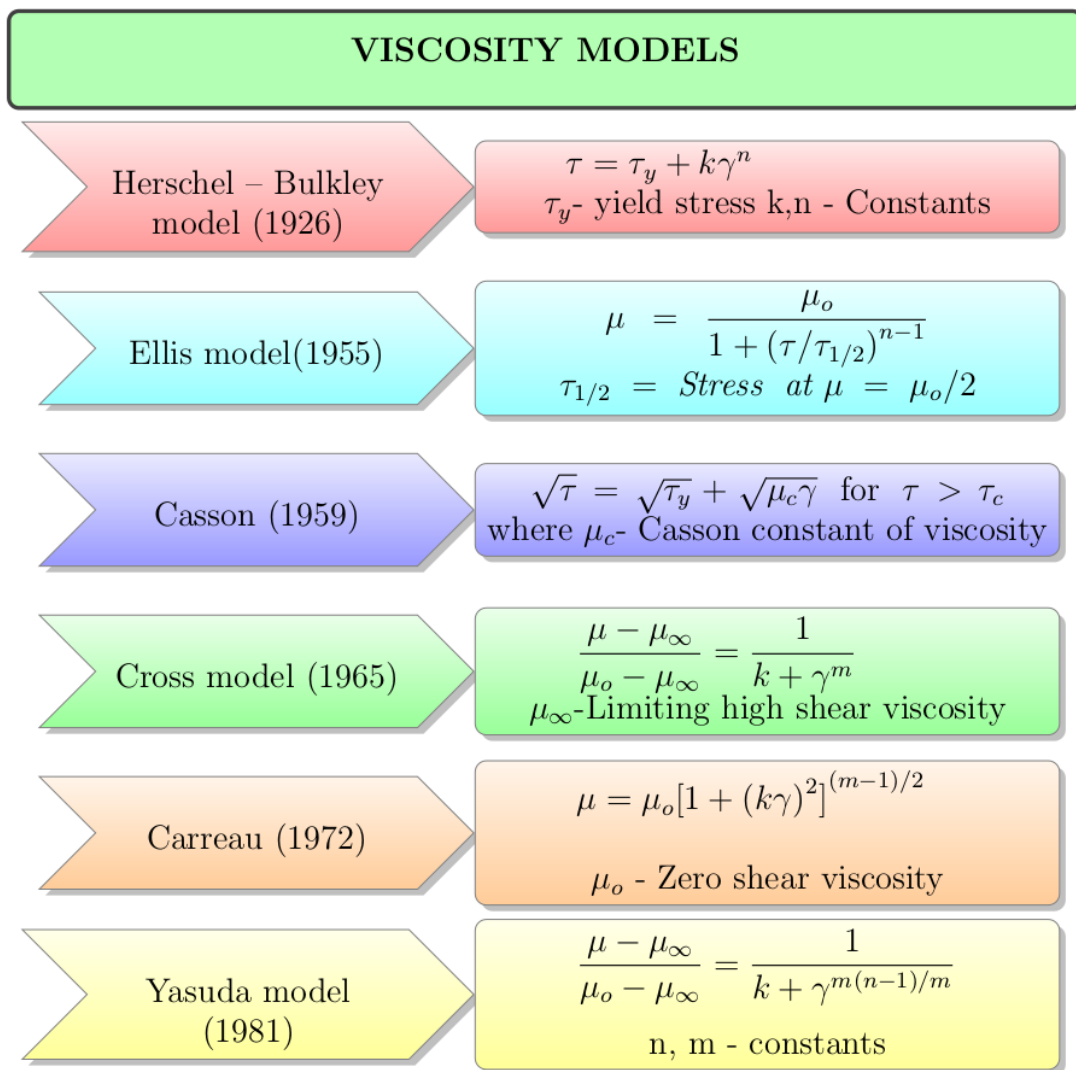


Figure 2.1: Different rheology models developed for non-Newtonian fluids

Comprehensive understanding has been gained on the flow behaviour of particles in the power-law, Ellis model and Carreau model fluids has been recorded by Wasserman

and Slattery (1964), Slatter (1997), and Chhabra *et al.* (1980), respectively. In this study, the non-uniform viscosity used are the power-law model (Eqn 2.1) and the Herschel–Bulkley model (Eqn 2.2), in which the shear stress is related to the strain rate through an effective viscosity η .

$$\eta = \frac{\tau_{ij}}{\dot{\gamma}_{ij}} = k\dot{\gamma}^{n-1} \quad (2.1)$$

$$\eta = \frac{\tau_{ij}}{\dot{\gamma}_{ij}} = \frac{\tau_y}{\dot{\gamma}} + k\dot{\gamma}^{n-1} \quad (2.2)$$

where k is the consistency, and n is the flow index. The second invariant of the rate of the strain tensor, $\dot{\gamma}$, is given by:

$$\dot{\gamma} = \sqrt{\frac{\dot{\gamma}_{ij}\dot{\gamma}_{ij}}{2}} \quad (2.3)$$

To illustrate the high concentration of solids in the flow behaviour of the fluids (typically thick pastes), various fluid models were developed to predict their behaviour. The most prominent fluid models are those that were developed by Bingham (1922), Herschel and Bulkley (1926), and Casson (1959). When thick slurries are subjected to shear stress up to a certain magnitude, their rate of deformation is zero. The threshold shear stress beyond which the fluid starts to move corresponds to the property termed yield stress. The fluid models mentioned feature this property and other rheological parameters such as consistency and flow index. Of all the models that have been proposed in the past, Slatter (1997) examined and found that the Herschel–Bulkley fluid model yields the best representation of the slurries.

The basic rheology model that was used to incorporate this property is the Herschel–Bulkley equation in which the viscosity is dependent on four parameters: τ_y , k , n and $\dot{\gamma}$. In simple shear flow, the Herschel–Bulkley equation takes the following form:

$$\tau = \tau_y + k\dot{\gamma}^n \quad \text{for } |\tau| > \tau_y \quad (2.4)$$

$$\dot{\gamma} = 0 \quad \text{for } |\tau| \leq \tau_y \quad (2.5)$$

where τ is the shear stress. The range for each of the parameters is discussed in the section below.

2.1.2 Choice of rheology

The type of fluid examined in this research work is mineral tailing. Some of the examples of the fluids considered in this study are coal tailings, gold tailings, nickel tailings and the like, which can be seen in Figure 2.2. Parameters of the Herschel–Bulkley model fitted to rheometrical data that were obtained for various mining slurries are illustrated below.



Figure 2.2: Coal (left) and copper (right) tailings depicts the highly viscous nature of the fluid V.Boger (2013).

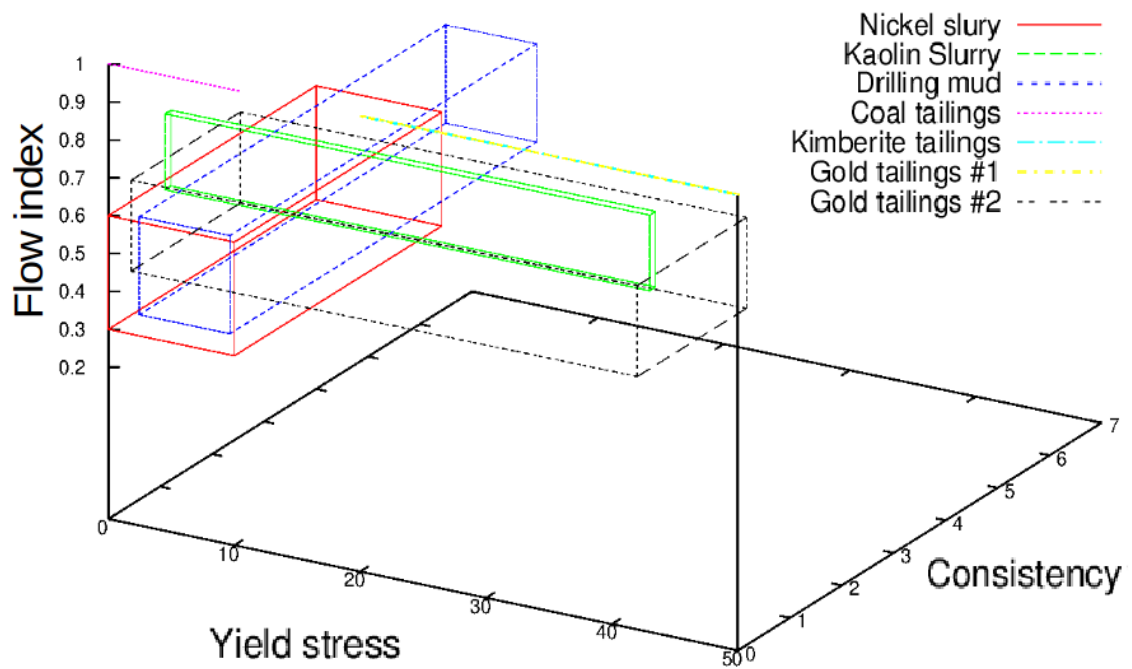


Figure 2.3: Graphical representation of parameter space for mining slurries fitted to Herschel–Bulkley model

The range for each parameter that relates to mining slurries such as bauxite tailings, red mud, uranium mill tailings, coal suspensions, fresh concrete, clay based tailings and the like was obtained from Bakker *et al.* (2009), Sofrá and Boger (2002), Turian *et al.* (2002), Mendes and Dutra (2019), Coussot *et al.* (1998), Bartosik (2010), Alehossein *et al.* (2012), and Nguyen and Boger (1998). From the rheology data, a range of parameters that covers a majority of these slurries are used in this study. As can be seen from Figure 2.3, the range of consistency (Pa s^n) is $0.1 < k < 2$, for flow index is $0.3 < n < 0.7$ and for yield stress $0 < \tau_y < 10$ (Pa).

2.1.3 Single spherical particle

Most studies to date have investigated settling characteristics of a spherical particle. However, certain studies have examined different shapes of a bluff body such as elliptical cylinders that have different aspect ratios along the horizontal and vertical axes. Although there is potential for the study of sheared settling in particles of different aspect ratios, we begin with a spherical particle to understand the fundamental physics of settling in non-Newtonian fluids. Therefore, the current study focuses on the spherical particle, the findings for which are reported in this thesis. Before finite volume fractions can be considered, the underlying physics of an isolated particle must be characterised. Hence, studies of an isolated particle are reported in this chapter.

2.1.4 Drag coefficient

An elementary hydrodynamic property to investigate the motion of particle settling is the drag coefficient, C_D . A detailed understanding of C_D is of utmost importance in terms of theoretical and practical value, because it allows the prediction of terminal falling velocities, V , for a fluid of any rheology.

The Drag, F_D , on a sphere in a quiescent fluid was first examined by Stokes, which lead to the familiar result that is presented through Equation 2.6. Stokes' result is valid only in an unconfined/unbounded fluid medium and a slow Newtonian flow ($Re \rightarrow 0$, that is, Stokes flow).

$$F_D = 3\pi d\eta V \rightarrow C_D = \frac{24}{Re} \quad (2.6)$$

However, in the current case, we are considering non-Newtonian fluid in non-creeping flow regime in a confined fluid medium. The relationship between C_D and Re in the case that was considered in this study cannot have a simpler correlation. Therefore, in this thesis, the drag coefficient for each case (including imposed planar shear conditions) is treated as the core property for the prediction of particle settling.

2.2 Particle settling in Power-law and Herschel–Bulkley fluids

A large array of literature has been presented from studies about particle settling in non-Newtonian fluid flows. Drag correlations that are available in the literature can be divided into studies that use numerical, analytical, and experimental methods. Scientific findings that use these methods are discussed below in §2.2.1 and §2.2.2

2.2.1 Experimental studies

Particle settling is influenced by various parameters such as domain size, fluid rheology and particle material property (density, porosity etc). Usually, the settling predictions were found for unbounded domain or negligible effects on the wall. Of the dimensionless parameters, the domain size is unaccounted for. Therefore, the results are presented in-terms for distinct domain sizes, and we notice the manner in which the drag coefficient varies due to the effect of confining walls. The experimental approach is discussed in the sections below in two categories, in the presence and absence of wall effects.

2.2.1.1 Bounded experiments

In a finite domain, the fluid flow is hampered. There is a backward movement of the fluid due to the entrainment effect near the particle combined with viscous friction near the boundary walls. The backward movement drastically slows down the settling speed of the particle (Song and Gupta (2009)).

Some researchers from those who have described drag on spheres in non-Newtonian fluids, have ignored the effect of domain walls, while others have insisted that the same wall correction are pertinent only only to Newtonian fluids.

A well known early study by Valentik and Whitmore (1965) measured the terminal velocities of spheres falling in clay suspensions. The study also applied corrections to the retarding effect of the walls of the containing vessel. Other early studies have been those by Ansley and Smith (1967a)

Apparently when a particle is settling in a narrow column or a small width channel, the fluid is pushed upwards along the side of the column that is subjected to extra frictional force (Lali *et al.* (1989)). However, Chhabra (2006) points out from his works that the wall effect considerably decreases as Re increases.

In this context, Andres (1961) consolidated a review of studies that deal with this phenomenon of unbounded and bounded solutions. He proposed a relationship to determine the wall correction factor on the settling velocity of particles. Felice and Parodi (1996) also developed a model for a similar case. However, this model depends on the Reynolds number and on the ratio between the particle size and the settling fluid medium. As an extension to this model, Kelessidis (2004) further investigated the development of an estimate for the error in the particle settling speed due to the entrainment effect that is induced by the wall; the magnitude was found to be approximately 5.5%. Additionally, cha (1980) predicted that, in an extreme case, the error could reach as high as 7%.

Apart from the wall correction factor, Andres (1961) also showed that for a particle to settle in a highly viscous fluid, its buoyant weight has to exceed the yield stress of the fluid. The applicability of this theory was reviewed both experimentally and theoretically by various researchers such as Boardman and Whitmore (1961) and Brookes and Whitmore (1968). Later, experimental studies were carried out by Graham and Jones (1994), Atapattu *et al.* (1995a) and Chhabra (2006). They predicted the settling velocities in undisturbed Bingham-plastic fluids. Additionally, the experimental works by Atapattu *et al.* (1995a) has yielded useful insights, particularly ,into the wall effects, drag behaviour, and the sizes of yielded and unyielded region in the case of the yield stress fluids.

2.2.1.2 Unbounded experiments

In an infinite media, particle motion is unhampered and particle settling induces velocities at every point of a fluid in the same direction as a result of which the entraining effect completely disappears.

Wall effects disappear completely when the value of (D/d) is beyond a certain critical value. The value was found to be about two times the size of the sheared zone that was normalised with respect to the particle diameter.

Atapattu *et al.* (1995b) summarised that wall effects were minimised by maintaining a D/d ratio greater than 15. Tabuteau *et al.* (2007a) also confirmed the magnitude of the ratio through their experiments. Additionally, it has been shown that the wall effects diminish with an increasing pseudo-plastic behaviour (increasing yield stress) Missirlis *et al.* (2001).

Although the extent of the wall effects on a sphere settling in shear-thinning fluids in cylindrical tubes even in creeping flow conditions is not very strong, it cannot be neglected. Therefore, an unbounded experiments for a wide lower and upper range of Reynolds number has been reported in the literature. At a broader perspective, in an unlimited domain, the terminal settling speed is relatively greater than that in a column.

2.2.1.3 Criterion for particle settling

It has been observed in the case of yield stress fluid, the rate of deformation is zero when the fluid is subjected to shear stress that is lower than the yield stress value. Here, the particle is embedded in the fluid without movement. There is a critical weight or size of the particle at which its own weight can exceed the yield stress of the fluid and begin to move.

Dedegil (1987) and Jossic and Magnin (2009) looked at the critical particle size. They measured the drag force that is exerted on objects in a yield stress fluid when the velocities become infinitely slow where the yield stress effects are predominant. On the basis of these results, a critical criterion is proposed for the object in the fluid, to estimate the yield stress that is needed to balance buoyancy force. On the contrary, Beris *et al.* (1985) and Blackery and Mitsoulis (1997) proposed a different critical criterion through numerical simulations. This stability criterion was found to be in good agreement with experimental works by Tabuteau *et al.* (2007a).

2.2.1.4 Particle Interaction

Merkak *et al.* (2006) provided data on the interactions between two spheres (of the same diameter), which move at very low velocity in a yield stress fluid. Other recent innovative

experimental studies conducted in this field examine the way the falling spheres interact with each other (Tran and Horsley (1993); Liu *et al.* (2003); Wilson *et al.* (2003); Horsley *et al.* (2004); and Gumulya *et al.* (2007)). In these studies, the drag force on two moving spheres was examined as a dependent variable of the distance between the two particles. These studies concluded that the degree of particle interaction increases more in the case of an increase in the viscoplastic behaviour.

2.2.2 Numerical studies

Under numerical investigation, a majority of the studies reported predictions for the unbounded medium either by considering a domain independence study or using the critical ratio of the particle to the domain size as defined by Atapattu *et al.* (1995a).

Numerical simulations were used to study the detailed flow field that surround a falling particle (Blackery and Mitsoulis (1997); Beaulne and Mitsoulis (1997)). The experimental works of Atapattu *et al.* (1995a) were compared with a numerical simulation of these flows by Beaulne and Mitsoulis (1997), and it was found that there was agreement between the numerical and experimental data.

Missirlis *et al.* (2001), and Beris *et al.* (1985) have examined the experimental measurements and followed their results with numerical simulations. Missirlis *et al.* (2001) compared with Dazhi and Tanner (1985), Cho and Hartnett (1983) and Wasserman and Slattery (1964) and found to be in good agreement with their drag prediction.

Reynolds and Jones (1989), Graham and Jones (1994), Atapattu *et al.* (1995a), and Dazhi and Tanner (1985) have reported correlations that predicts the terminal velocity of spheres in power-law fluids. On the contrary, Wilson *et al.* (2003) resolved for non-Newtonian materials a new curve that is used with an ‘equivalent Newtonian viscosity’, which would produce the same particle terminal velocity.

In yield-stress fluids, numerical studies show that the creeping motion of a particle in an unbounded Bingham fluid (yield stress with constant viscosity and no thixotropy), there is an envelope of fluid whose size depends on the yield stress value of the fluid. The envelope of fluid is due to the confined flow around the surface of the particle. In the zone outside the envelope, the stress is smaller than the yield stress and hence, the fluid does not move. This zone is known as the unyielded region. A detailed insight on the size

of the unyielded/ yielded region for Bingham and yield stress fluids is discussed in the section below.

2.2.2.1 Yielded and unyielded region

From the yield stress fluids, the motion of a particle causes certain changes in the molecular structure of the fluid when under stress. This molecular distortion in the fluid medium results in the coexistence of solid-like zones at a macroscopic level. The solid-like zones are known as the ‘unyielded region’ in the fluid domain. Therefore, in the velocity contours, distinct zones of yielded and unyielded regions are seen.

The yielded and unyielded regions vary according to the yield stress property of the fluid. The aspects of the unyielded region in the fluid medium were primarily addressed by Chhabra in 1995 through his experiments, and it was then investigated through computational studies by Taibi and Messelmi (2018).

Chhabra showed the shape of the yielded region depends on both the sphere to column diameter ratio as expected and the variations in the viscosity with the shear rate. For particle settling in yield stress fluid, it is found that unyielded region appears on both sides of the particle.

Putz *et al.* (2008) conducted a computational study to understand this behaviour by using polymeric shear thinning yield stress fluids. It has been found that the size of the yielded region is inversely proportional to the yield stress.

$$HB = \frac{\tau_y}{k\dot{\gamma}^n} \quad (2.7)$$

$$Bi = \frac{\tau_y}{k\dot{\gamma}} \quad (2.8)$$

The dimensionless approach of representing the yield stress property of the fluid is referred to as the Herschel–Bulkley number (HB). If the shear thinning behaviour is absent i.e., $n = 1$, it is referred to as the ‘Bingham number (Bi)’ (described in Equation 2.7 and 2.8). Generally, the dimensionless parameters that govern the flow are obtained by considering scaling analysis of the governing partial differential equations and using its appropriate non-linear viscosity function (rheology model). In all the past studies, the results were represented in terms of Re , C_D and Bi or HB . For dealing with yield stress

fluids settling measurements representation, Ansley and Smith combined two dimensionless groups - Re and Bi to a single parameter , Q^* as:

$$Q^* = \frac{Re}{1 + kB_i} \quad (2.9)$$

The value of constant k has been postulated to be unity for Bingham fluids. Later, the values of k are presented based on the blockage ratio of the fluid domain. For an unbounded medium, the value of k for shear thinning-yield stress fluids was given as 0.818 by Atapattu *et al.* (1995a).

It has been reported and confirmed through experimental measurements that the size of the unyielded surface increases with increasing Bi or HB . Increasing unyielded region proves the diminishing viscous deformation induced in the flow. Therefore, it is demonstrated that unyielded region around the particle surface implicate the zero shear or the rest region. However, if we apply shear, the unyielded region shrinks and disappears due to the viscous deformation throughout the fluid domain.

2.3 Sheared settling

Particle settling under gravity in various non-Newtonian fluids is well explored, and several studies are recorded in the past. However, particle settling under ‘induced shear’ has been addressed by less than a handful of researchers in the past. The idea of that imposed shear on the fluid medium distorts the fluid viscosity around the particle surface and allows the particle to settle even faster. Gheissary and van den Brule (1996) addressed the manner in which the total shear rate can be written for a particle settling under induced shear.

The total effective shear rate was defined to incorporate the imposed shear rate. The total shear rate is the superimposition of the settling shear rate and shearing plane shear rate. The orientation of the imposed shear could act on the particle in fluid differently (planar shear imposed oriented either orthogonal or non-orthogonal to the settling direction). Experiments have not investigated the shift in Re and its corresponding drag based on the imposed shear (which is the focus of the current work). Some of the other recent relevant findings recorded are discussed in this section in the following order.

- Sheared Newtonian fluid Stokes flow

- Sheared settling in power-law and Herschel–Bulkley fluids

2.3.1 Sheared Newtonian fluid Stokes flow

In 1906, Einstein addressed the shear flow of a single, non-Brownian, inertia-less and buoyancy-free sphere in an infinite Newtonian fluid medium. In shear flow the particle rotates at a speed, ω , which is a function of the applied shear rate, $\dot{\gamma}_{applied}$. The functional relation for ω is given by Equation 2.10.

$$\omega = \frac{\dot{\gamma}_{applied}}{2} \quad (2.10)$$

Trevelyan and Mason (1951) and Avino and Maffettone (2015) confirmed experimentally that the constant angular velocity of spherical particles, which is proportional to the shear rate, is independent of particle size, and is in excellent accord with theory proposed by Einstein (1906).

The result was derived from zero net torque on the sphere surface due to the steady state flow. After several experiments, it has been found that the relation between ω and the applied shear rate ($\dot{\gamma}_{applied}$) is in agreement with the theoretical prediction given in Equation 2.10. As a consequence of the reversibility of the Stokes equations, symmetric streamlines were observed throughout the flow. In addition, the velocity profile appeared symmetric due to a set of closed orbits around the sphere.

2.3.2 Sheared settling in power-law and Herschel–Bulkley fluids

2.3.2.1 Experimental studies

Godinez *et al.* (2014) considered the case of a rotating and a settling particle in yield stress fluids. Rotation was induced magnetically in his experiments. The superposition of two shear rates from particle settling and rotation has been given by Godinez *et al.* (2014). Experimental investigation by imposing shear were conducted to determine the rheology of the fluid, particularly to predict the shear thinning or shear thickening fluid and the value of the consistency. This study was most relevant to our research work. It was relevant due to the fact that the viscosity around the particle vicinity is changed through externally/magnetically induced particle rotation. In such a setup, the flow around the sphere is given by the combination of the motion that is produced by translation or by

the rotation of the particle. Therefore, the resulting effective viscosity around the particle surface is the lowest and it gradually increases as we move away from the particle. The drag decreases as a result of the low viscosity region around the particle surface, the particle in turn settles faster in the fluid. Hence, the translating rotating particle settled faster in a shear thinning fluid.

Dazhi and Tanner (1985) and Snijkers *et al.* (2009, 2011) addressed the superposing rotation and translation in shear thinning fluids. Although, this experiment was conducted to act as a rheometer for power-law fluids, the correlation between the drag coefficient, the Reynolds number and flow index is not completely explored for non-Newtonian fluids of all flow regimes.

Herschel–Bulkley fluids were investigated for its particle settling flow under sheared conditions by Ovarlez *et al.* (2012) through experiments. They studied how induced shear can increase the settling rate in these type of fluids by inducing magnetic rotation to the spheres that are sedimenting in a Couette geometry. A background simple shear flow of a Herschel–Bulkley fluid could induce settling in systems that were at rest in the quiescent case, and that the settling velocity increased with the background shear rate.

2.3.2.2 Analytical study

Under the assumption of negligible inertial effects, the case of particle settling within a background simple shear flow of a power-law fluid was examined by Childs (2013). The problem was analytically solved by using a three-dimensional pseudospectral method. The particle settling velocity was found to have two distinct dependencies on the dimensionless parameters of the flow, corresponding to regimes of a dominant background shear flow or gravitational settling force. The results suggested an empirical settling law, for the settling velocity of a spherical particle within a background simple shear flow.

2.3.2.3 Numerical study

Thus far, no work has used a numerical approach, and our current work aims to fill this gap in the literature. The delineation of the different flow regimes under sheared conditions is reported in this study. The functional form of the drag coefficient is well understood in the case of sheared shear-thinning and yield stress fluids. Additionally, direct influences

of imposed shear and, in particular, the values of critical Reynolds numbers denoting the onset of the separation of flow are reported in this work.

2.4 Summary

For unsheared particle settling, extensive results on drag, surface pressure distribution, and streamline patterns have been discussed. In the past, the drag coefficient at different flow regimes was presented. These observations are also consistent with the experimental and numerical findings.

For sheared particle settling, there are a limited number of studies. Only three (Ovarlez *et al.* (2012); Childs (2013); Godinez *et al.* (2014)) discuss the increase in the particle settling velocity due to the applied shear. Although all these researchers examined sheared settling for different applications, they reported an increase in settling velocity due to increased shear and lower viscosity. However, the drag behaviour with respect to Reynolds number was not discussed in any work.

In our numerical study, we aim to bridge the gap and extend the literature to present a drag coefficient on the sheared particle that has never been examined before, to our knowledge.

Chapter 3

Methodology

EXPERIMENTAL measurement of settling in sheared non-Newtonian fluids is difficult for a number of reasons. In this thesis, the open source computational fluid dynamics (CFD) tool - OpenFOAM was chosen to simulate the settling. CFD provides the ability to theoretically simulate any physical condition. CFD allows great control over the physical process, and provides the ability to isolate specific phenomena for study. The basic concept in the physical interpretation is the subdivision of the mathematical model into non-overlapping components of simple geometry called finite volumes. The response of the mathematical model is then considered to be approximated by that of the discrete model that is obtained by connecting or assembling the collection of all elements. However, this approximation is normally considered representative enough for most systems and physics. CFD methodologies required to solve the particle settling in sheared non-Newtonian fluid is discussed in this chapter.

The development of the CFD model in OpenFOAM requires a number of utilities that could identify the rotation and the settling rate of a particle. A numerical algorithm was newly developed in order to determine the particle rotation in non-Newtonian fluids. This algorithm was used along with the CFD model to solve the problem of particle settling under a sheared fluid medium. The model was first developed for unsheared particle settling to investigate its efficacy and accuracy. The model was validated by comparing it with the previously published predictions for particle settling in non-Newtonian fluids.

After rigorous validation for the unsheared case, the model for the sheared case was developed by adding a planar shear boundary condition. A review of the literature showed that little or no quantitative experimental data was available to validate the model

in the sheared case. However, the model was validated against the available analytical solution for sheared power-law fluids under negligible inertial effects Childs (2013). In yield-stress fluids, the model was validated using experimental measurements (conducted by CSIRO, Australia) in a purpose-built shear rig. Predictions of the settling rate by the CFD model were compared to the experiments by CSIRO. Once the confidence in the model is developed, useful predictions about the flow behaviour in different cases can be presented.

3.1 Governing equations for non-Newtonian fluids

In an incompressible laminar flow of a non-Newtonian fluid, the equations of motion are the continuity and momentum equations.

$$\frac{\partial u_i}{\partial x_i} = 0 \quad (3.1)$$

$$\rho \frac{\partial u_i}{\partial t} + \rho \frac{\partial (u_i u_j)}{\partial x_j} = -\frac{\partial p}{\partial x_i} + \frac{\partial \tau_{ij}}{\partial x_j} \quad (3.2)$$

$$\tau_{ij} = \eta(\dot{\gamma}) \dot{\gamma}_{ij} \quad (3.3)$$

$$\dot{\gamma} = \sqrt{\frac{1}{2} \dot{\gamma}_{ij} \dot{\gamma}_{ij}} \quad (3.4)$$

where u_i is the component of the velocity in the x_i -direction, ρ is the fluid density, η is the effective viscosity, p is the pressure and τ_{ij} is the stress tensor. The rate of deformation tensor is $\dot{\gamma}_{ij}$, and it is equal to $\nabla u + \nabla u^T$. The challenge in the modeling of non-Newtonian flows is the absence of a simple linear relationship between the stress and strain rate of the fluid. The rheology model that is used to specify the non-Newtonian fluids that are used here is the Herschel–Bulkley model, in which the effective viscosity is

$$\eta = \tau_y / \dot{\gamma} + k \dot{\gamma}^{n-1} \quad (3.5)$$

where τ_y is the yield-stress of the fluid, k is the consistency and n is the flow index. When the yield-stress is zero ($\tau_y = 0$), the fluid is referred to as a power-law fluid. The equations of motion (Eqn. 3.1 and 3.2) are solved using the finite-volume-based-solver, *simpleFoam*, which is a branch of OpenFOAM 3.1.0. SimpleFoam is a steady-state solver

for an incompressible, turbulent flows, and it uses the SIMPLE (Semi-Implicit Method for Pressure Linked Equations) algorithm to solve the momentum and pressure equations.

3.2 The computational model

The aforementioned differential equations have been solved using a finite-volume–based solver, OpenFOAM. The factors required to set up the numerical solution methodology for particle settling in sheared non-Newtonian fluids is discussed in this section. To set up a numerical model for particle settling in sheared non-Newtonian fluids in OpenFOAM, certain assumptions need to be made about our model. We setup the model as a single sphere settling in a cubical box which acts the fluid domain. Here the sphere represents the particle in the fluid. It is not possible to simulate particle settling in an infinite medium; therefore, a finite domain must be chosen. We consider the problem of particle settling in an unbounded medium by using the approximation of a single sphere at the centre of a cubic box that as a side length of D . The box and sphere are idealised to the domain size and the particle, respectively. For the settling problem in the computational setup, a frame of reference is usually attached to the domain boundaries, for which a complex moving mesh has to be considered. To reduce computational complexity, the analogy is reversed. We perform the simulation in a frame of reference that is attached to the particle; thus, the boundaries of the box move upwards with respect to the stationary particle. When we change the frame of reference to be set on the particle, the particle is stationary and the boundaries of the box move upwards. The boundaries of the box are defined as moving non-slip boundaries that will simulate fluid flow around the sphere. The sphere is then assumed to have this moving boundaries' velocity as the settling velocity of the particle. The boundaries that do not move are defined as 'periodic boundaries' which implies that the continuity of fluid flow between opposite boundaries is maintained. This model would duplicate realistic conditions, which would be experienced when particles fall in a non-Newtonian fluid.

3.2.1 Setup for differences between unsheared and sheared cases

Figure 3.1 shows a schematic representation of the computational setup for a un-sheared settling problem. The left and right (x) boundaries of the box are defined as

no-slip boundaries that move vertically (y -direction) with a speed equal to the settling velocity V . This will drive a flow around the sphere, which is equivalent to the flow due to particle settling. However, V is the settling velocity we seek in the first place; hence, an algorithm to identify the settling velocity for a given particle density is required, and it is discussed below.

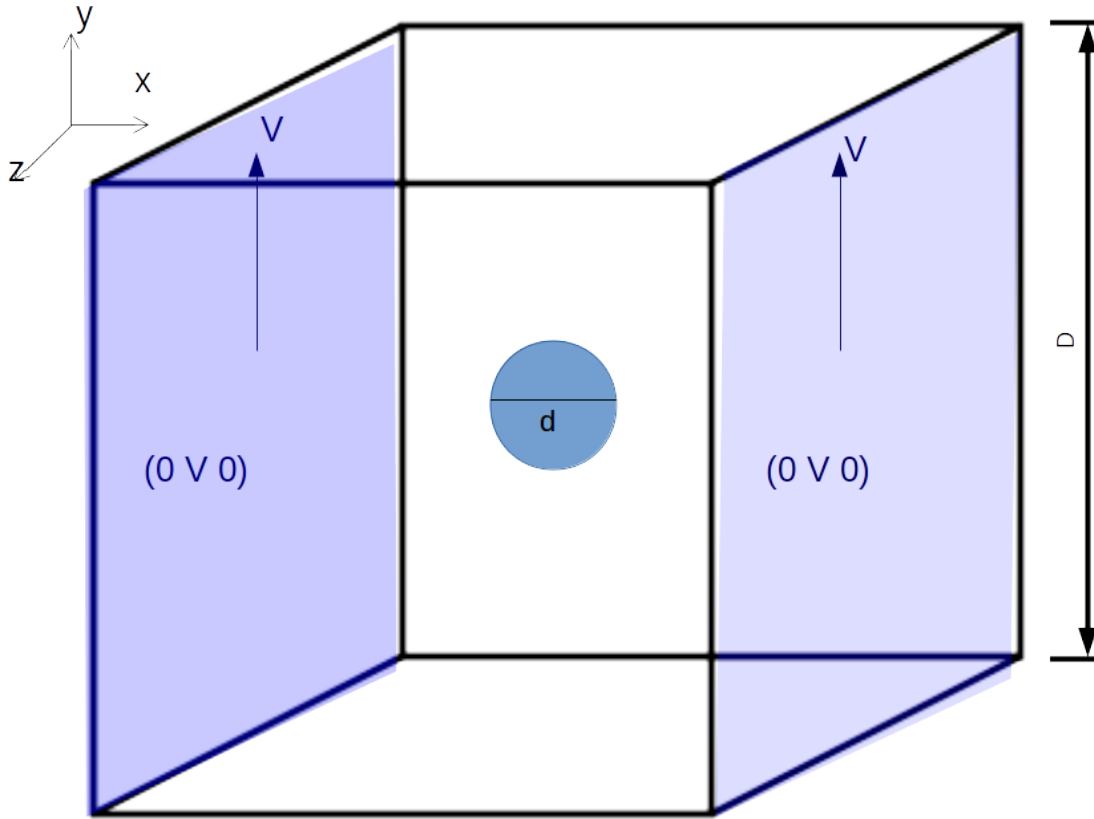


Figure 3.1: Schematic representation for unsheared settling

Figure fig. 3.2 depicts a schematic representation of the computational setup for sheared settling problem. Similar to the unsheared case, each pair of boundaries in the box acquires a certain boundary condition. The left and right (shaded blue region in Fig. 3.2) boundaries of the box are defined as no-slip boundaries that move vertically (y -direction) at a velocity equal to the settling velocity, V ; the boundaries and also move in the opposite direction with the velocity, W , in the z - direction to impart planar shear of $2W/D$ to the fluid medium whereas $W = 0$ for unsheared settling. Therefore, the boundary conditions for the left and right boundaries are $(0 \ V \ -W)$ and $(0 \ V \ W)$, respectively.

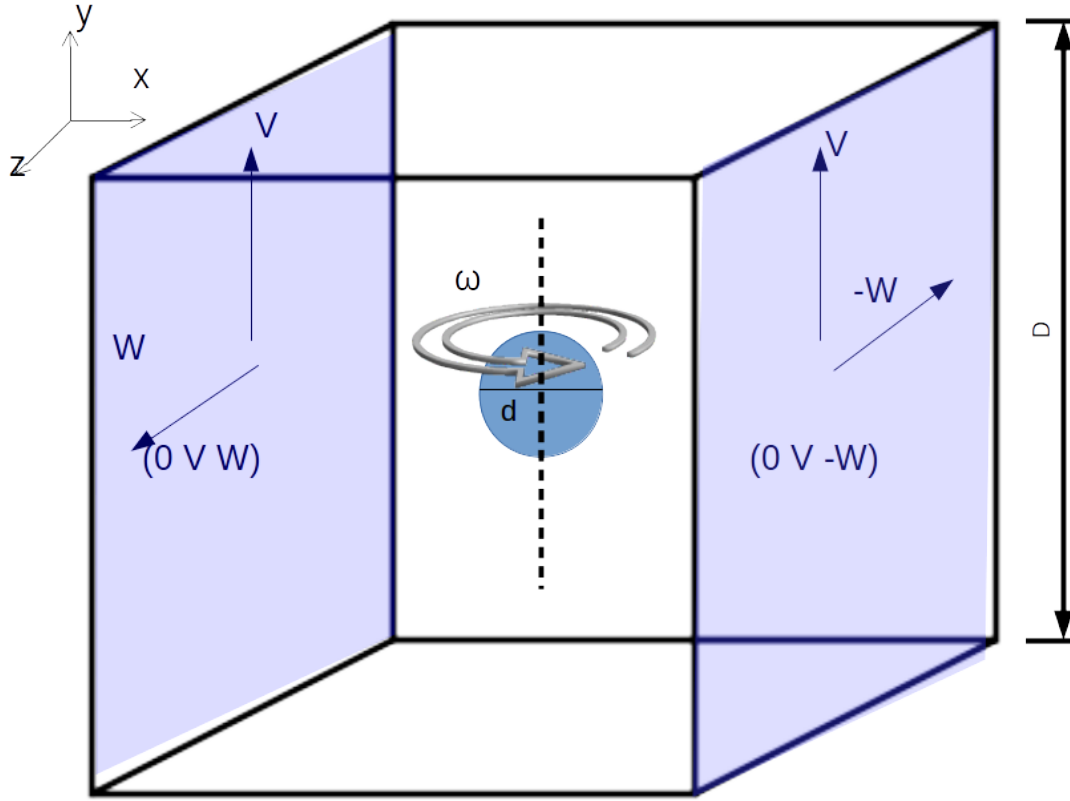


Figure 3.2: Schematic representation for sheared settling

Periodic boundary conditions are used on the two other pairs of boundaries (top and bottom (y) and front and back (z)) of the box. This approximation is equivalent to simulating an infinite 2D array of particles that settle between two infinite moving plates, and it has the potential to introduce errors. The domain width plays an important role in the drag that is experienced by the particle. A domain independence study was carried out to eliminate the entrainment effect that is induced by the boundaries. The effect of this approximation is discussed in the following section.

3.2.2 Boundary conditions

With reference to the problem mentioned above, the setup defined in the previous section, which is a pictorial summary of the boundary conditions, is given in Figures 3.3 and 3.4.

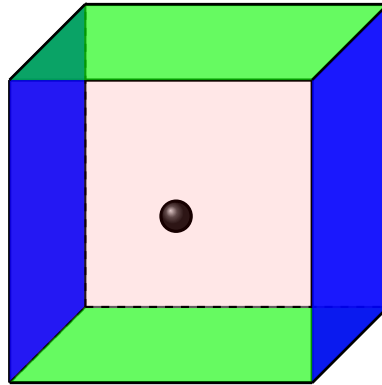


Figure 3.3: Color code for domain walls' boundary conditions demonstration in Table 3.4

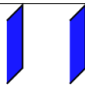

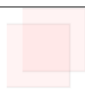
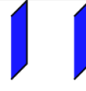
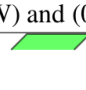

Type of the problem	Boundary conditions	
Settling of particle in unsheared medium	Boundary wall	Boundary condition
		Moving upwards ($0 \ V \ 0$) and ($0 \ V \ 0$)
		Periodic boundary condition
		Periodic boundary condition
Particle settling in shear medium	Boundary wall	boundary condition
		Moving upwards and shearing ($0 \ V \ W$) and ($0 \ V \ -W$)
		Periodic boundary condition
		Periodic boundary condition

Figure 3.4: Boundary conditions for each pair of domain walls.

3.3 Archimedes number

There are many means of non-dimensionalising the results. The use of Archimedes and Reynolds number is one of the ways in which to represent in terms of. In this section, we demonstrate how a dimensionless parameter 'Ar' is inter-replaceable with C_D, Re , by some studies. The incorporating of the density difference into Ar's formulation for a power-law fluid medium is defined in Equation 3.6 Chhabra *et al.* (2001).

$$Ar = \frac{3}{4}C_D Re^{(2/(2-n))} = \frac{gd^{(2+n)/(2-n)}\Delta\rho\rho^{n/(2-n)}}{k^{(2/(2-n))}} \quad (3.6)$$

In our numerical investigation, density differences $500 \leq \Delta\rho \leq 4000$, were considered in this study. It is evident from Equation 3.6, that the representation can be inter-changed to glean information about the particle density simply from the $C_D - Re$ correlation.

For example, for a given Re , the corresponding drag could be determined from the final correlation, and their $\frac{3}{4}C_D Re^{(2/(2-n))}$ would be its corresponding Ar . Using its formulation, the particle density or density difference can be further calculated. Finally, we could say that the representation of the $C_D - Re$ correlation is interchangeable, which enables the extraction of its Ar and, ultimately, data on particle density or density difference.

This interchangeability was intended to check using our results; hence, a behavioural analysis of Ar and $C_D Re^{(2/(2-n))}$ was carried out. Their behaviour was found precisely linear, and this again adds to the reliability of the root-finding algorithm on the model.

3.4 Scaling analysis

It is important to view the results in terms of dimensionless parameters; hence, there is a need to non-dimensionalise the governing parameters using scaling analysis. The dimensionless parameters are developed by carefully choosing a scaling variable for each parameter. Details are discussed in this section.

Choosing a density scale given by the fluid density, a length scale equal to the particle diameter d , a velocity scale given by the settling velocity V , and a viscosity scale given by the viscosity at a shear rate of V/d , the dimensionless form of the momentum equation leads to two different particle settling Reynolds number for power-law and yield-stress fluids.

The governing equations(Eqn. 3.1 and 3.2) are non-dimensionalised using the following dimensionless variables:

$$\nabla = \frac{1}{d}\nabla^* \quad u = Vu^* \quad P = \tau_y P^* \quad \eta = \left(\frac{d\tau_y}{V} + \frac{kW^{n-1}}{d^{n-1}}\right)\eta^* \quad t = \frac{d}{V}t^*$$

The governing equations are rewritten in dimensionless form using the dimensionless variables as mentioned above.

$$\nabla^* . u^* = 0 \quad (3.7)$$

Using the dimensionless variables, the momentum equation takes the following form:

$$\rho \frac{d(Vu^*)}{d(\frac{t}{V})} = -(\frac{\tau_y}{d}) \nabla^* P^* + \frac{1}{d} (\nabla^* . (\frac{d\tau_y}{V} + \frac{kV^{n-1}}{d^{n-1}}) \eta^* \frac{\nabla^*}{d} Vu^*) + \rho g \quad (3.8)$$

Replacing u with Vu^* , t with $\frac{d}{V}t^*$, P with $\tau_y P^*$, η with $(\frac{d\tau_y}{V} + \frac{kV^{n-1}}{d^{n-1}})\eta^*$ and ∇ with $\frac{1}{d}\nabla^*$, $u = Vu^*$, we get the above equation. And on further rearranging we get Equation 3.9.

$$\frac{\rho V^2}{d} \frac{du^*}{dt^*} = -(\frac{\tau_y}{d}) \nabla^* P^* + \frac{V}{d^2} (\frac{d\tau_y}{V} + \frac{kV^{n-1}}{d^{n-1}}) \nabla^* . (\eta^* \nabla^* u^*) + \rho g \quad (3.9)$$

Taking $\frac{\tau_y}{d}$ common on R.H.S, we get,

$$\frac{\rho V^2}{d} \frac{du^*}{dt^*} = -(\frac{\tau_y}{d}) \nabla^* P^* + (\frac{\tau_y}{d}) (1 + \frac{kV^n}{d^n \tau_y}) \nabla^* . (\eta^* \nabla^* u^*) + \rho g \quad (3.10)$$

Taking $\frac{\tau_y}{d}$ common on all terms of R.H.S, we get,

$$\frac{\rho V^2}{d} \frac{du^*}{dt^*} = (\frac{\tau_y}{d}) \left\{ -\nabla^* P^* + (1 + \frac{kV^n}{d^n \tau_y}) \nabla^* . (\eta^* \nabla^* u^*) + \frac{\rho g d}{\tau_y} \right\} \quad (3.11)$$

Rearranging to get $\frac{du^*}{dt^*}$ on L.H.S, we obtain the following equation.

$$\frac{du^*}{dt^*} = (\frac{\tau_y}{\rho V^2}) \left\{ -\nabla^* P^* + (1 + \frac{k\dot{\gamma}^n}{\tau_y}) \nabla^* . (\eta^* \nabla^* u^*) + \frac{1}{Y} \right\} \quad (3.12)$$

Grouping the dimensionless parameters, we get equation 3.13

$$\frac{du^*}{dt^*} = (\frac{HB}{Re}) \left\{ -\nabla^* P^* + (1 + \frac{1}{HB}) \nabla^* . (\eta^* \nabla^* u^*) + \frac{1}{Y} \right\} \quad (3.13)$$

$$\frac{du^*}{dt^*} = \frac{HB}{Re} \{-\nabla^* P^*\} + \frac{1+HB}{Re} \{\nabla^* . (\eta^* \nabla^* u^*)\} + \left\{ \frac{HB}{ReY} \right\} \quad (3.14)$$

From Eqn 3.14, we obtain the dimensionless parameters that govern the flow, namely Reynolds, Herschel–Bulkley and yield-gravity numbers, respectively, given by:

$$\text{Reynolds number, } Re = \frac{dV\rho}{k\dot{\gamma}^{n-1}} = \frac{d^n\rho V^{2-n}}{k} \quad (3.15)$$

$$\text{Herschel–Bulkley number, } HB = \frac{\tau_y}{k\dot{\gamma}^n} \quad (3.16)$$

$$\text{Yield-gravity number, } Y = \frac{\tau_y}{\Delta\rho gd} \quad (3.17)$$

We reduce to three dimensionless parameters (Re, Y and HB) that will be used to present our results in terms of in upcoming chapters.

3.5 Special cases in scaling

3.5.1 Case: 1 Scaling for plastic regime:

In very high HB, that is, when HB tends towards ∞ , the flow regime is termed a plastic regime. This phenomenon can be written numerically as

$$\frac{\tau_y}{\dot{\gamma}} \gg k\dot{\gamma}^{n-1}$$

The scaling for such a flow regime can be carried out by considering the parameters that are dominating the flow and by eliminating the ones that are negligible. The dimensionless variables for the plastic regime are given below.

$$\nabla = \frac{1}{d}\nabla^* \quad u = Vu^* \quad P = \tau_y P^* \quad \eta = \left(\frac{d\tau_y}{V}\right)\eta^* \quad t = \frac{d}{V}t^*$$

The dimensionless governing equation that uses the above dimensionless variables is calculated for the plastic regime.

$$\frac{du^*}{dt^*} = \left(\frac{HB}{Re}\right) \left\{ -\nabla^* P^* + \nabla^* \cdot (\eta^* \nabla^* u^*) + \frac{1}{Y} \right\} \quad (3.18)$$

3.5.2 Case: 2 Scaling for Viscous regime:

In very low HB, that is, when HB tends towards zero, the flow regime is termed a viscous regime. This phenomenon can be written numerically as

$$k\dot{\gamma}^{n-1} \gg \frac{\tau_y}{\dot{\gamma}}$$

The dimensionless variables for the viscous regime are given below.

$$\nabla = \frac{1}{d}\nabla^* \quad u = Wu^* \quad P = k\dot{\gamma}^n P^* \quad \eta = k\dot{\gamma}^{n-1}\eta^* \quad t = \frac{d}{V}t^*$$

The dimensionless governing equation that uses the dimensionless variables that are mentioned above is given by the following equation.

$$\frac{du^*}{dt^*} = \left(\frac{1}{Re}\right) \{-\nabla^* P^* + \nabla^* \cdot (\eta^* \nabla^* u^*)\} + \frac{HB}{ReY} \quad (3.19)$$

3.5.3 Case: 3 Scaling for Intermediate regime

When the yield-stress and the Herschel–Bulkley viscosity equally dominate, that is, when HB tends to one, both the terms have to be considered for scaling. The scaling for pressure and viscosity changes as shown below:

$$\nabla = \frac{1}{d}\nabla^* \quad u = Wu^* \quad P = (\tau_y + k\dot{\gamma}^n)P^* \quad \eta = \left(\frac{\tau_y}{\dot{\gamma}} + k\dot{\gamma}^{n-1}\right)\eta^* \quad t = \frac{d}{V}t^*$$

$$\frac{du^*}{dt^*} = \frac{1 + HB}{Re} \{-\nabla^* P^* + \nabla^* \cdot (\eta^* \nabla^* u^*)\} + \left\{ \frac{HB}{ReY} \right\} \quad (3.20)$$

3.5.4 Case: 4 Scaling for imposed shear

Two different shear rates are experienced by the particle. One is the shear rate due to the settling of the particle, and the other is due to the imposed shear. The formulation of the shear rates due to the settling and the applied shear will be $\dot{\gamma}_{settling} = \frac{V}{d}$ (where V is the settling velocity and d is the particle diameter) and $\dot{\gamma}_{applied} = \frac{2W}{D}$ (where W is the velocity of the shearing plane and D is the distance between the moving boundaries),

respectively. Since both the shear rates share the same units, a scaling analysis will result in the same dimensionless equations.

When the shear from the applied shear and the shear from the particle settling are normal to each other, the total shear rate, $\dot{\gamma}_T$, will be a vectorial sum of both (Gheissary and van den Brule (1996)). Therefore the resulting shear rate will be as follows

$$\dot{\gamma}_T = \sqrt{\dot{\gamma}_{settling}^2 + \dot{\gamma}_{applied}^2} \quad (3.21)$$

For investigating settling under imposed shear, we begin by validating our computational model by using experiments that have been carried out by CSIRO. They have conducted experiments for particle settling in plane shear in a yield- stress fluid, which is fitted by the Herschel–Bulkley rheology model. We non-dimensionalise imposed shear in two different ways to present our results which is discussed in next Chapter.

3.6 Determination of settling velocity for a given $\Delta\rho$

The determination of the terminal settling velocity for particle settling in power-law fluids, the rheological parameters of which closely relates to mining slurries have been computationally solved using the grid resolution and the domain size mentioned above. Theoretically, the forces acting on a settling sphere are drag, buoyancy and its own weight. For a steady flow, the net force acting on the particle is zero. Therefore, the net drag experienced by the particle will be equal to buoyancy force ($\frac{\pi}{6}d^3\Delta$): When they are found to be equal, their corresponding velocity is the estimate for the settling velocity for the density difference between the particle and the fluid.

For a given particle density $\Delta\rho$ and its buoyancy (F_B), the drag force is computed with an initial guess of settling velocity. The settling velocity is then adjusted until the drag force matches the buoyancy so that the net force is zero. The adjustment of the settling velocity is employed using a root-finding algorithm outside the solver (simpleFoam) in OpenFOAM.

The algorithm uses the secant method, which is a root-finding method, with two initial guesses; it throws a new guess that is higher or lower than the initial guesses, depending on the position of the root. The flow chart of this process is outlined in Figure 3.5.

For clarity in representing settling velocity, we use settling velocity under unsheared conditions is denoted as V_U and under sheared conditions as V_{Sh} .

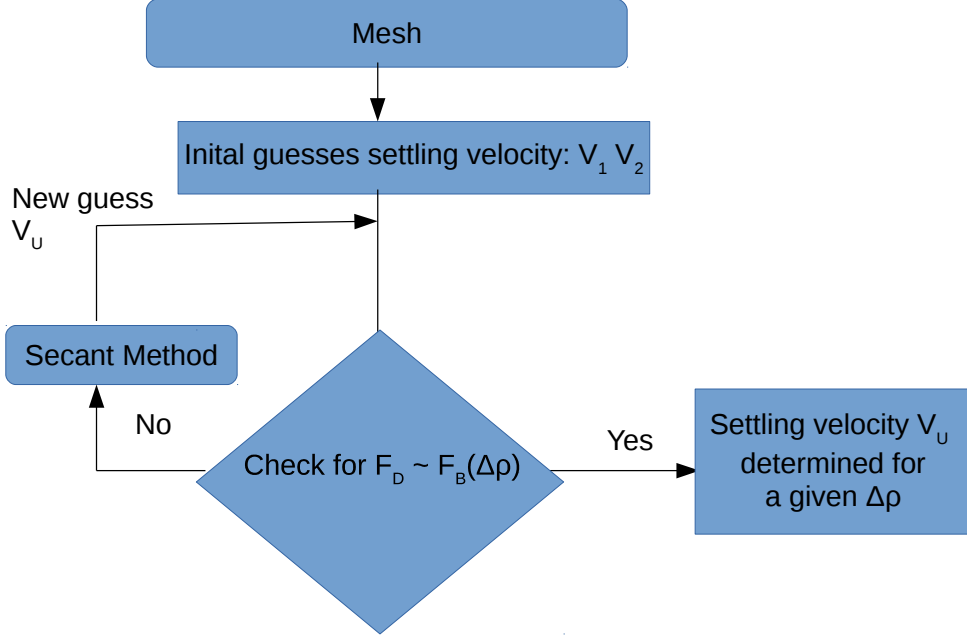


Figure 3.5: Flow chart for determination of settling velocity for a given $\Delta\rho$

3.7 Determination of particle rotation

In the case of an imposed shear, the boundary conditions for the left and right boundaries are $(0 \ V \ -W)$ and $(0 \ V \ W)$, respectively, which yields an applied shear of $2W/D$. When the enforced shear is applied to the stationary sphere, a torque is observed along the y -axis. This is due to the applied shear that produces a spin on the sphere. Under sheared conditions, the particle will also rotate about the y -axis at a rotational velocity ω .

In the computational model, to study sheared particle settling, the rotational velocity, ω is applied to the sphere, and its corresponding torque is noted.

Since for a steady flow there is a zero net torque, we need to limit this value. In order to limit this value, ω is varied to the sphere to reduce the calculated torque, τ , such that $\tau(\omega) \sim 0$. Therefore, in the simulations, ω is varied until the net torque on the sphere is zero. This zero torque is achieved by the ‘secant method’.

In a Newtonian fluid in the Stokes regime, the particle rotational velocity is given by half the imposed shear, that is, $\omega = W/D$. In viscoplastic fluids and non-creeping

Newtonian fluids, this rotation is unknown. The rotational velocity that provides zero net torque is found by using the secant algorithm. The root-finding process begins with initial guesses of $\omega = W/D$ and 0; it then progresses to predict a new guess with respect to the net torque value for the guesses that are shown in Figure 3.6. In order to determine the particle settling and rotational rate, the algorithm to determine, V_s , as shown in the Figure 3.5, is coupled with the secant algorithm to find ω , as can be seen in Figure 3.6. Convergence criteria that are used for a steady-state incompressible non-Newtonian flow for pressure and velocity have been maintained low at $1e^{-8}$. To computationally solve non-linear viscosity models, the initial conditions that are provided should be a converged solution of the previous flow index or consistency. This is done to avoid the large amount time that is taken for convergence.

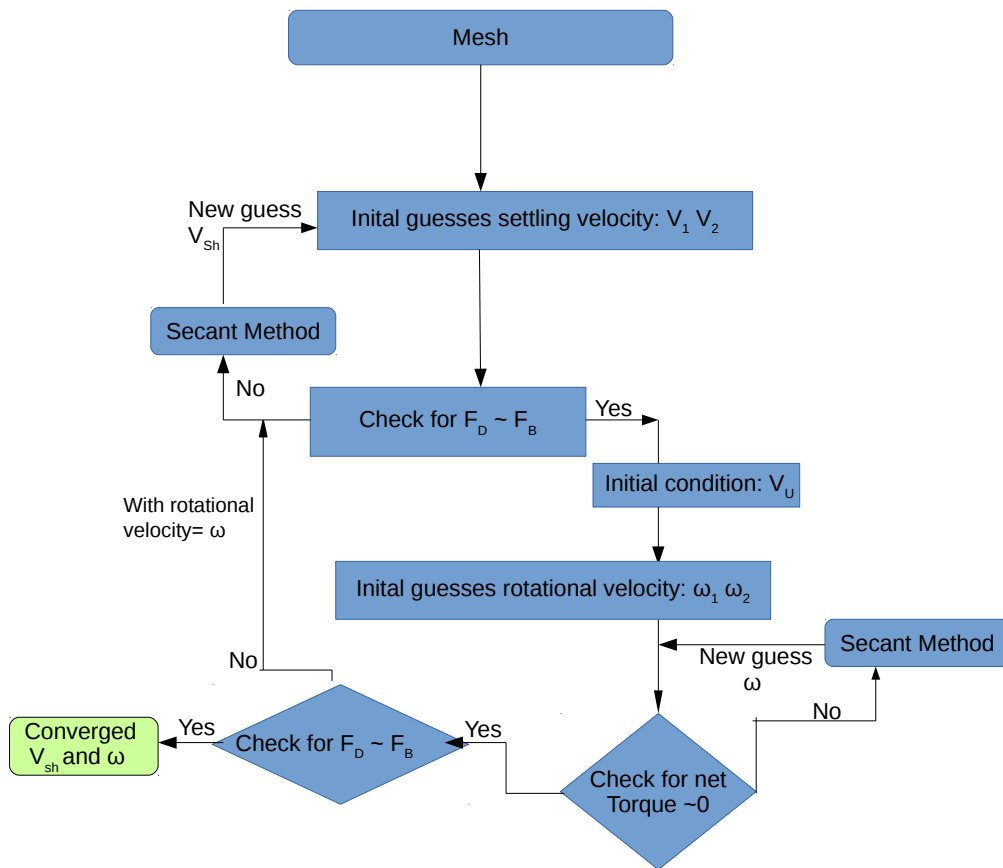


Figure 3.6: Flow chart for determination of particle rotation

3.8 Grid and domain independence

The finite size domain is only an approximation to particle settling in the infinite domain and the presence of the wall will influence settling. Atapattu *et al.* (1995b) showed that the ratio of the domain length (D) to the particle size (d) needs to be greater than 15 for boundaries to not matter; however, this needs to be investigated here to ensure that the results are domain-independent. In order to avoid wall effects in the results, a domain-independence study was carried out.

Grid resolution is also a key pre-requisite to ensure reliable results. In particular regions of the highest variations near the surface of the particle, must be adequately resolved. In order to ensure that the solution is independent of the grid resolution, a grid resolution study should be carried out to address this issue.

The effect of the walls and the resolution around the particle surface could affect the coefficient of drag, C_D . The domain independence and the grid resolution study was conducted by studying C_D for increasing the domain size and various grid resolutions. Therefore, we use rigorous validation with a benchmark solution of the Stokes drag coefficient to obtain a domain and grid-independent solution that would ensure a cost-effective and accurate simulation.

3.8.1 Grid generation

Although a large array of options that are available for mesh generation in OpenFOAM, snappyHexMesh and blockMesh (in-built tools in OpenFOAM) were used in this study.

1. **BlockMesh** - The geometry of this setup was generated using this utility. The number of nodes mentioned in a blockmesh, which is a utility used to create simple block-based fully structured hexahedral meshes. A three-dimensional box (which acts as the fluid domain) was generated using this utility.

2. **SnappyHexMesh** - requires an already existing base mesh (a simple-block, fluid domain in this case that was created using blockmesh) to work with. Depending on the options in the input file (snappyHexMeshDict), it can: refine the mesh; adjust the mesh to fit onto provided geometries (sphere in this case); and add boundary layers near the

requested patches. The stereolithography (STL) object of a sphere was introduced at the centre of the base mesh, and appropriate adjusting from the base mesh was done.

3.8.1.1 Grid resolution parameters

There are a number of interacting parameters that control the quality of the grid that is used in this study. The independence of the solution for the grid resolution was considered. To study the effect of the grid resolution, a fixed box size ($10D$ big) was used, and key geometric parameters were modified, such as the number of surface elements on the sphere (N_s), the thickness of the first shell of elements on the surface of the sphere (Δ_1) and the expansion factor for the element thickness that move away from the surface (r_e).

1. **Number of Surface cells** : Number of 3D elements that are attached on the surface of the sphere.
2. **Expansion ratio** : Expansion factors are controlled by a mesh expansion ratio. The expansion factor is the change in volume between two neighboring cells, more specifically, between two sub-control volumes on neighboring cells.
3. **First cell height** : The thickness of the first layer that is attached to the surface of the sphere.
4. **Refinement region**: A region of refinement around the particle surface is introduced to investigate the drag prediction performance. In this case, it is a spherical refinement region of a size twice the particle diameter.

Details about the setting up of some of the above parameters were used to inter play to conduct this study.

3.8.1.2 Number of surface cells

The surface of the sphere is discretised with an N_s element in which we choose values, $200 \leq N_s \leq 80000$. The surface length scale (L_s) for a mesh element on the surface of the sphere is defined by:

$$L_s = \sqrt{\frac{4\pi r^2}{N_s}} \quad (3.22)$$

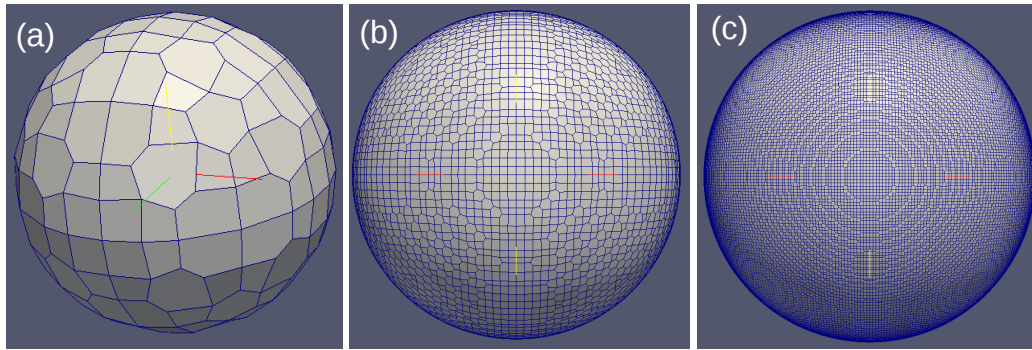


Figure 3.7: Surface cells varied on the object-sphere (a) Coarse -200 cells (b) Medium-6000 cells (c) Refined -40,000 cells

OpenFOAM performs simulations in physical co-ordinates; therefore, there is a need to choose d . However, results will be presented in a non-dimensional form and can be scaled to any particle size of choice at scale parameters. For instance, the number of nodes in blockMesh and the level of refinement in snappyHexMesh specification to increase the number of surface cells is given Table 3.1 for a one cm particle in a ten-centimeter box, the results of which can later be translated to a dimensionless form. For a different sized box or particle, the number of cells in blockMesh and the level of refinement in snappyHexMesh would vary. Once the surface cells are varied in the mesh by increasing the nodes as shown in Table 3.1, the number of surface cells is examined by certain methods in OpenFOAM. The data of surface cells data was gleaned by referring to the log file that was generated during meshing (log.snappyHexmesh).

Nodes at BlockMesh	Level of refinement in snappyHexMesh	Number of surface cells(Ns)
(20 20 20)	level (2 2)	200
(20 20 20)	level (3 3)	744
(30 30 30)	level (3 3)	1584
(20 20 20)	level (4 4)	2768
(25 25 25)	level (4 4)	4344
(30 30 30)	level (4 4)	6120
(20 20 20)	level (5 5)	10904
(30 30 30)	level (5 5)	24312
(35 35 35)	level (5 5)	33176
(40 40 40)	level (5 5)	42936
(50 50 50)	level (5 5)	67400

Table 3.1: Meshing input specification in OpenFOAM to increase the surface cells ranging between 200 -67000 cells

3.8.1.3 Expansion ratio

The ratio of heights from one layer to the next consecutive layer in a direction away from the surface, that is, $\frac{\Delta_2}{\Delta_1} = \frac{\Delta_3}{\Delta_2} = \frac{\Delta_4}{\Delta_3} = \frac{\Delta_5}{\Delta_4}$ as can be seen in Figure 3.8.

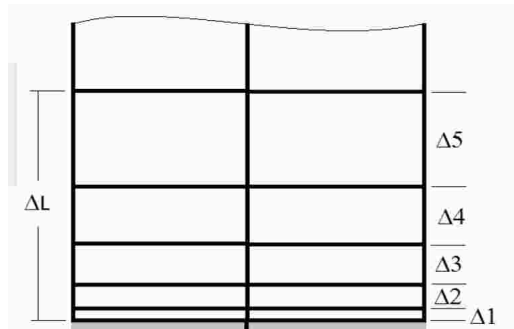


Figure 3.8: Expanding of layers and total thickness (ΔL)

3.8.1.4 Setting up layers around the sphere

The first layer of cells that are adjacent to a sphere, and the thickness of the nearby cells that are attached to the surface of the particle are referred to as the ‘first layer thickness’. Multiple layers were added that progresses from the first layer.

In OpenFOAM, layer addition is a function of the expansion ratio, final layer thickness (FLT) and the number of required layers. As can be seen in Figure 3.9, multiple layers were added around the surface of the particle to increase the grid resolution around the sphere. The near resolution at the surface of the sphere (Δ_1) is set to a fixed fraction (ϵ) of the mean length surface scale (L_s) - $\epsilon * L_s$ and a fixed expansion factor away from the sphere 1.3 until the wall normal spacing becomes equivalent to the tangential spacing, and then have elements approximately uniformly sized in all directions until the radius is equal to a single particle diameter, after which the element size can continue to expand. The mathematical representation of this approach is explained below by first defining first layer thickness (Δ_1) and ratio of consecutive layers’ thickness (r_e) to derive the final layer thickness (FLT).

The first layer thickness at the surface of the sphere (Δ_1) is set as:

$$\Delta_1 = \epsilon L_s \quad (3.23)$$

The ratio between two consecutive layers’ thickness is given by the product of first layer thickness and the expansion ratio, r_e .

$$\frac{\Delta_{i+1}}{\Delta_i} = r_e^n \epsilon L_s \quad (3.24)$$

We consider the last layer thickness at the surface of the sphere to be L_s ,

$$\Delta_n = r_e^n \epsilon L_s = L_s \quad (3.25)$$

$$r_e^n = 1/\epsilon \quad (3.26)$$

Therefore, the number of surface layers required is given by,

$$n = \frac{\log \frac{1}{\epsilon}}{\log r_e} \quad (3.27)$$

$$fLT = r_e^{n-1} \epsilon \sqrt{\frac{4\pi r^2}{N_s}} \quad (3.28)$$

where r_e is the expansion factor and fLT is the final layer thickness.

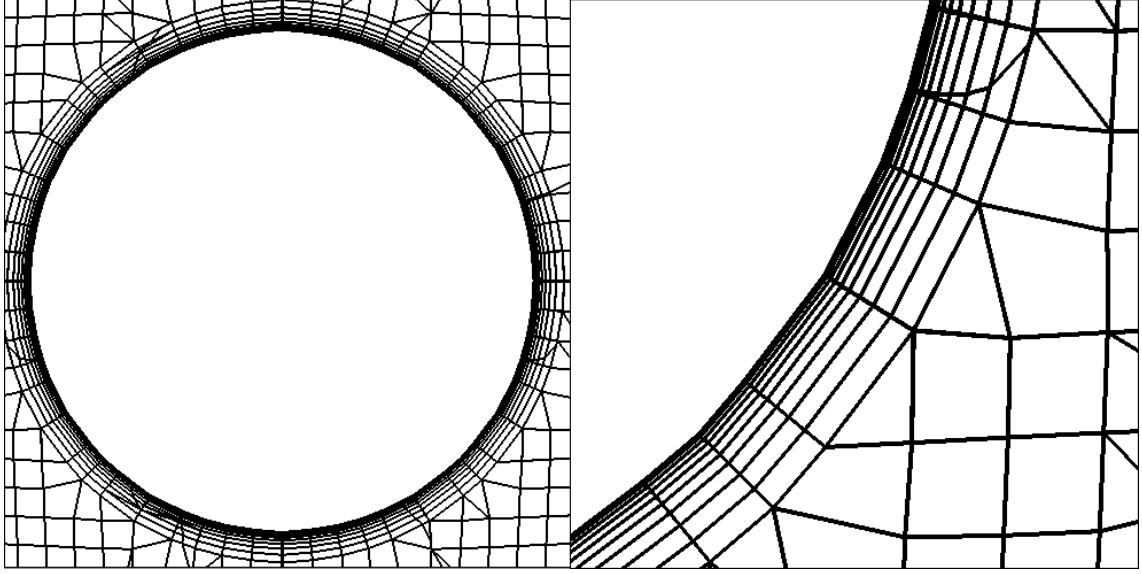


Figure 3.9: On the left image, zoomed view of the slice of 3D mesh used in the simulations. On the right, the layers around the particle surface widen according to the expansion ratio $r_e=1.3$

Once grids were generated for a range of surface resolutions, predictions of the drag coefficient were noted. To increase the refined meshes using a range of each of the grid-controlling parameters, the drag was compared with the Stokes drag to determine when the results converged, that is, asymptote beyond a specific magnitude. Values of $N_s \geq 10000$, Δ_1 =one tenth of the length scale of the surface mesh and $r_e=1.3$ are found to provide converged results and are subsequently used in all simulations. It was found that the ratio of the domain size (D) to the particle size (d) needed to be $D/d \geq 15$ to provide converged results. This result is in agreement with the results of wall effects for yield-stress fluids, which was presented by Atapattu *et al.* (1995a). Approximately three million grid cells and $D/d = 30$ were used in the simulations.

Number of surface elements(N_s)	Surface length scale	Final layer thickness
200	2.51e-3	2.05e-3
744	1.3e-3	1.06e-3
1584	8.91e-4	7.3e-4
2768	6.7e-4	5.5e-4
4344	5.4e-4	4.4e-4
6120	4.53e-4	3.7e-4
10904	3.4e-4	2.77e-4
24312	2.27e-4	1.85e-4
33176	1.95e-4	1.58e-4
42936	1.71e-4	1.4e-4
67400	1.37e-4	1.12e-4
81456	1.24e-4	1.013e-4

Table 3.2: Layer thickness calculated using Equation 3.28 for a range of N_s studied

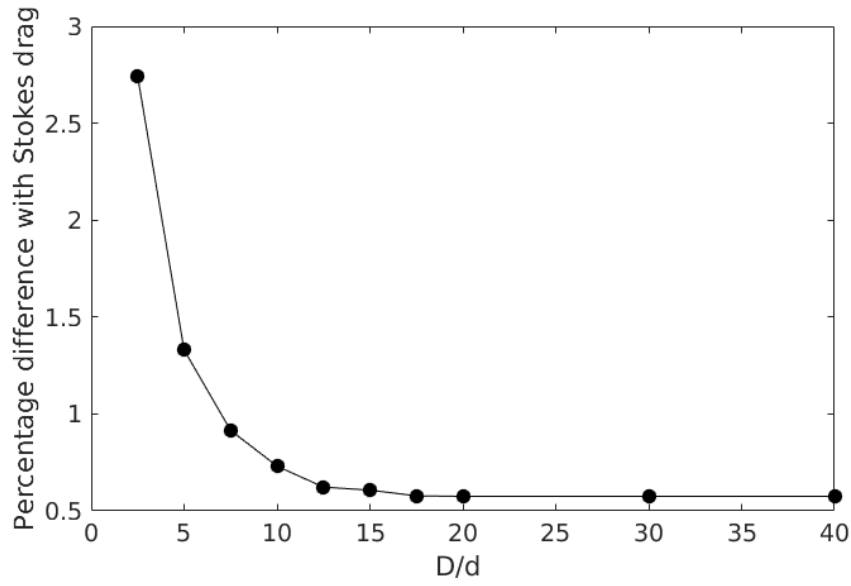


Figure 3.10: The grid resolution around the sphere was maintained constant and the box size was varied

To increase N_s , the first layer becomes thinner. When $\epsilon = 0.1$, the height of the first layer is $0.1 * L_s$, the layer grows with respect to the expansion ratio. The final layer thickness for a range of N_s with respect to their corresponding surface length scale is given in Table 3.2.

3.9 Mesh types

The importance of grid resolution around the particle surface is discussed in the previous section. The mesh quality at a certain defined region around the particle is investigated. The defined region considered here is twice the particle size from the center of the domain and is refined at different levels to determine the manner in which the solution varies or remains independent of the additional cells that are responsible for refinement.

3.9.1 Levels of refinement

The level of refinement around the particle is increased to understand if there is any significant difference in the predicted solution. The mesh was created in such a way that there are around two to five levels refinements at increasing levels around the surface of the particle. As the cells move away from the particle, the cells grow farther and wider. The predicted solution using the mesh, shown in Figure 3.11, was compared with the mesh without any levels of refinement. The percentage difference from the solution was observed to determine an optimum grid for all further numerical investigation.

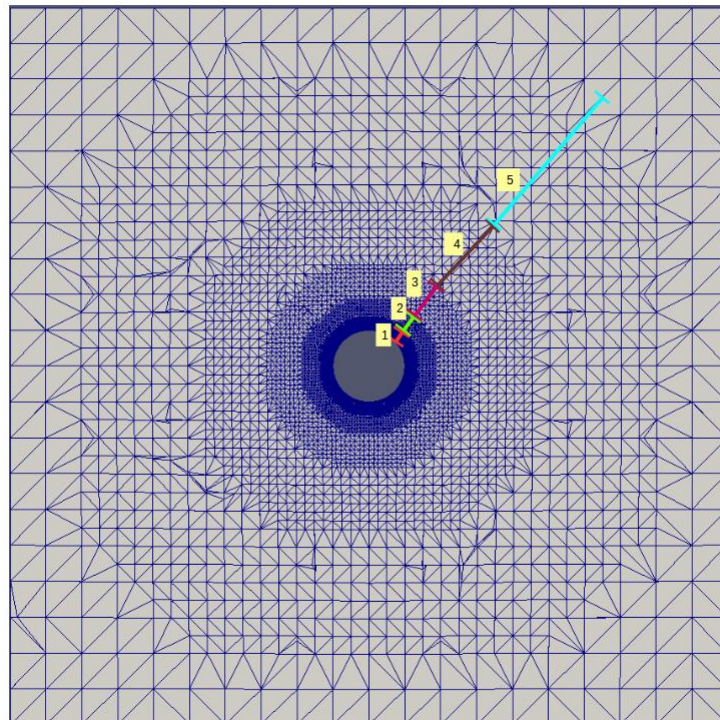


Figure 3.11: Mesh type 1 - slice view: Level of refinement at 5 stages

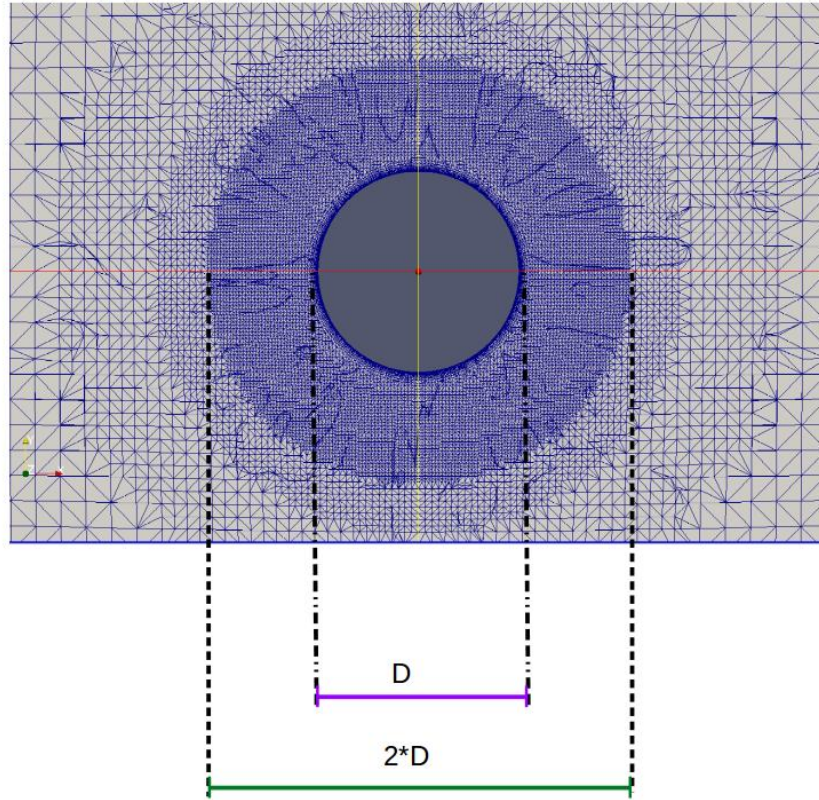


Figure 3.12: Mesh type 2 -slice view : Intense refinement at a selected circular region - 2 times the particle diameter

The two mesh types that are shown in Figure 3.11 and 3.12 have been studied, and a combination of both the features was found to provide accurate results; in addition, its corresponding coefficient of drag (C_D) was measured.

3.10 Grid resolution study at a different Re

It is logical to consider the grid resolution study for a fluid flow, the viscous stress of which dominates the pressure, that is, for Re of less than one. This is because the study will be primarily about the effects of the deformation of the viscous stresses around the surface of the particle. Therefore, a grid resolution study at a low Re in which the viscous force is dominant is sufficient.

However, in this case, a slightly different Re (in this case $Re = 0.2$) was also investigated. We found that the results of an optimum grid appeared to be the same. As can

be seen in Figure 3.13, the drag coefficient converged for $N_s > 10000$, as in the previous case.

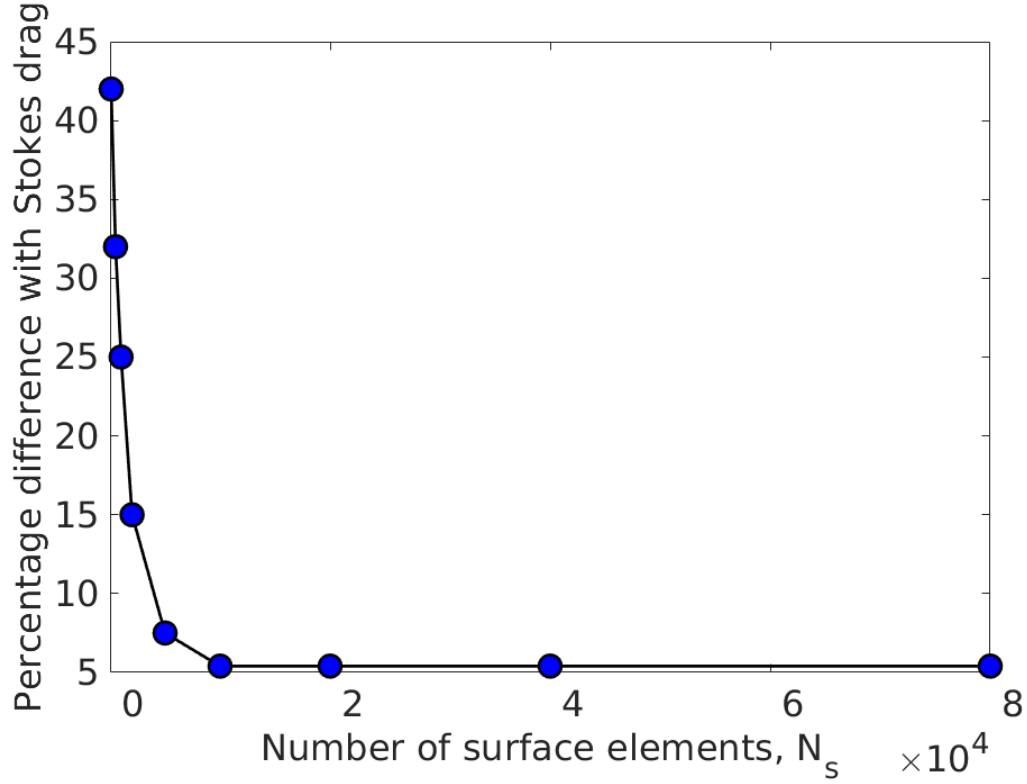


Figure 3.13: Percentage difference with Stokes drag versus number of surface elements on the sphere, N_s

3.11 Domain independence and grid resolution study for non-Newtonian fluids

A grid resolution study for non-Newtonian fluids was also undertaken. A similar approach of investigating the predicted drag for each domain size was studied. This is was done to find domain independent grid. The domain independence study was carried out for power law fluids (discussed in Chapter 4) and yield stress fluids (discussed in Chapter 5). In summary, it was found from the study that $30D$ was more suitable for the numerical investigation on non-Newtonian fluids as the solution predicted by our computational model converged beyond $30D$.

3.12 Experimental methodology used by CSIRO

An important requirement for any computational study is an indication of the validity of the simulation results. In a number of earlier studies of particle settling in sheared fluids, experimental equipment based on cylindrical Couette flow was used, which does not supply a constant, uniform shear field (e.g. Wilson (2000)), which complicates the combined effects of particle applied shear and applied shear. Talmon and Huisman (2005) approximated a uniform linear shear field by using a very large cylindrical Couette rig and produced consistent results, although the size of such an apparatus can become prohibitive in large particles. An alternative is a moving belt planar Couette arrangement that is able to provide a defined volume of constant shear stress/shear rate. Some previous work of this type is available in the literature. For example, S. Caserta *et al.* (2011) describe a rig to investigate shear induced particle migration at the micro scale, at which the fluid used was a highly elastic non-Newtonian fluid. Typical gaps were 300–700 micron, and the particles were rigid spheres of 90.9 micron.

An experimental rig that was designed and fabricated here was informed by the limitations of earlier experimentation, and is shown in Figure 3.14. The approach is to generate shear using two parallel belts that are fully submerged in a liquid that is held inside a transparent-walled box with a volume of 0.6 m³. The belts move in opposite directions; each belt has an equal and opposite velocity that can be varied. This design results in a zero-net velocity on the centre-plane between the belts. This is desirable to minimise horizontal translation of the particle during fall experiments McLaughlin (1991). A large measurement zone is included to increase the region of uniform shear and to allow particles to reach terminal velocity. Each belt is 450 mm high (in the direction of the fall) and has a straight length of 1300 mm (in the direction of the belt motion). The shear rate between the belts can be varied by changing the speed of the two independent drive motors and/or by varying the gap (D) between the belts (from 10 to 400 mm). The fluids used in the experiments are transparent fluids that allow optical access, which facilitates the photographing of the settling particles using the Particle Image Velocimetry (PIV) of the flow field. Once the belts are set in motion, the test particle is released on

the centre plane, half way along the belt.

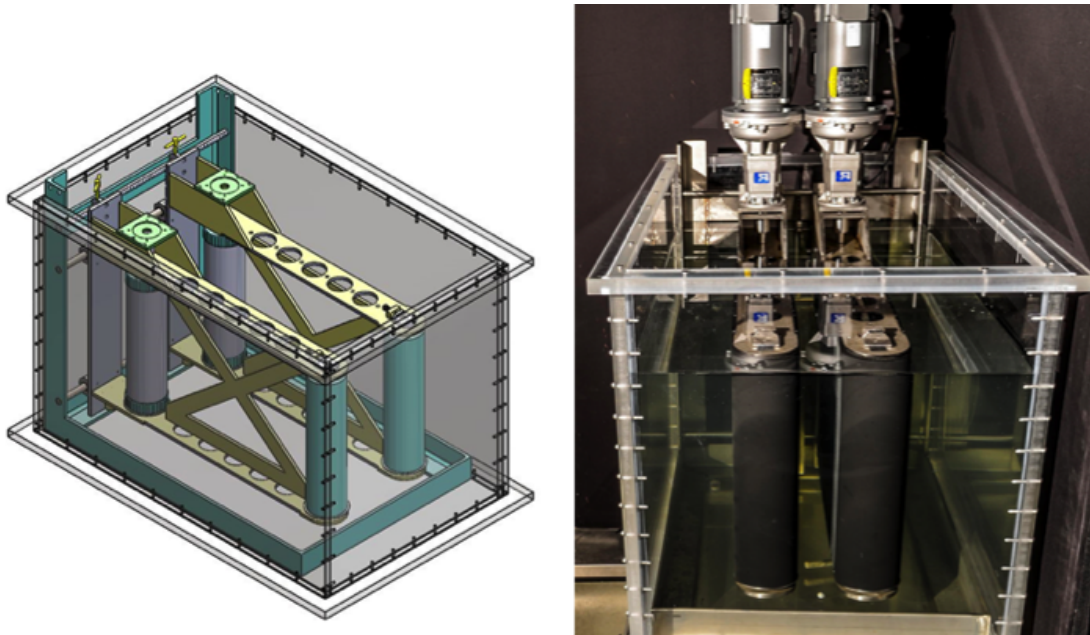


Figure 3.14: CAD drawing and photograph of the sheared settling rig developed at CSIRO.

In settling experiments the proximity of boundaries can affect the settling behaviour, and several authors, (e.g. Missirlis *et al.* Missirlis *et al.* (2001)) have suggested that, in cylindrical settling chambers, the particle-to gap-ratio should be less than 0.05 to ensure that the falling velocity is within 90 % of the unhindered terminal settling velocity. To test for the effect of sphere diameter to gap ratio (d/D), tests were conducted at a constant shear rate with varying gaps. No measurable effect of the gaps that were used in these experiments (not shown) was observed. For analysis, the conditions in the measurement zone are, thus, a good approximation in the case of infinite parallel plates (planar Couette flow), which is assumed from henceforth.

The generally accepted value of the Reynolds number at which the Couette flow becomes unsteady is approximately 370 Dou *et al.* (2007), based on the gap width, D , and the velocity difference between belts, $2V_b$. However, for the shear-thinning fluids used in the study, this transition value is not known, and a number of velocity measurements were undertaken in the gap between the belts using PIV. These measurements (not shown) indicated that, provided Re was less than approximately 230, a stable region of uniform

shear could reliably be attained in the central part of the sheared zone. However, there were some edge effects at the top and bottom of the belt, which reduced the effective measurement zone by approximately 40 mm. These factors were taken into consideration when running individual experiments.

A high-speed camera (Phantom v210 operating at 400 frames per second at a resolution of 1280×800 pixels) was used to record the particle fall and to estimate its settling velocity. The video was recorded with a horizontal view of the gap between the belts; the falling sphere's position was determined by measuring the pixels. A typical calibration for the image pixel to real-world dimension is shown in Figure 3.15. The full recordable distance is 130 mm with no distortion over that range. The available distance allowed for steady-state velocity to be achieved (as measured from video images), and any experiment where this was not the case was rejected. In the experiments, digitised video images were used to determine the height as a function of time, which allowed instantaneous velocity to be calculated. For each particle and applied shear rate, a minimum of five runs were measured and averaged. The digitisation process also allowed confirmation that steady-state settling had been achieved.

The properties of the different particles used are shown in Table 3.3. The densities were measured by a pycnometer and the diameters (in three axes) were measured by Vernier calipers to within 10, μm . This allowed an estimate of sphericity to be made, which in all cases, was greater than 99 %.

Table 3.3: Particle parameters used in the experiments.

Material	ρ (kg m ⁻³)	D mm
Steel	8042	3.96
Steel	8042	4.7

The fluid that was used in the validation measurements was a 0.1 % solution of Carbopol 980. Accurate rheological characterisation of this fluid is essential to match the simulation with the experimental data. The range of shear rates required could be covered with a Haake Rheostress RS1 rheometer by using a concentric cylinder (Couette)

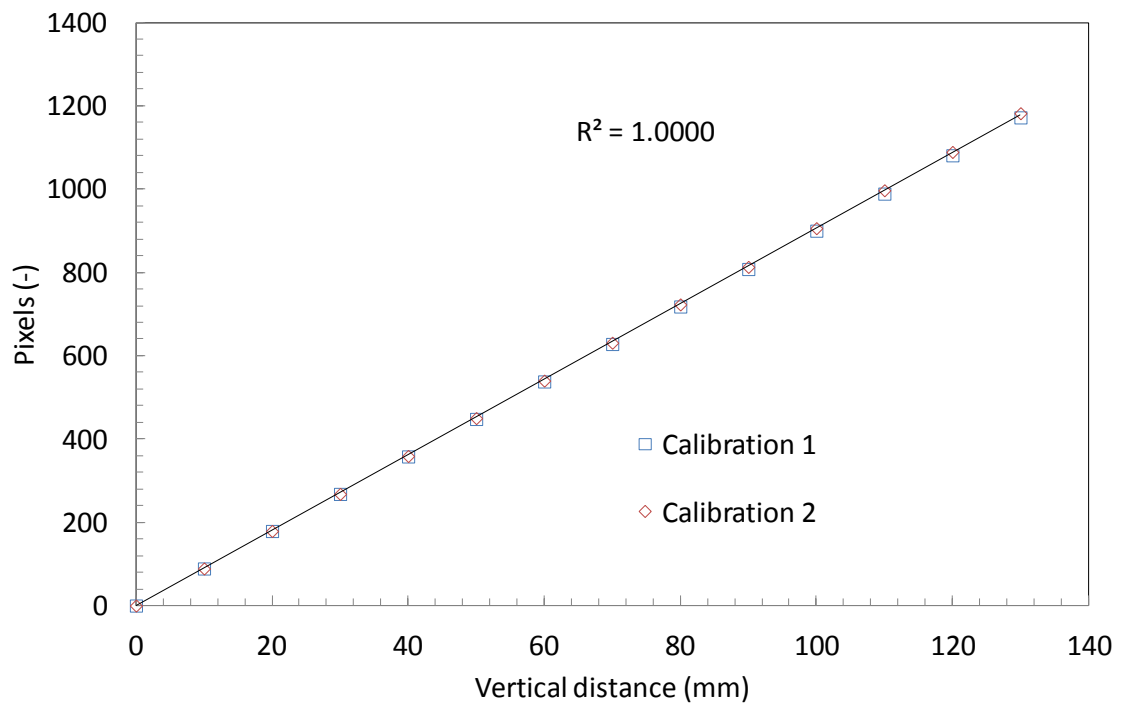


Figure 3.15: Calibration curves for translating images to distance traveled. Both examples show high linearity, that is, no distortion with position.

geometry that comprises a 38 mm inner cylinder and a 41 mm outer (stationary) cylinder. Temperature control was maintained via a recirculating water bath; test temperatures were matched with those in the sheared settling measurements within ± 0.1 C. The upper range of the measurements in the concentric cylinder geometry was limited due to the inaccuracies that were caused by the onset of Taylor-Couette vortices, which is a secondary flow effect at high shear rates (Taylor (1923)). In the unaffected region, the correct shear rate (allowing for the non-Newtonian fluid effect) was obtained by using an integration approach for the Couette inverse problem(MacSporran (1986)). This method is generally more successful than a differential approach due to the inevitable noise that is present in real data. Repeat results were combined and averaged. The measured rheology of the Carbopol solution was fitted to a Herschel-Bulkley model, and the model parameters are shown in Table 3.4. Validation against shear-thinning Carbopol solutions will provide good validation data. The comparison of CFD with experimental results will be discussed in subsequent chapters.

Table 3.4: Fluid rheology.

Material	τ_Y (Pa)	k (Pa s ⁿ)	n (–)
0.1 wt % Carbopol 980	10.0	2.19	0.50
In CFD actually used	9.76	2.41	0.48

3.13 Summary

The numerical methods that were used in this study are elaborated in this chapter. The governing equations to solve the problem of particle settling under sheared conditions in non-Newtonian fluids are discussed.

The overview of the grid and domain independence study determine the grid of appropriate resolution and domain size that would ideally yield the same drag coefficient (total force acting on the particle) as we moved to a higher mesh resolution or domain size. This would result in a cost-effective grid resolution for the computational study.

Other flow behaviors have not analysed, and only the Stokes drag coefficient has been examined at this point. Drag coefficient C_D predictions were compared to determine the point at which the results converged. Values of $N_s \geq 10000$, Δ_1 =one tenth of the length scale of the surface mesh and $r_e=1.3$ were subsequently used in the simulations. Predictions of the drag coefficient, C_D , for different box sizes (at the converged resolution mentioned above) were compared. From this it was determined that the ratio of domain size (D) to particle size (d) needed to be ≥ 15 to provide converged results. This result is in agreement with the results that are presented in Atapattu *et al.* (1995a) for yield-stress fluids. Approximately three million grid cells were used in the simulations. A similar approach for non-Newtonian fluids was considered. The results showed that a mesh that was slightly more refined than the mesh used in Newtonian fluids was more suitable for computational simulations of non-Newtonian fluids.

Once a cost-effective mesh was established, the methodology to identify the unknown variables such as particle rotational velocity and settling velocity for a given density difference were developed using external scripts to vary the input variable until the solution for a steady-state was obtained. The methodology used external scripts to vary the input variable until the solution of a steady-state was obtained. Therefore, all the nec-

essary tools have been equipped for the intended numerical investigation of a wide range of parameters such as fluid rheology, particle size and density difference.

Chapter 4

Settling in power-law fluid

IN this chapter, particle settling with and without imposed shear in a power-law fluid is described. These unsheared and sheared conditions in particle settling form the basis of this study, and the study consist of drag prediction for unsheared and sheared flows, respectively. Firstly, we verify the model for predictions under an unsheared condition. This is done by comparing our drag predictions with a set of known previous findings for particle settling in power-law fluids. Once the model is found to be reliable, predictions for a wide range of parameters that pertain to mining slurries (that are fitted by power-law model) are presented. Next, the method that is used to determine the particle settling rate (and hence, the drag coefficient) in an unsheared condition is outlined. We then validate the model for predictions under sheared conditions using experimental measurements by CSIRO. After stringent validation of the model, a detailed investigation of particle settling in power-law under sheared conditions is discussed. We studied the manner in which the imposed shear altered the settling rate by modifying the shear-thinning viscosity around the particle boundary. In essence, the consequence of the imposed shear elevates the settling rate in power-law fluid depending on the applied shear. Then, the effect of shear on other fluid rheologies is discussed. Finally, sheared settling predictions are presented with respect to the applied shear. using the governing dimensionless numbers.

4.1 Validation of unsheared power-law fluids

In the investigating of the significance of imposed shear on particle settling, the motivation is to understand particle settling under an unsheared condition first. It is important to

consider settling without shear because the shear-thinning behaviour of the fluid, which essentially is the functions of n , needs to be taken into account.

In the steps of investigating unsheared settling in power-law fluids, we begin with validating the model by using the previous findings. As discussed in Chapter 2, a broad range of the settling rate measurements have been published for various ranges of power-law fluids since the 1960s. They are used to validate the model in this study. Finally, the validated model paves the way for further exploration of a wide range of parameters that pertain to mining slurries that can be fitted by the power-law model.

In order to validate the model outlined in Chapter 3, the particle settling velocity was determined for different fluid consistencies, k ; flow index, n ; and density difference, $\Delta\rho$. In our numerical investigation, density difference, $500 \leq \Delta\rho \leq 4000 \text{ kg/m}^3$; flow index, $0.3 \leq n \leq 1.0$; and consistency, $0.1 \leq k \leq 2.0 \text{ Pas}^n$, were considered.

As expected, the particle settling velocity increases as the density difference ($\Delta\rho$) increases, as shown in Figure 4.1. Unsurprisingly, the effect of fluid consistency, k on V_U , is approximately linear, with a higher consistency resulting in a lower velocity. The effect of decreasing flow index is to increase the settling velocity as n decreases.

Graham and Jones (1994), Atapattu *et al.* (1995b) and Dhole *et al.* (2006) all presented a relationship between C_D and Re for power law fluids at finite Re by using experimental and numerical methods. Graham and Jones (1994) and Dhole *et al.* (2006) used a numerical approach to establish an empirical relationship for drag prediction. They used experimental studies by Koziol and Glowacki (1988) and Dennis and Walker (1971) to validate their approach. Although it is crucial to compare the results with experimental studies, the results are compared with other numerical predictions by Graham and Jones (1994) and Dhole *et al.* (2006). This is due to the fact that they have already validated their prediction with experimental measurements by Dazhi and Tanner (1985) and Koziol and Glowacki (1988).

The results presented in Figure 4.1 were appropriately non-dimensionalised and are plotted in Figure 4.3 to compare. We notice that the relationship between C_D and Re is a function of the flow index. It is interesting to ascertain again from the dimensionless plot that the drag coefficient reduces as the flow index increases.

The reported results of Graham and Jones (1994) in predicting the drag coefficient is given by Equation 4.1, and it is compared with the results obtained in this study, as shown

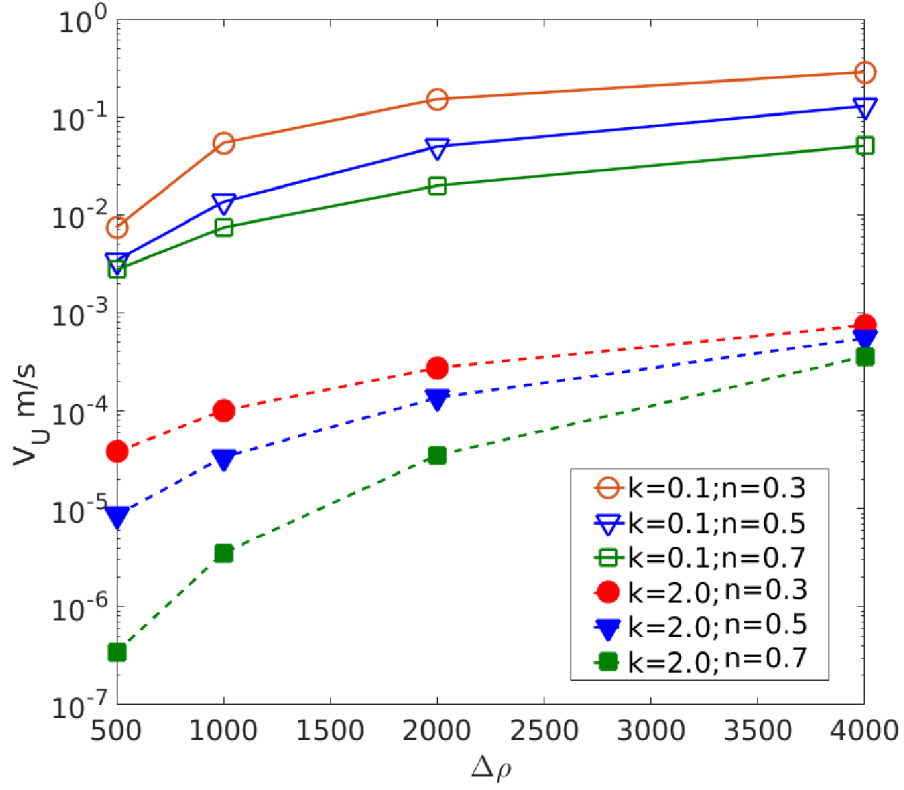


Figure 4.1: Settling velocity as a function of density difference

in Figure 4.2.

$$\begin{aligned}
 C_D &= \frac{12}{Re} 2^{(1-n)} (2-n) & Re \leq 0.2 \\
 C_D &= \frac{35.2}{Re^{1.03}} + n \left\{ 1 - \frac{20.9}{Re^{1.11}} \right\} & 0.2 \leq Re_p \leq 24 \\
 C_D &= \frac{37}{Re^{1.1}} + 0.25 + 0.36n & 24 \leq Re \leq 100
 \end{aligned} \tag{4.1}$$

Similarly, the results were compared with Dhole *et al.* (2006) for a higher Reynolds number. The expression given by Dhole *et al.* (2006) is given in Equation 4.2. The results of the work show excellent agreement with the correlations in Equation 4.2. This agreement establishes the confidence to proceed with further investigation.

$$\begin{aligned}
 C_D &= \frac{24}{Re} [1 + a Re^{bn/(cn+d)}] & 5 \leq Re \leq 250 \\
 a &= 0.148, b = 2.346, c = 2.423 \text{ and } d = 0.918
 \end{aligned} \tag{4.2}$$

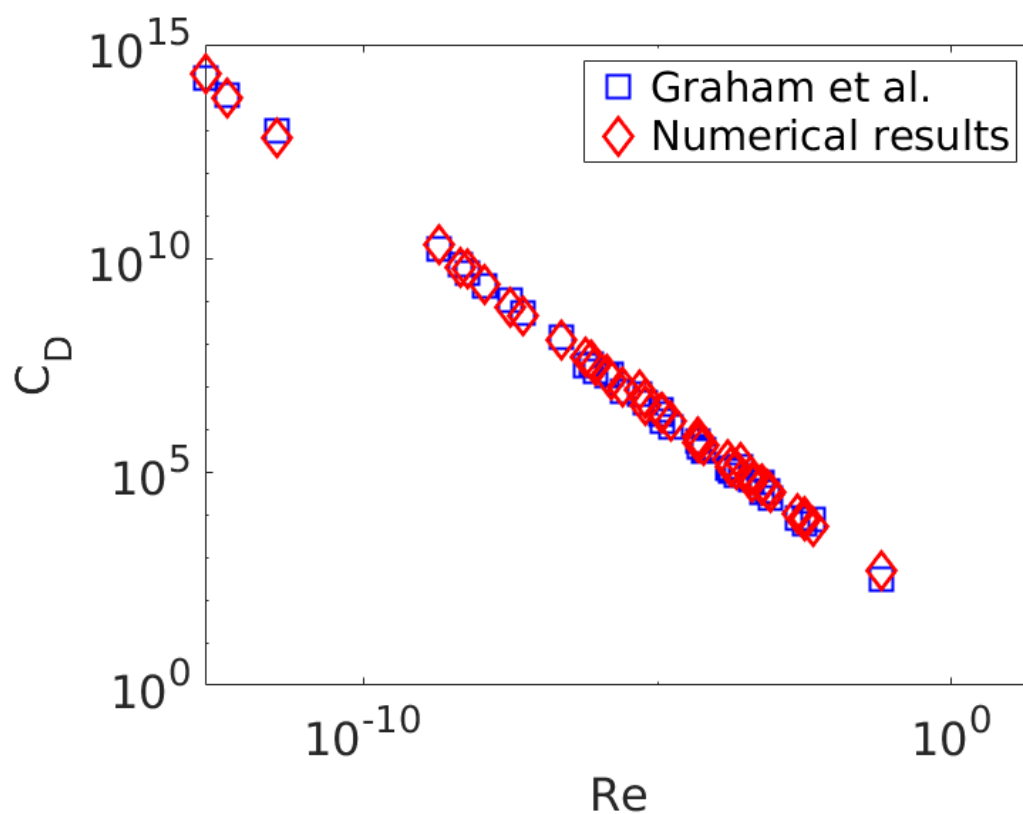


Figure 4.2: Comparison with Graham and Jones (1994) for $0.2 \leq Re \leq 1$

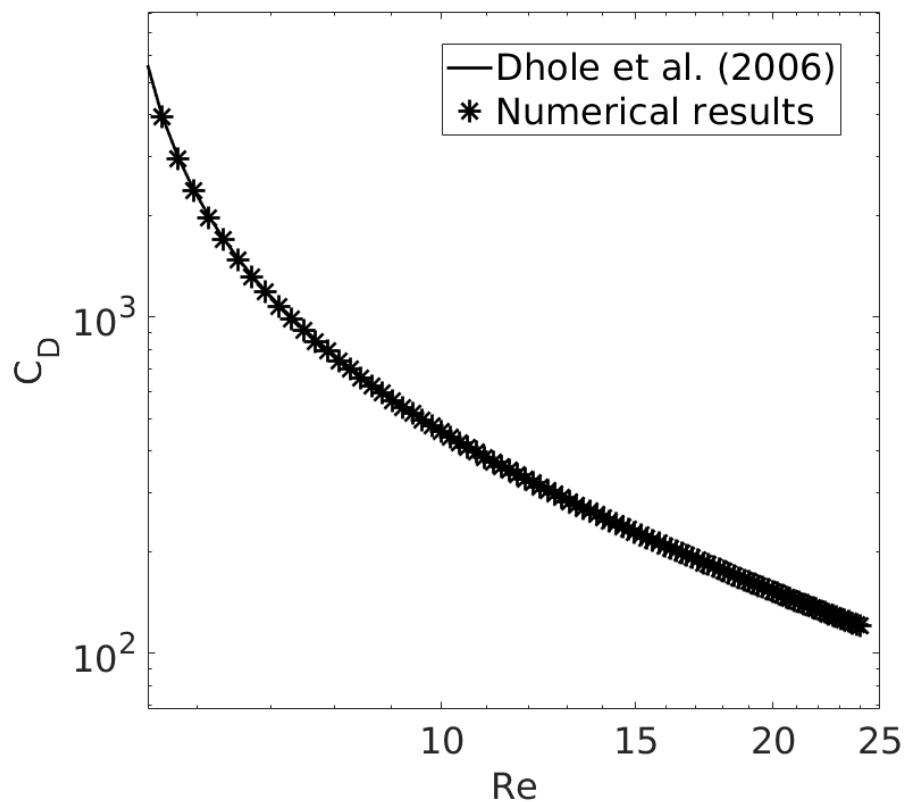


Figure 4.3: Comparison of our numerical results with Dhole *et al.* (2006) for $5 \leq Re \leq 24$

Results from Graham and Jones (1994) and Dhole *et al.* (2006) were compared. It was found that the experimental results by Graham and Jones (1994) agreed well within a maximum percentage difference of 13% with the numerical results. Although Dhole *et al.* (2006) presented an expression for Re range ($5 \leq Re \leq 250$) that was not covered in this study, attempts to compare the prediction by our model were made and found that it was within 5%. Atapattu *et al.* (1995b)'s prediction for creeping flow was also considered. Since Atapattu *et al.* (1995b) through his experiments confirms the prediction by Dazhi and Tanner (1985). We compared with Dazhi and Tanner (1985) and it matches with the predicted values within a maximum deviation of 5.06%. Comparison with Dazhi and Tanner (1985) is later discussed in this chapter since we use an approach that is slightly similar to theirs to present our results.

Therefore, the results here show good agreement with previously published correlations. This agreement provides clear evidence of the reliability of the computational model; it also suggests that subsequent results for settling under imposed shear will be similarly reliable. Although, further validation for settling under imposed shear will be undertaken to verify this.

4.2 Validation of sheared power-law fluids

After investigating an unsheared power-law fluid, we proceed to examine the sheared settling. Before investigating the sheared settling, we validate the model from two different sources, (i) experiments and (ii) analytical prediction.

From the validated model, we extend to present a functional form for predictions for a range of parameters in this study. Firstly, the predictions for the settling rate are presented in terms of the ratio of sheared settling velocity to unsheared settling velocity to quantify the scale-up of particle settling due to the induced shear. Secondly, the imposed shear is scaled without the unsheared shear rate scale to provide prediction.

4.2.1 Validation of sheared settling with analytical prediction

Childs (2013) developed an analytical expression for creeping flow with the particle settling in flows of power-law fluids with an applied background shear (Γ). The settling velocity was found to have two distinct dependencies on a dimensionless combination

of the flow parameters, that corresponded to regimes of dominant background shear flow or settling force of the particle. Using dimensional analysis, the dimensionless settling velocity, \hat{u}_s related to actual settling velocity, u_s which is given by

$$u_s = \left\{ \frac{(d/2)^{(n+1)} \Delta \rho g}{k} \right\}^{\frac{1}{n}} \hat{u}_s \quad (4.3)$$

Similarly, background shear rate is non-dimensionalised as, Λ , that is the ratio of the timescale of the particle settling velocity to that of the background shear rate. Λ is given by

$$\Lambda = \frac{1}{\Gamma} \left\{ \frac{d^3 \Delta \rho g}{2k d^2} \right\}^{\frac{1}{n}} \quad (4.4)$$

The dimensionless settling velocity, \hat{u}_s is expressed as a function of two dimensionless parameters Λ and n .

$$\hat{u}_s = f(\Lambda, n) \quad (4.5)$$

$$\hat{u}_s = \alpha(n) \Lambda^{n-1} + \beta(n) \quad (4.6)$$

where α and β are fitting constant for different flow index, n , the numerical values of which can be seen in Table 4.1.

Table 4.1: Value of fitting constants, α and β for the Equation 4.6 for various flow index given by Childs (2013)

n	α	β
1	0	2/9
0.8	0.18	0.055
0.6	0.22	0.023
0.4	0.24	0.0029
0.2	0.28	$8.4e^{-6}$

This settling law was shown to provide a good approximation of the variation in the settling velocity with Λ over a wide range of Λ . By comparing our numerical settling velocity data with the empirical settling law given in Equation 4.6, the results in this work are in good agreement, as can be seen in Figure 4.4.

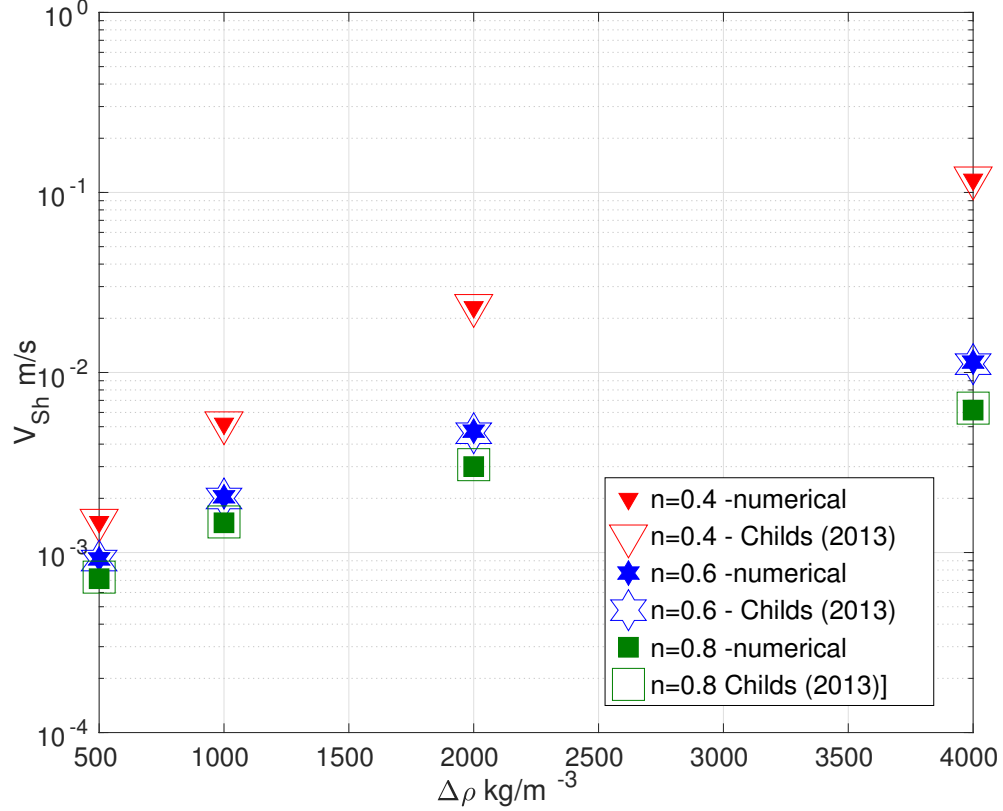


Figure 4.4: Comparison of numerical results for $0.4 < n < 0.8$ with Childs (2013) for a range of $\Delta\rho$ (500–4000)

We found good agreement with prediction by Childs (2013) for low Re . Although Childs (2013) examined particle settling with a background shear, it was only for creeping flow regime. Our work extends to laminar flow regime of the range $0.001 \leq Re \leq 1$. Before we proceeded with our numerical investigation, another set of validation was performed using experimental measurements by CSIRO to ensure the reliability of the model.

4.2.2 Validation of sheared settling with experiments

To investigate settling under imposed shear, we also validate the computational model against experimental data for settling velocity in a sheared yield pseudo-plastic fluid by using the experimental technique described in §3.11. Although this fluid that is described with a rheology model is different from that which is considered in this study,

it is still a shear-thinning fluid and the only reliable data that is available. A comparison, in this case, will provide a solid basis for validation. Experimental measurements were made by using the Herschel–Bulkley fluids detailed in Table 3.4 for a range of imposed-shear rates. In the experiments, plane shear was imposed by placing moving conveyor belts in a settling tank with width, D . The conveyor belts move in opposite directions at velocity, ‘ W ’, imparting a shear rate of $2W/D$ on the particle. Imposed shear is increased either by decreasing the distance between the conveyor belts or when the belt speed increases. Experimental measurements were available for Herschel–Bulkley fluids ($\tau_y = 9.76$; $k = 2.41$; $n = 0.48$) for a range of imposed shear rates (0 – 16.5 s^{-1}) on the particle sizes 4.7 and 3.96 millimetres. For each particle and applied shear rate, a minimum of five runs were measured and averaged. The experimental measurements were compared with our predictions by the model. The comparison, which is shown in Figure 4.5, shows that there is good agreement, with a maximum discrepancy of 10% . On the basis of this agreement, we conclude that both our overall modeling approach that is discussed in Chapter 3, and the OpenFOAM implementation of the Herschel–Bulkley model can reliably model the settling of the spherical particles in non-Newtonian fluids (for a broad spectrum of rheology parameters) as well as different fractions of imposed shear.

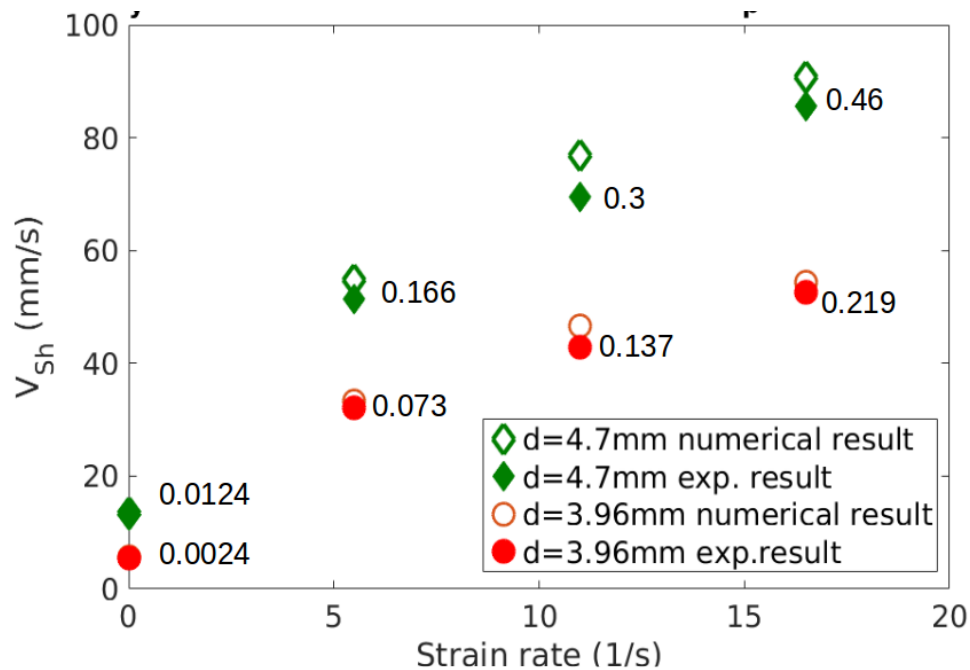


Figure 4.5: Comparison between the experimental settling rate in sheared medium and that measured by the numerical study. Fluid rheology: $\tau_y = 9.76 \text{ Pa}$, $k = 2.41 \text{ Pa s}^n$, $n = 0.48$, $\rho_p = 8042 \text{ kg/m}^3$. The corresponding Re for the settling rate is denoted beside the solid marker.

As can be seen in §4.2.1 and §4.2.2, the model is in good agreement with Childs (2013) and CSIRO experiments. This provides the confidence that is needed to proceed with our numerical investigation over a range of rheology parameters relevant for mining slurries and to provide predictions for higher Reynolds numbers that are unexplored.

4.3 Flow field

4.3.1 Unsheared settling

Drag depends on n , Re and δ' , however the base cause of these differences is the underlying flow field. To understand the effect of Re on settling flow structures, the velocity and viscosity fields for flow around the particle under unsheared conditions for low and high Re were compared. Further information on the structure of the detailed flow field can also be obtained by examining the streamline patterns for different values of the dimensionless system parameters.

A typical flow field for a power-law fluid, is shown in Figures 4.6 to illustrate differences in the variation of the y -component of velocity for the flow index ($n = 1$ and 0.5) and the Reynolds number ($Re = 1$ and 50). Due to the no-slip boundary conditions, the velocity magnitude is zero around the particle surface, and its magnitude increases across the fluid domain.

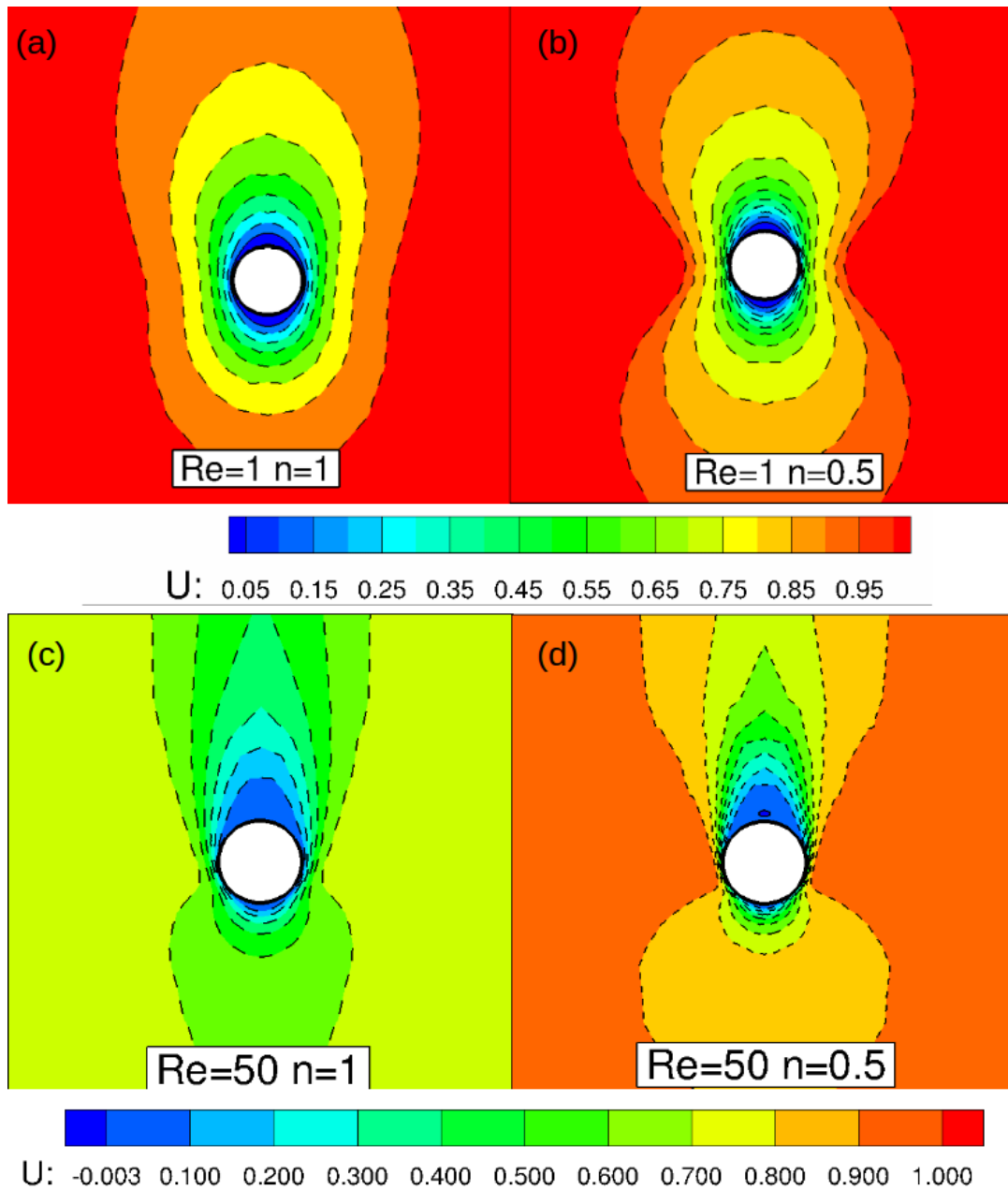


Figure 4.6: Contours of y -component velocity for (a) $Re = 1$; $n=1$, (b) $Re = 1$; $n=0.5$, (c) $Re = 50$; $n=1$, and (d) $Re = 50$; $n=0.5$

We can see from Figure 4.7-(left) that there is obvious symmetry around the particle surface for $Re \sim 1$. At a higher Re , the symmetry breaks, as can be seen in Fig 4.7-(right).

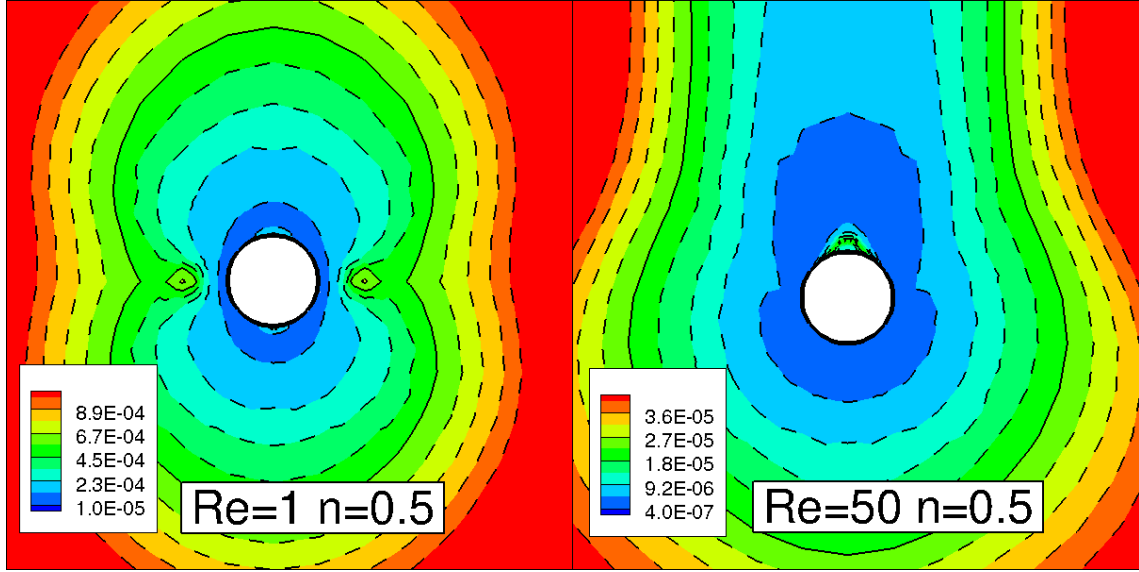


Figure 4.7: Viscosity contours for $Re = 1$ (left) and $Re=50$ (right) for $n = 0.5$.

As shown in Figure 4.7, the viscosity is, unsurprisingly, the lowest around the surface of the sphere (except at the rear stagnation point). The high-viscosity exterior fluid at the particle sides indicates low shear region.

4.3.1.1 Flow separation

At around the surface of the particle, flow separation causes the viscous drag to become negative and the pressure drag to increase. This results in a total increase in the drag in shear-thinning fluids. We noticed that a wider wake causes an increase in the pressure drag. The width of wake area keeps increasing as we move towards the shear-thinning nature of the fluids, that is, $n < 1$. At a low Re , streamline profiles indicate that the flow is attached to the surface of the sphere. At a higher Reynolds number (here, $Re \sim 50$), we observe a region of negative velocity, when the flow separates and turns to flow backward at a stagnation point, as can be seen in the Figure 4.8.

As we compare low Re ($Re = 1$) to high Re ($Re = 50$), we observe flow separation for $Re \leq 40$ for all values of n that are covered in this study, as shown in Figure 4.8. There is a critical point in the Re range (for each n) beyond which flow separation starts. For low n , it was observed that the critical Re at which the flow separation is below the Newtonian range. The critical Re beyond which the flow separates is around 30 for the lowest n covered in this study.

Streamline patterns here exhibit behaviour that is similar to the findings from the literature. This shows that a complete fore and aft symmetry prevails in the creeping flow region, whereas a wake appears in the rear of the sphere at about $Re \sim 20-30$, this wake grows in size with increase in the Reynolds number.

The effect of the flow index on the streamline patterns for a sphere is found to be small, except for the fact that the wake formation is delayed for increasing n , and the resulting wakes are slightly smaller in size than those in the case of a Newtonian fluid.

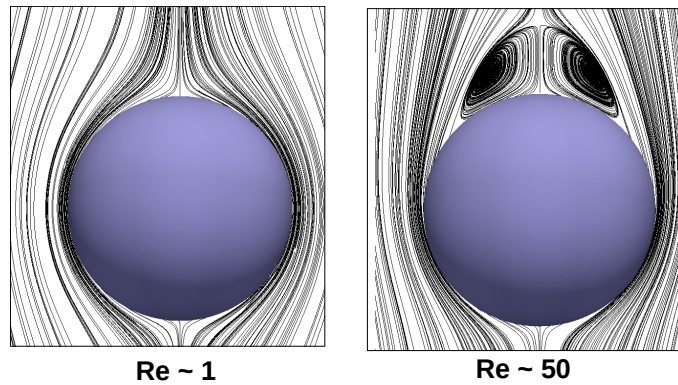


Figure 4.8: Effect of Re on streamline contours for $n=0.5$ showing flow separation for higher values of Re

For example, when $n = 0.3$, the critical Re beyond which the flow separation lies between 25-30, and it increases as the flow index increases. We also observe that the recirculation length increases for higher Re and for decreasing n . In Figure 4.9, for increments of Re , the flow separation for a given flow index (in y axis) is indicated by an ‘o’ and the unseparated flows by ‘x’.

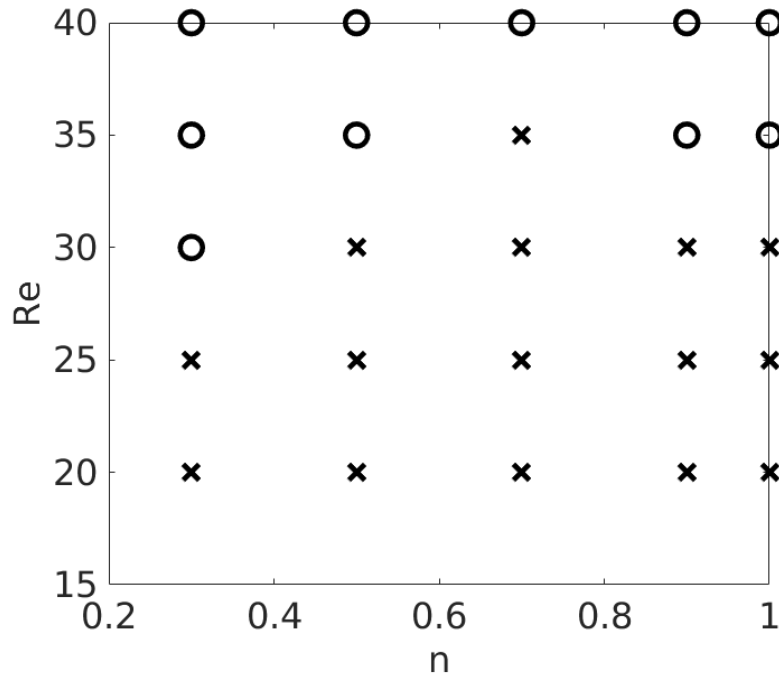


Figure 4.9: Flow separation map as a function of n and Re . Separated flow indicated by 'o' and the unseparated flows by 'x' at higher Reynolds number for various flow index.

4.3.2 Sheared settling

The application of external shear to a shear-thinning fluid through which a particle is settling will modify the viscosity and hence velocity field at the particle surface. In turn, these changes will modify the distribution of surface forces on the particle and thus the total drag. Because the steady-state settling velocity is a balance between drag and body forces, we expect the application of shear to modify the settling velocity. The aim of this section is to begin to quantify the way in which applied shear (here characterised by δ') changes the settling velocity and the coefficient of drag.

Before quantifying the effect of applied shear, we first present a qualitative picture in terms of the flow field so that the key generic features can be clearly understood. It is worthwhile to examine the differences in the velocity y -component between $Re=0.001$ and $Re=1$ for various n and at the highest δ' that has been covered in this study.

For rheology where $n = 0.5$, a comparison between the sheared flow field ($\delta' = 1$) and unsheared flow field is shown in Figure 4.10. A significant increase in velocity and a decrease in viscosity in comparison to those in the unsheared case can be clearly seen.

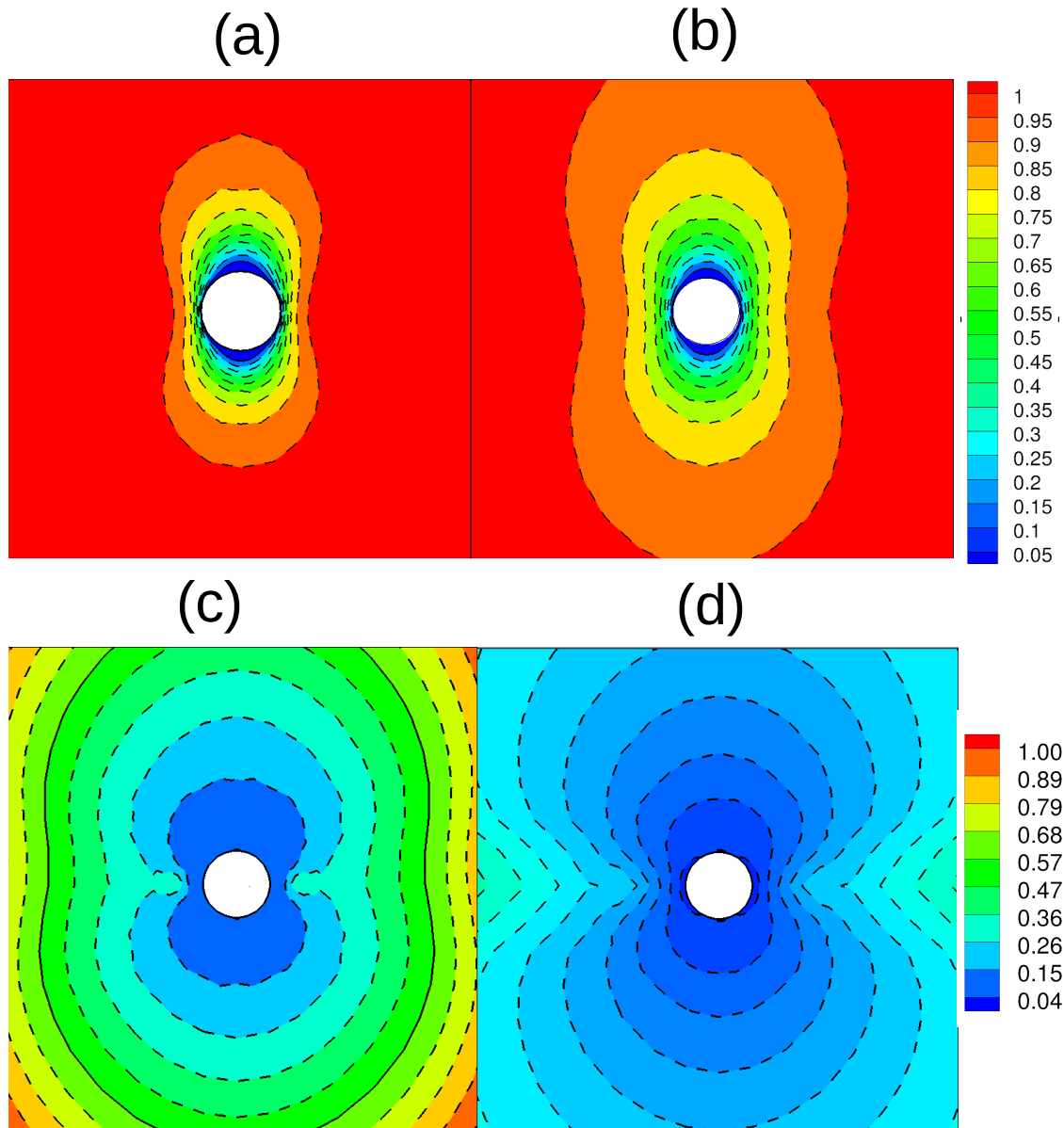


Figure 4.10: Contours of (a) unsheared velocity y component (b) sheared velocity y component ($\delta' = 1$) (c) unsheared viscosity distribution (d) sheared viscosity distribution ($\delta'=1$) (for $Re = 1$, $n = 0.5$)

For an imposed shear of $\delta' = 1.0$, $Re \approx 0.001$ and $Re \approx 1.0$, $n=1.0$, the velocity on the centre plane is shown in Figure 4.11. The particle surface shows zero velocity because the boundary condition is applied and we observe that the velocity is uniformly distributed along the flow domain.

A similar flow pattern for sheared settling at $n=0.9$, $n=0.7$, and $n=0.5$ is found; that is, the velocity magnitude is the minimum around the particle surface, and it increases uniformly across the domain length, as can be seen in Figure 4.12, 4.13 and 4.14.

When we see the velocity field from the least shear-thinning fluid to the most shear-thinning fluid, the uniform expansion is shortly attained as we move along the more shear-thinning fluid. The contour scale that displays mentioning '0.9' in 4.11, 4.12, 4.13 and 4.14 shrinks as n increases; and it further shrinks at a higher Re .

It is interesting to note that the onset of velocity attaining "uniformly even" is shorter at $Re=1$ at a lower Re . Similarly, at a low n , becomes uniformly faster than Newtonian fluids.

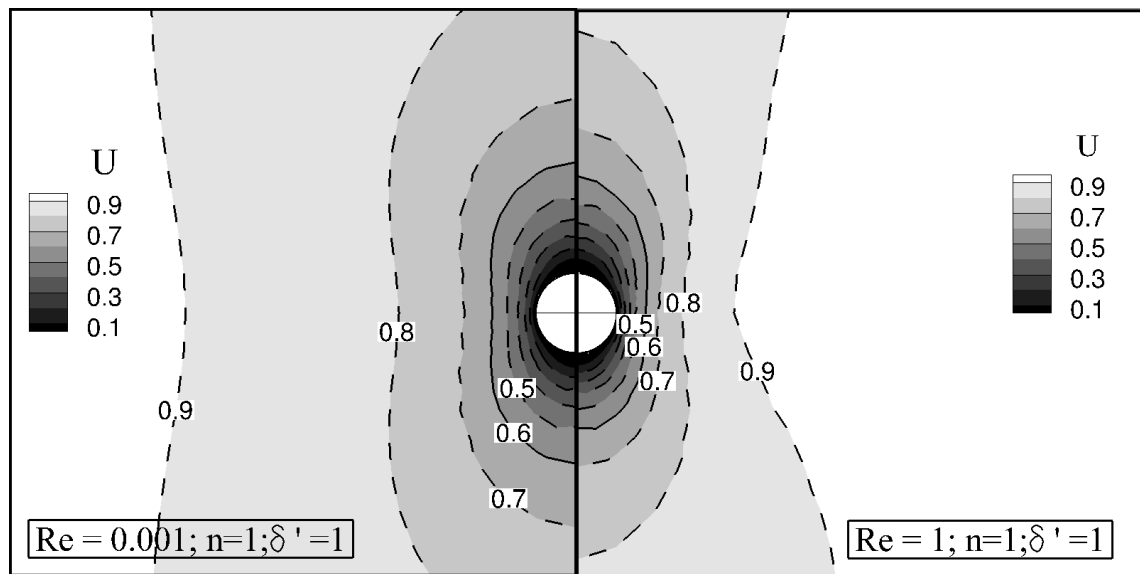


Figure 4.11: Velocity contour for $Re=0.001$ and $Re=1$ at $\delta' = 1$ and $n = 1$

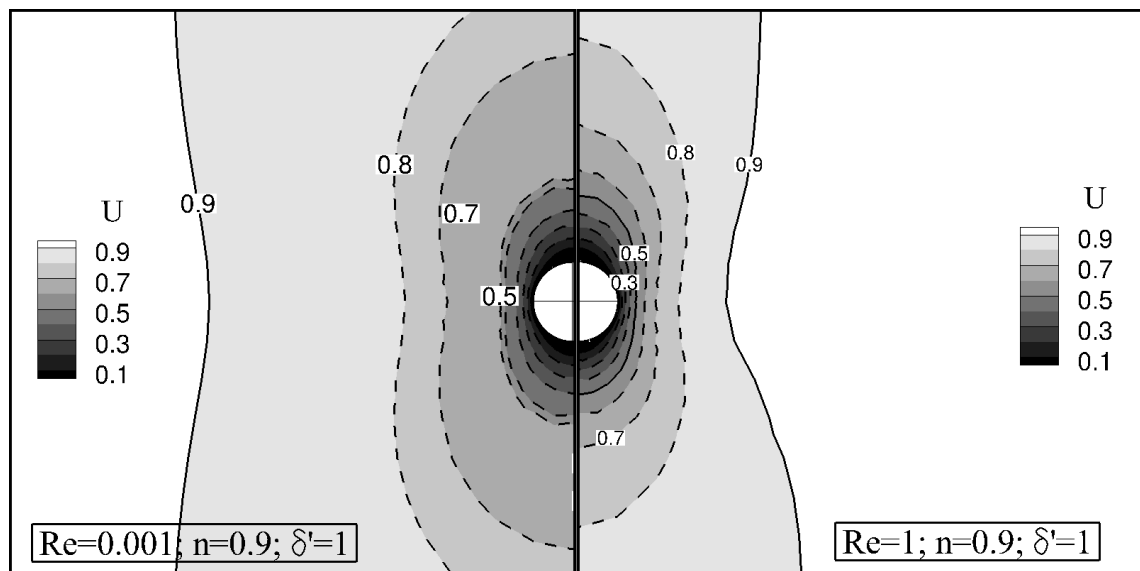


Figure 4.12: Velocity contour for $Re=0.001$ and $Re=1$ at $\delta' = 1$ and $n = 0.9$

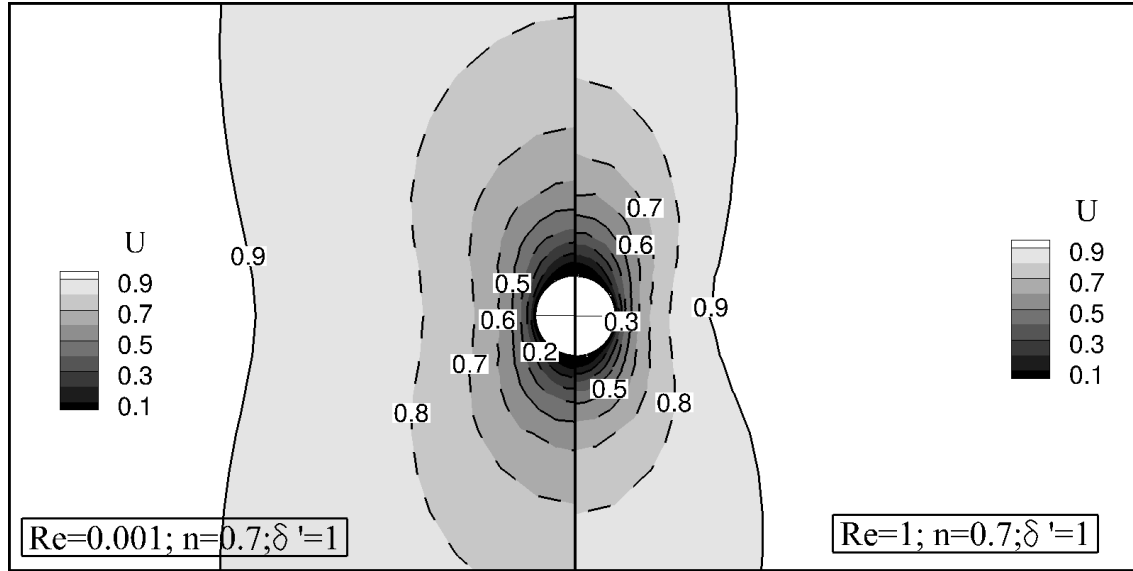


Figure 4.13: Velocity contour for $Re = 0.001$ and $Re = 1$ at $\delta' = 1$ and $n = 0.7$

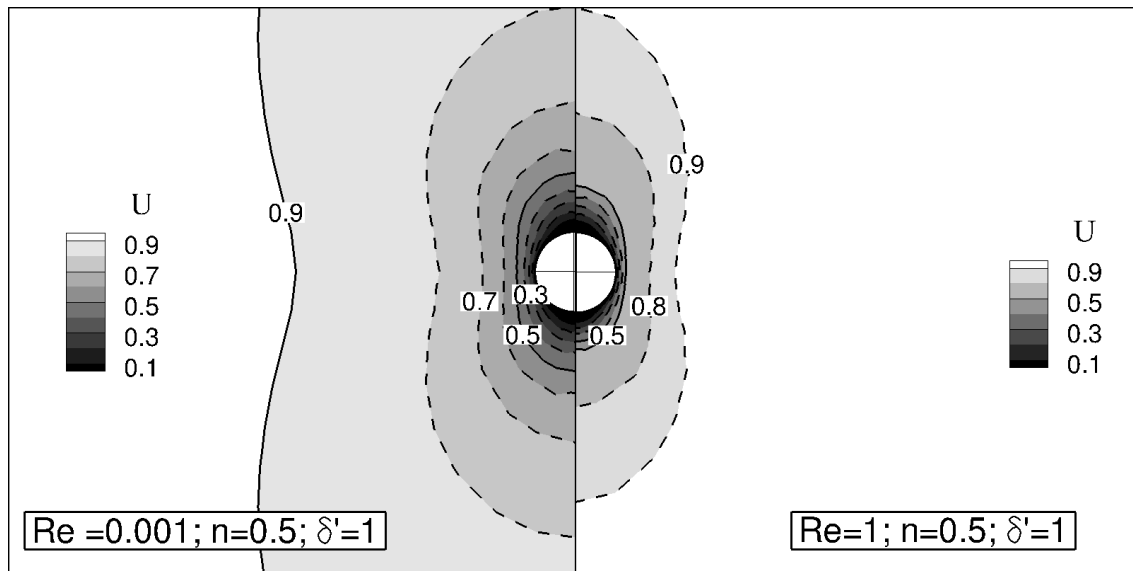


Figure 4.14: Velocity contour for $Re = 0.001$ and $Re = 1$ at $\delta' = 1$ and $n = 0.5$

4.3.2.1 Comparison between maximum and minimum Re / δ'

Under sheared conditions, one way to better understand the effect of Re on δ' is to subtract the two fields and plot the difference. The distinction between two flow fields is achieved by considering a point-wise differencing of the image at the same scale. In this way, we are able to identify the flow pattern differences between the different conditions in this study. As mentioned earlier, this comparison study is conducted in two categories; the difference between (i) high and low Re and (ii) high and low δ' . The former category is discussed in Section §4.3.2.2, and the latter in Section §4.3.2.3, respectively.

4.3.2.2 Effect of Reynolds number

For the velocity field between $Re=1$ and $Re=0.001$ for a given flow index and δ' , we notice two things. Firstly, the flow field is zero on the particle surface, as expected. Secondly, we observe that the zero (in dark blue) field after differencing after uniformly decreasing from the particle surface as can be seen in Figure 4.15. For low n , the high difference zone (in pink and red) reduces due to the shear-thinning behaviour of the fluid.

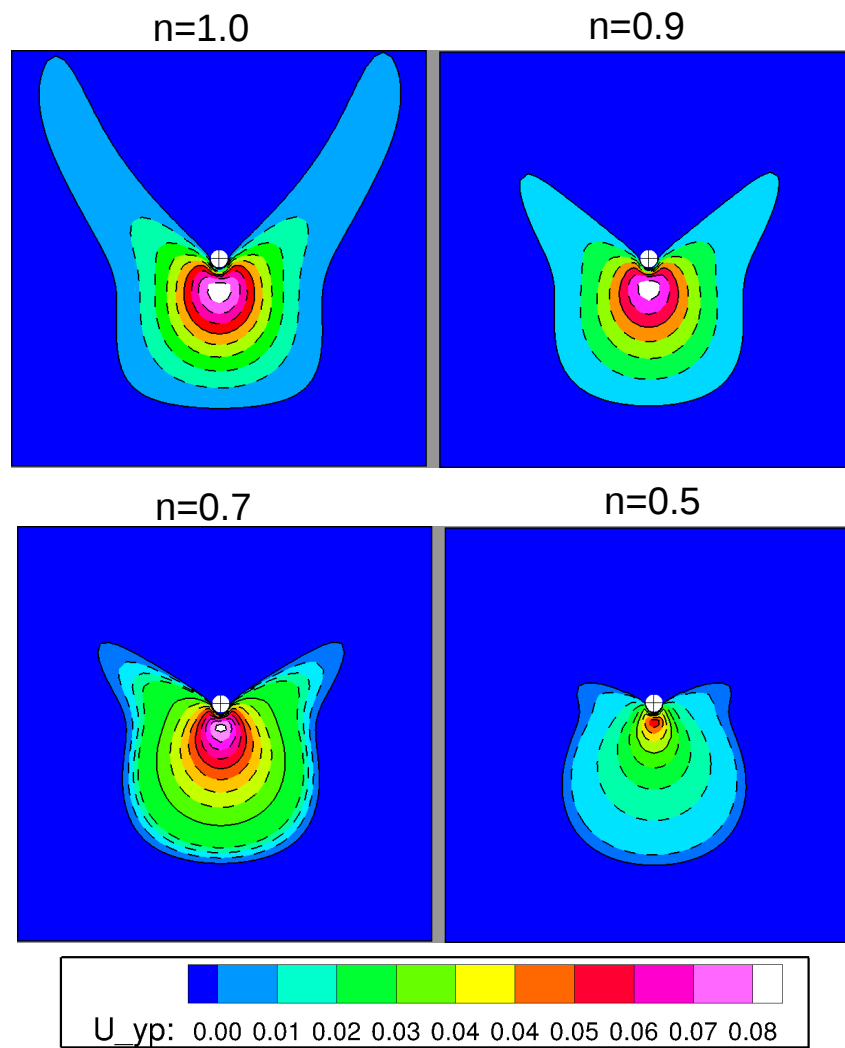


Figure 4.15: Comparison between contour of y - component of velocity at $Re=0.001$ and $Re=1.0$ for $\delta' = 0.1$

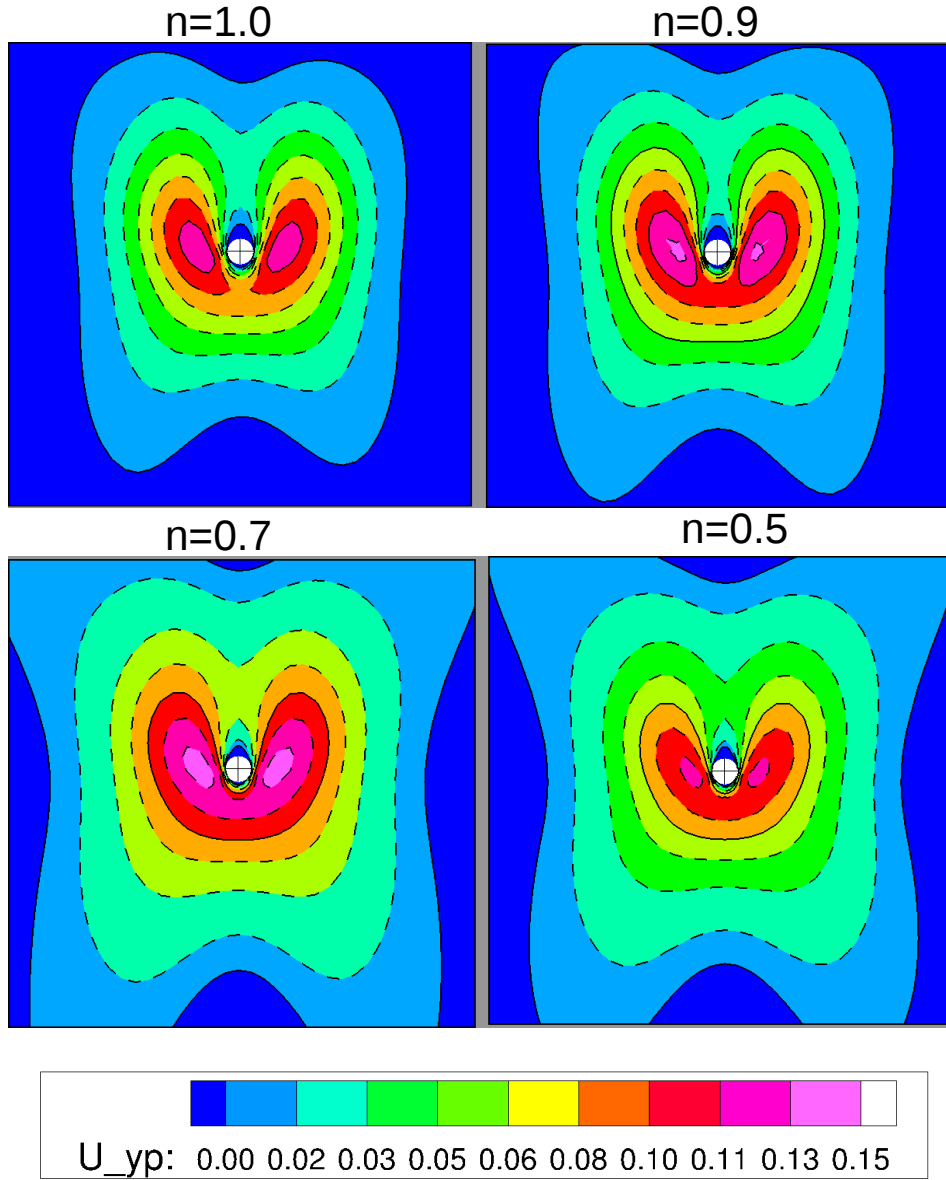


Figure 4.16: Comparison between contour of y - component of velocity at $Re=0.001$ and $Re=1.0$ for $\delta' = 1$

We examine by comparing the velocity contour at the minimum non-zero δ' covered in this study. We also investigate by comparing the velocity contour at the maximum δ' , that is, $\delta' = 1.0$. Similar to Figure 4.15, in this case, we observe that in Figure 4.16 the high difference region reduces as n uniformly decreases and becomes zero everywhere.

4.3.2.3 Effect of imposed shear

For a given Re , by analysing the contours' difference between $\delta' = 0.1$ and $\delta' = 1$ in Figure 4.17, it can be seen that as we note a greater amount of shear-thinning fluid from $n=0.9$ to $n=0.5$, we observe a highly sheared region beside the particle due to the shearing wall speed, W . Additionally, around the particle surface is zero as it becomes more shear thinning.

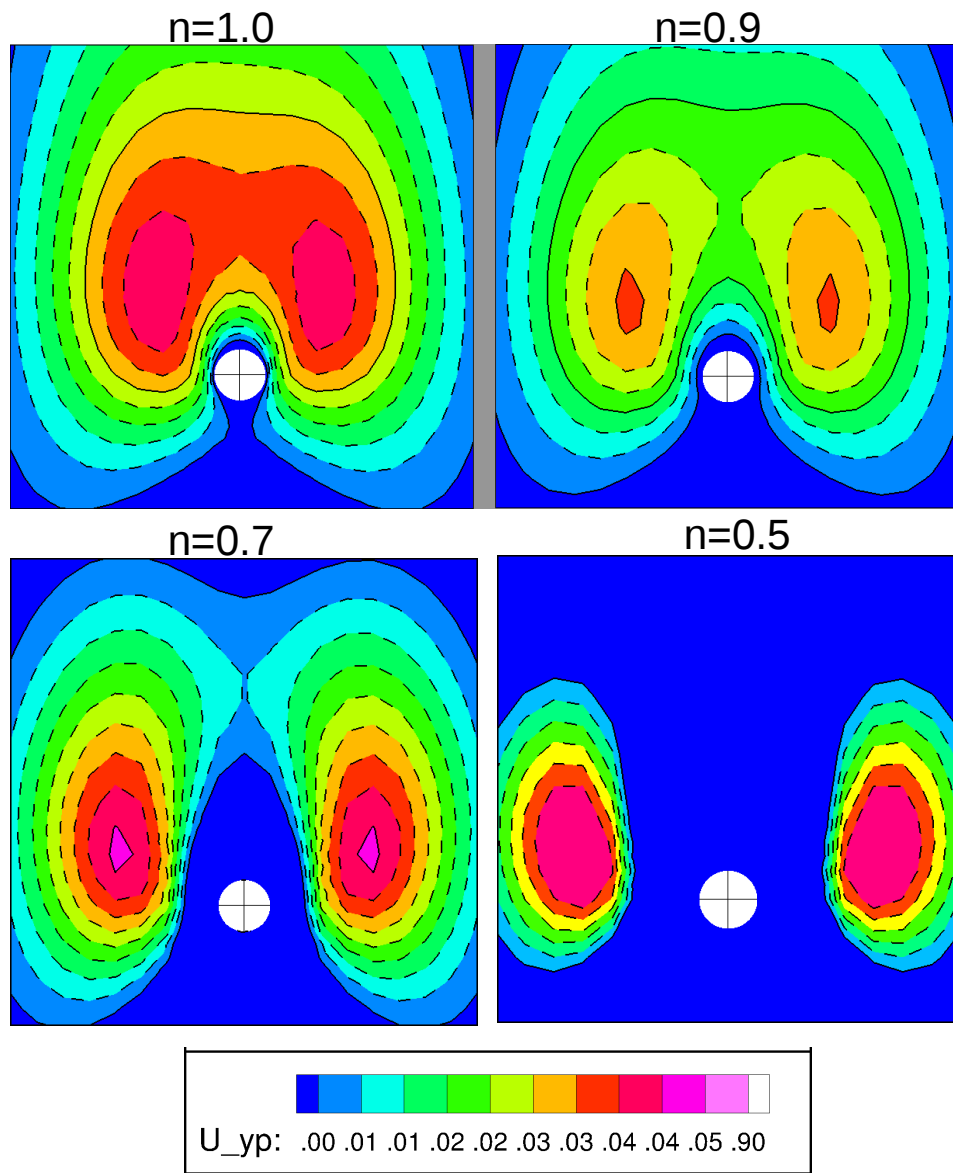


Figure 4.17: Comparison between contour of y - component of velocity at $\delta' = 0.1$ and $\delta' = 1$ for $Re=1$

Examples of the flow field results with $\delta' = 0$ and $\delta \neq 0$ proves the significance of the applied shear across the fluid domain and as a result of which the particle settling is affected. We now proceed to investigate the results in terms of drag coefficient, C_D or settling rate, V_{Sh} and quantify in terms of the range of parameters covered in this study.

4.4 Results

Imposed shear increases the settling rate of the particle in shear-thinning power-law fluids. We examine the manner in which different imposed shears, when combined with the natural settling due to gravity, create an impact due to the shear-dependent fluid on the particle.

4.4.1 Non-dimensionalising imposed shear

Since applied shear modifies viscosity in the neighborhood of the particle, and it has already been shown to affect the settling velocity by Childs (2013), the aim of this section to quantify the effect of shear. It is expected that results can be collapsed by suitable non-dimensionalisation, and two different non-dimensionalised parameters are considered.

First, the applied shear (specified by velocity difference divided by box size) is compared to a normal shear rate, which is given by the settling velocity without shear (V_U) divided by the particle diameter, d . The non-dimensional shear is then given by

$$\delta = \frac{2W/D}{V_U/d} \quad (4.7)$$

where W is the shearing plane velocity, D is the domain size, d is the particle size, and V_U is the unsheared settling velocity.

Secondly, the applied shear is compared to the shear rate that is given by settling with shear (V_{Sh}) divided by d . The non-dimensional shear is then given by

$$\delta' = \frac{2W/D}{V_{Sh}/d} \quad (4.8)$$

where V_{Sh} is the settling velocity with imposed shear.

Using the dimensionless imposed-shear to vary the fraction of imposed-shear, we conduct a numerical investigation of particle settling in power-law fluids. Based on this

dimensionless parameter, we quantify the increase in the settling rate and also the drag coefficient decrease.

4.4.2 Functional form for the settling rate in an unsheared medium

The Stokes settling velocity for a Newtonian fluid (V_{St}) is given by Equation 4.9. We present an expression for settling velocity prediction, which is similar to Eqn 4.9 for the range of Re covered in this study. Instead of the constant $1/18$ and η in the Eqn 4.9, we introduce $C = f(n)$ and power-law viscosity, respectively to obtain an expression for settling velocity for power-law fluid in an unsheared medium (V_U), as shown in Eqn 4.10.

$$V_{St} = \frac{1}{18\eta} g d^2 \Delta\rho \quad (4.9)$$

$$V_U = \left(\frac{C g \Delta\rho d^{n+1}}{k} \right)^{1/n} \quad (4.10)$$

The value of C in Eqn 4.9 is equal to $1/18$ in a Newtonian Stokes flow. By incorporating the shear rate scale as V_U/d in the power-law viscosity (see Eqn 2.1), Equation 4.10 is obtained. The value of C, in this study, was investigated in a range of rheologies and density differences. For creeping flow regime, it is found that the value of C is a function of the flow index and its function is given by Equation 4.11. Therefore, the expression for V_U is given by Equation 4.12.

$$C = \frac{1}{18X_{Un}} \quad (4.11)$$

$$V_U = \left(\frac{\Delta\rho g d^{n+1}}{18k X_{Un}} \right)^{1/n} \quad (4.12)$$

In order to account the value of C for the unsheared power-law fluids, a correction factor X_{Un} is introduced as a function of flow index n and its values are tabulated in Table 4.2. A similar approach of X_{Un} in the creeping flow limit was given by Dazhi and Tanner (1985) and their values listed in Table 4.3. The value of X_{Un} from our numerical results was compared with Dazhi and Tanner (1985) and the results show good agreement, as shown in Figure 4.18.

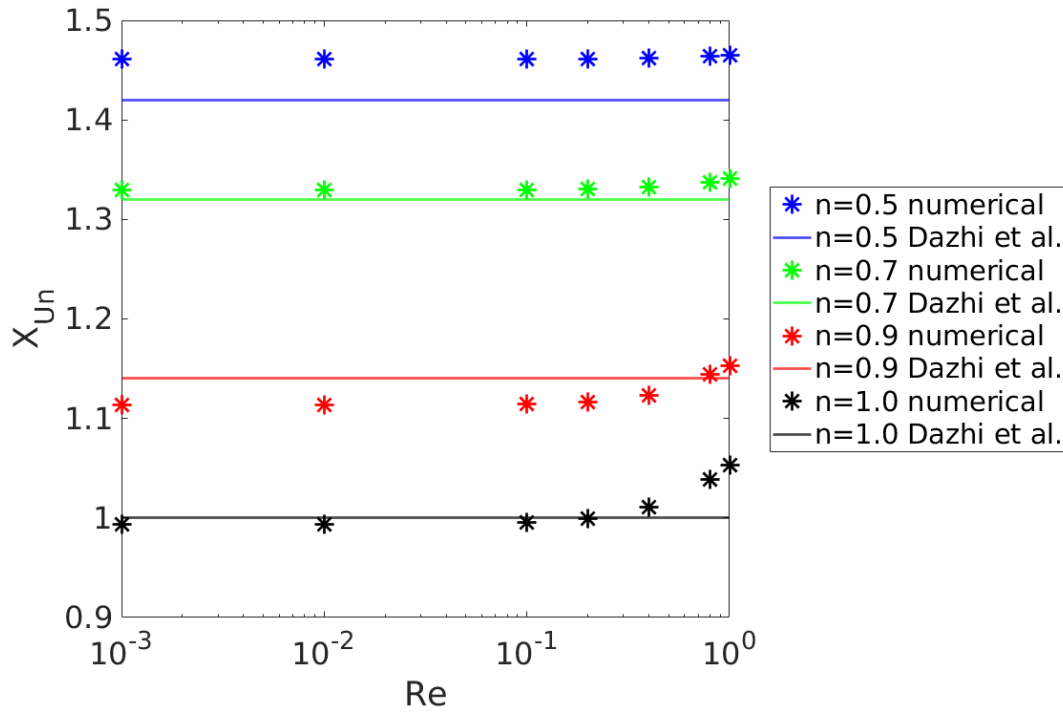


Figure 4.18: Comparison with Dazhi and Tanner (1985) and our numerical measurements

The results were compared with Dazhi and Tanner (1985) in Figure 4.18. The drag coefficients from the results and literature were compared, and the results were found extremely consistent, with a maximum difference of $\sim 5.06\%$ between them, as can be seen in Figure 4.18. In addition, the values compare well with the experimental measurements by Leclair (1970), Chhabra (1993) and Jaiswal et al.(1991).

n	X_{Un}
1	1.00
0.9	1.113
0.7	1.33
0.5	1.461

Table 4.2: The values of the drag correction factor X_{Un}

n	$X_{Un \text{ Tanner}}$
1	1.00
0.9	1.140
0.8	1.240
0.7	1.320
0.6	1.382
0.5	1.420
0.4	1.442
0.3	1.458
0.2	1.413

Table 4.3: X_{Un} given by Dazhi and Tanner (1985) for unbounded flow

4.4.3 Functional form for the settling rate in a sheared medium

At any imposed shear on the particle, the local shear in the entire flow, particularly in the vicinity the particle, is affected. As expected, the low viscosity region around the particle aids in faster settling than in an unsheared medium. To quantify the tendency of the particle to settle faster under sheared conditions, we apply shear based on δ .

The results for a one-millimetre of particle settling in sheared power law fluids with $n = 0.3$ and 0.7 for $100 < \Delta\rho < 2000$ and $0.1 < \delta < 10$ are shown in Figure 4.19. As can be seen, for a given rheology, as the imposed shear rate ratio δ increases, the particle settling velocity also increases. As expected, the impact of the imposed shear, δ , decreases the viscosity across the entire computational domain, but the local effect in the vicinity of the particle enables the particle to settle faster.

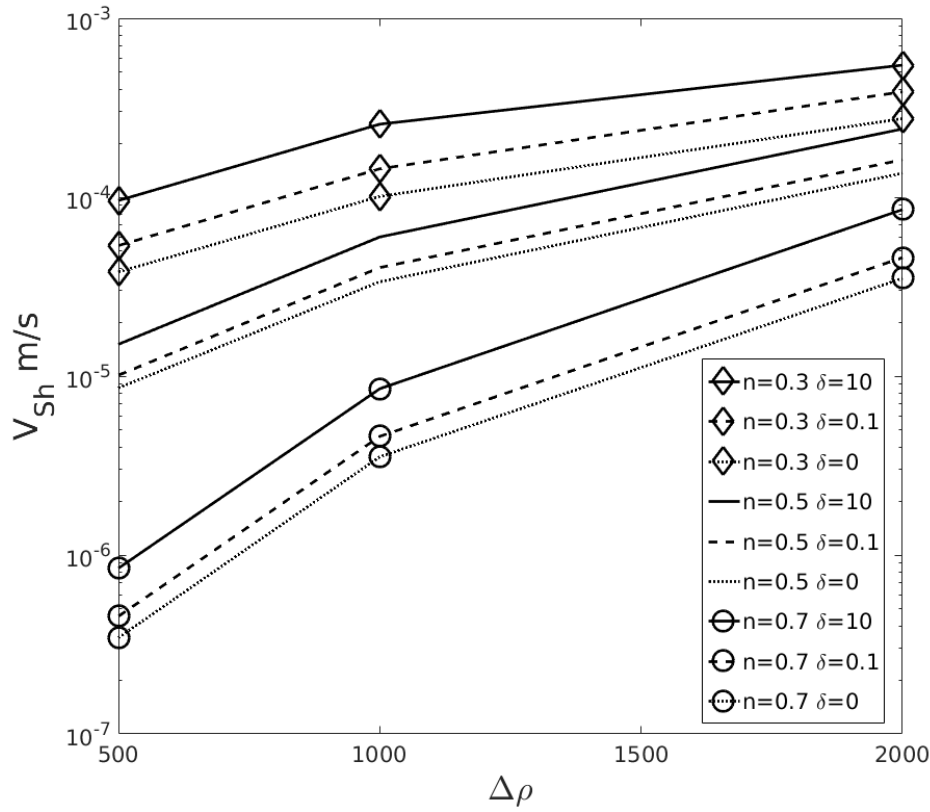


Figure 4.19: Settling velocity as a function of density difference for different δ .

4.4.3.1 Ratio of sheared to unsheared settling velocity

We present the results of sheared settling in terms of the ratio of the settling velocity in the case of imposed shear (V_{Sh}) with that in the unsheared case (V_U). The results of V_{Sh}/V_U for a given value of k ($= 2.0 \text{ Pa s}^n$) are shown in Figure 4.20a as a function of the imposed shear rate ratio, δ . Important to note is that each of the curves in Figure 4.20a is indistinguishable for every density ratio considered, that is, the results in Figure 4.19 for a fixed n collapse for all $\Delta\rho$. This then means that the results appear to be independent of Re , at least over the range of Re of the simulations (10^{-6} to 1). The second result is that, similar to the results in Figure 4.19 for V_{Sh} , the ratio, V_{Sh}/V_U , increases with decreasing n , that is more shear-thinning fluid result in higher relative settling in a sheared fluid. Although not obvious from Figure 4.20a, our results also predict that the settling velocity of a Newtonian fluid is affected by applied shear, although this is quite a weak effect being approximated by $V_{Sh}/V_U = (1 + 0.003\delta)$.

The effect of consistency k (0.1, 2), on the ratio, V_{Sh}/V_U , is shown in Figure 4.20b for a single flow index, $n = 0.5$. Again, these results cover the full range of density

differences. It is clearly seen is that k has no direct influence on the ratio of sheared to unsheared settling velocities, which is a consequence of the viscosity being a linear function of k . It confirms that the ratio, V_{Sh}/V_U , is not a strong function of Re .

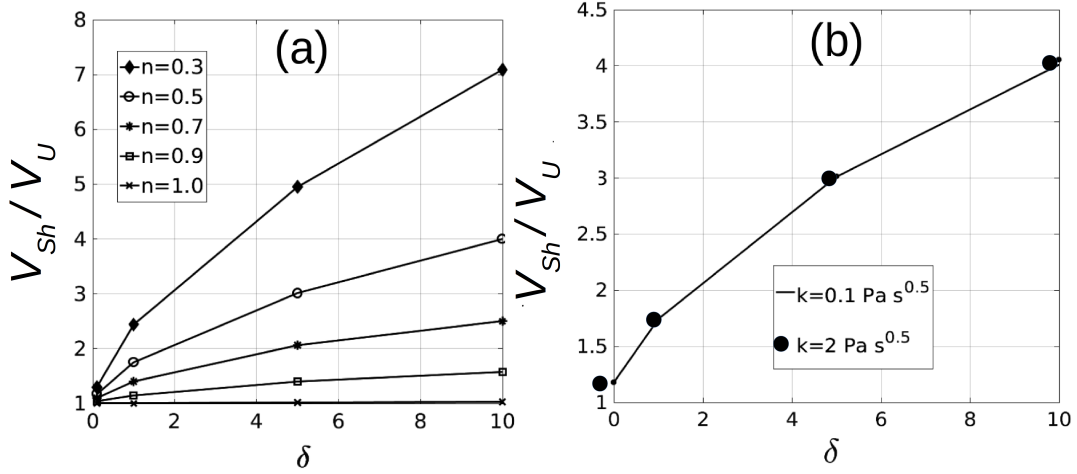


Figure 4.20: V_{Sh}/V_U a function of δ (a) for flow index $0.3 < n < 1.0$ at constant $k=2.0$ (b) for $k=0.1$ and 2 Pa s ^{n} at constant $n=0.5$

From the results for imposed shear, we observe that the velocity ratio is primarily a function of the imposed shear and the flow index. Based on this understanding, we collapse the data to determine the following unified correlation:

$$\frac{V_{Sh}}{V_U} = (1 + 0.003\delta)(1 + 1.56\delta)^{(1-n)} \quad (4.13)$$

Equation 4.13 incorporates the effect of shear due to both settling, and the imposed shear through δ ; the equation was obtained using non-linear least square regression analysis. The first term arises from a need to recover the Newtonian result. The functional form of the second term is based on the ratio of the viscosity scale, η_{Sh} (see Equation 4.15), in the case of the imposed shear to that in the unsheared case η_U (see Equation 4.14). This ratio takes the form, $(1 + a\delta)^{1-n}$, and it is used to determine the correlation.

$$\eta_U = k \left(\frac{V_U}{d} \right)^{n-1} \quad (4.14)$$

$$\eta_{Sh} = k \left(\sqrt{\left(\frac{V_{Sh}}{d} \right)^2 + \left(\frac{\delta V_U}{d} \right)^2} \right)^{n-1} \quad (4.15)$$

The surface that represents this fit of the velocity ratio as a function of δ and n is shown in Figure 4.21. It indicates excellent between the correlation and our results.

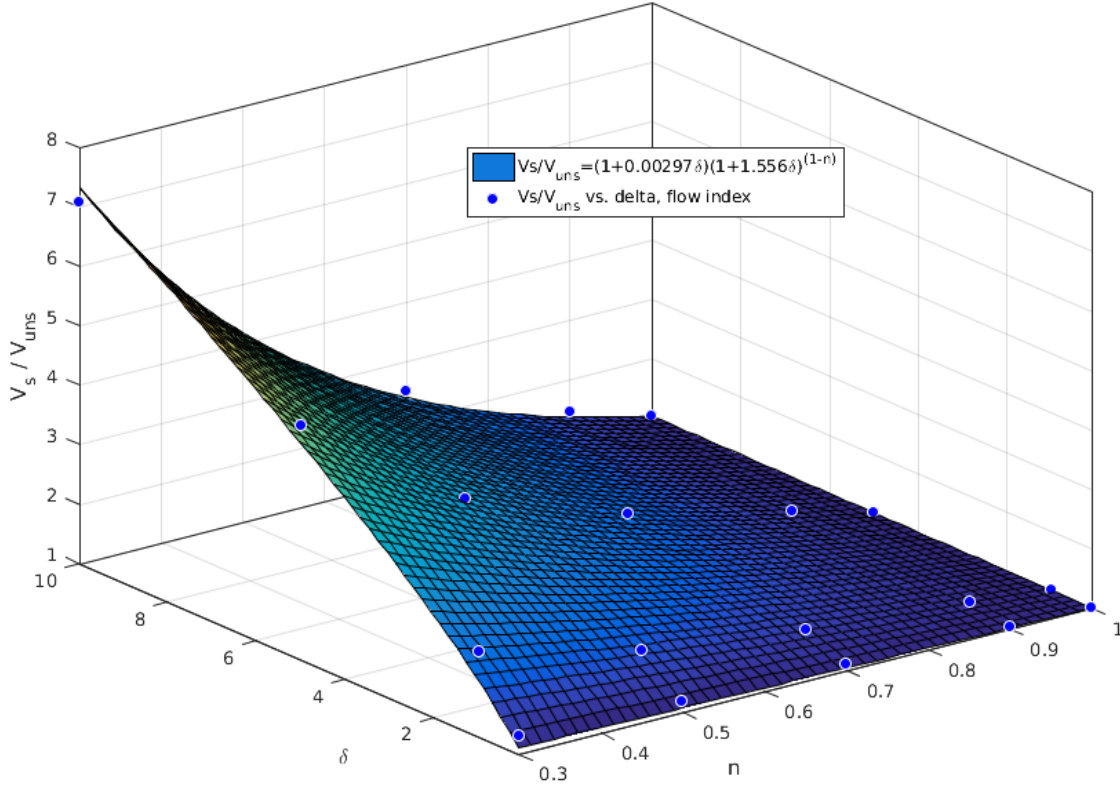


Figure 4.21: Surface fit for V_{sh}/V_U as a function of δ and n

4.4.4 Drag prediction

It is clear from the section described above that imposed shear has a significant influence on the particle settling rate. However, it is also important to discuss the drag that is exerted on the particle in the shear-thinning sheared medium. Therefore, for a deeper understanding of the drag force that is experienced by the particle under sheared conditions, an investigation of particle settling over a range of Re ($0.001 \leq Re \leq 1$), $0.1 \leq \delta' \leq 1$ and $0.5 \leq n \leq 1.0$ was carried out. The non-dimensional shear δ' is used here. To investigate without the use of unsheared data, we intended to use δ' , that is scaled with the sheared settling rate and imposed shear rate. However, our results based on δ collapsed with δ' and is discussed in the later section.

The drag on the particle in sheared power-law fluids, was obtained in the following order:

- Unsheared Newtonian fluid
- Unsheared power-law fluid
- Sheared Newtonian fluid
- Sheared power-law fluid

When developing an expression for C_D (or V_{Sh}) for sheared power-law fluids, there are a number of conditions that must be satisfied. First, as $\delta' \rightarrow 0$, the unsheared results must be recovered. Second, as $n \rightarrow 1$, the Newtonian results must be recovered. This suggest several possible ways of developing the required expression. The choice used here is (i) unsheared Newtonian, (ii) unsheared power-law fluid, (iii) sheared Newtonian fluid and, (iv) sheared power-law fluid. Therefore, the final correlation would satisfy all the conditions. In this section, we observe the manner in which each condition affects the particle drag in the order discussed above. We develop a consistent methodology to assimilate all the unsheared and sheared conditions into our prediction for drag.

To elucidate the sphere drag in different cases, we consider the study by Dazhi and Tanner (1985), which represents drag on a sphere in terms of the values of the drag correction factor, $X_{Un} = f(n)$, and Stokes drag coefficient, C_{St} , as written in Equation 4.16. The value of X_{Un} is shown in Table 4.2. We introduce a similar mechanism to illustrate our numerical data, and extend it to represent the effect of shear in an expression for future prediction.

$$C_D = X_{Un}(n)C_{St} \quad (4.16)$$

4.4.4.1 Drag prediction in the unsheared case

As mentioned previously, Dazhi and Tanner (1985) presented the settling behaviour of power-law fluids from Newtonian fluids through the inclusion of a dimensionless factor, X_{Un} . The drag results obtained for unsheared power-law is expressed in terms of X_{Un} , that is, C_D/C_{St} . The flow regime is considered valid for a low Reynolds number or a creeping flow, that is, Equation 4.16 is valid up to an Re of less than one (Tripathi *et al.* (1994)).

Although the work by Dazhi and Tanner (1985), with which our was model was compared and found to be in good agreement, it is valid only in the creeping flow regime.

When Re increases, we clearly see a trend of drag coefficient not longer equals $X_{Un} C_{St}$, as shown in Figure 4.22. When our data of higher Re ($0.001 \leq Re \leq 1$) was compared with Dazhi and Tanner (1985), the percentage difference was found to be around $\sim 5.06\%$.

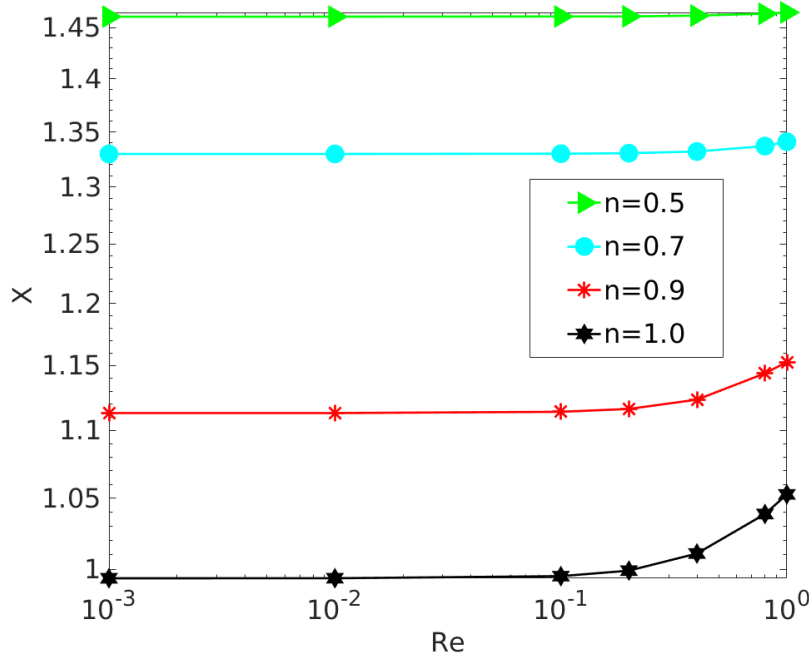


Figure 4.22: X versus $\log Re$ for the range: $0.001 \leq Re \leq 1$

To accommodate the slight dependency on Re , especially for high n , the Eqn 4.16 must be modified. We observe that the value of X , as written in Equation 4.17, does not behave as a constant for Re that is greater than 0.1 approximately, from the Figure 4.22. On this note, we proceed to predict by adding a first order term into the Equation 4.16, which will be valid for $0.001 \leq Re \leq 1$.

$$X = \frac{C_D}{C_{St}} \quad (4.17)$$

4.4.4.2 Unsheared Newtonian fluids

Our study examines Re that is less \leq one; therefore, we take into account the study by Clift *et al.* (1978) on Newtonian fluids to support our prediction for unsheared Newtonian fluids. Clift *et al.* (1978) presented an expression for C_D in an unsheared Newtonian fluid. We use a similar expression, that is, $(1 + A Re^B)$. From our computational results for drag, we predict an expression for particle settling in Newtonian fluids under an unsheared condition, as can be seen in Equation 4.18. The model for unsheared Newtonian fluids

was obtained using non-linear regression fit, and the value of fitting constants, $A = 0.06$ and $B=1.6$, were found. The accuracy was more than 99% with the data points.

$$X/X_{Un} = (1 + A Re^B) \quad (4.18)$$

where $A = 0.06$ and $B=1.6$

4.4.4.3 Unsheared power-law fluids

In order to predict a functional form for unsheared power-law fluids, we use the Equation 4.18, and we modify for power-law fluids by considering 'A' as a function of the flow index (say A'). Also, 'B' is considered a constant since the range of Re examined is $Re \leq 1$. From our results, by using data fitting, we obtain a value for A' . The functional form for unsheared power-law fluids is given by Equation 4.19, and its accuracy is well above 94 % with the measured points, as shown in Figure 4.23. As Equation 4.19 was modified from Equation 4.18, we see that the shear-thinning results collapse on Equation 4.18.

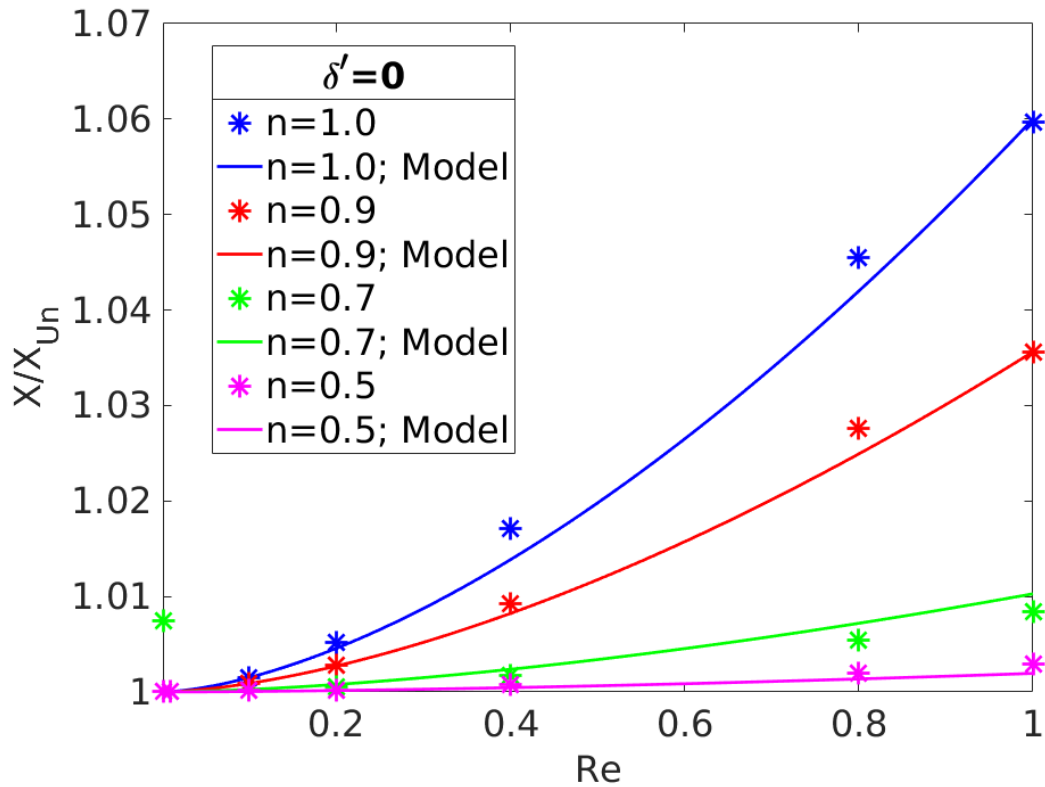


Figure 4.23: Comparison between predicted functional form in Equation 4.19 versus the numerical data for unsheared power-law fluid

$$X/X_{Un} = (1 + A' Re^B) \quad (4.19)$$

where $A' = 0.06 n^{4.947}$ and $B=1.6$

4.4.4.4 Sheared Newtonian fluids

Starting from the unsheared Newtonian fluid functional form in Equation 4.18, we extend the correlation to include the effect of imposed shear. Interestingly in Newtonian fluids, we observe there is a slight increase in the settling rate due to the changes in the pressure field, although the viscous stresses do not affect the settling. In order to accommodate this effect, we modify Equation 4.19 to a functional form, $(1 + A' Re^B)(1 + Re\delta')^b$. We modify in such a way that it retains the unsheared functional form for power-law fluids, that is, $(1 + A' Re^B)$ and accommodates the change in C_D in sheared Newtonian fluids. Initially, the term that was intended to include the effect of C_D for imposed shear was $((1 + \delta')^b$. From the data analysis, it was found that the behaviour $(1 + A' Re^B)((1 + \delta')^b$ changed for a given Re . So, it was modified to $(1 + A' Re^B)(1 + Re\delta')^b$ for better accuracy. The modified functional form is given in Equation 4.20, and its accuracy is close to 98 % with our data.

$$X/X_{Un} = (1 + A' Re^B)(1 + Re\delta')^b \quad (4.20)$$

where $b = 0.05$ and the values of A' and B remain the same as mentioned in Equation 4.19, that is $A' = 0.06 n^{4.947}$ and $B=1.6$.

$$C_{D_{Neut}} = \frac{24}{Re} X \quad (4.21)$$

where the expression for X is given in the Equation 4.20.

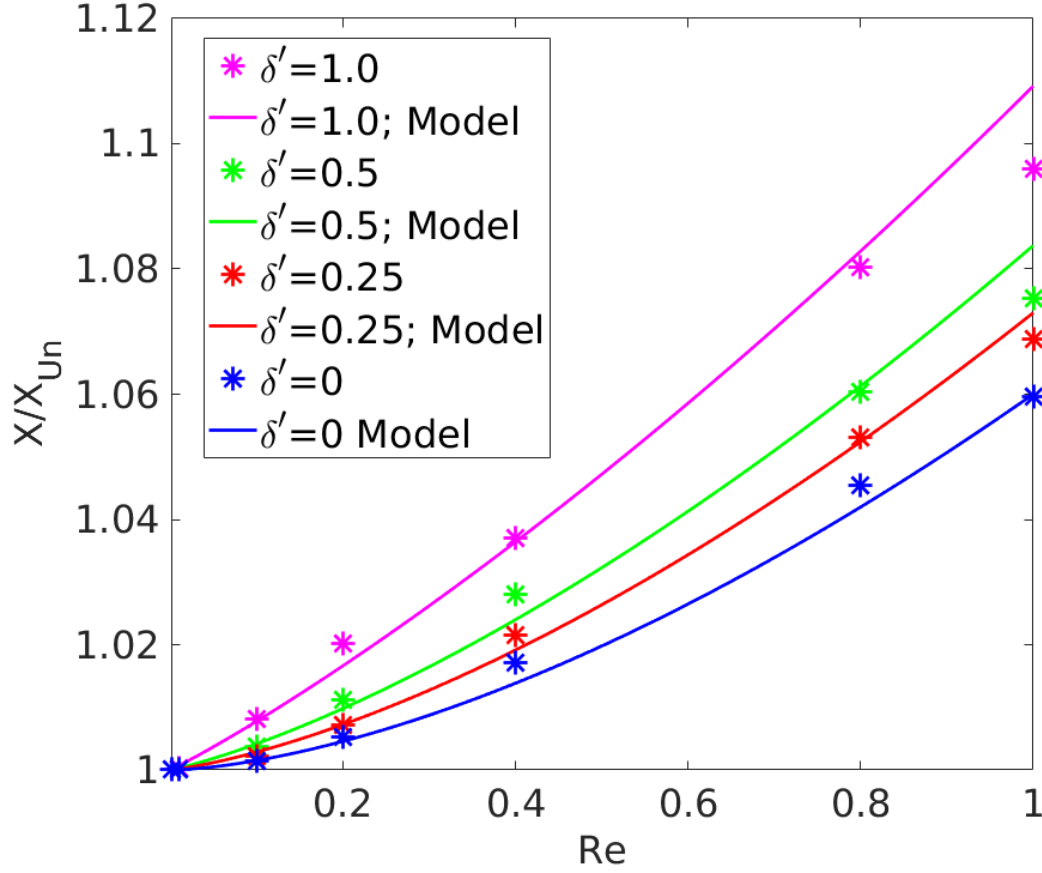


Figure 4.24: Comparison between predicted the functional form in Equation 4.20 versus the numerical data for sheared and unsheared Newtonian fluid

4.4.4.5 Sheared Power-law fluids

We now examine the manner in which imposed shear affects particle settling in power-law fluids. A prediction functional form for this is proposed by retaining the sheared Newtonian functional form (Equation 4.20) and including another multiplier - total shear rate scale $(1 + \beta\delta')^{((n-1)/2)}$. This additional term arises from the total shear rate that is experienced by the particle. Because the particle experiences shear that is induced by imposed shear $(2W/D)$, and the shear resulting from the settling of the particle (V_{Sh}/d) , the total shear rate can be written as the vectorial sum of both (Gheissary and van den Brule (1996)). The total shear can be written as Equation 4.22, which inturn modifies to Equation 4.23 when δ' is introduced.

$$\dot{\gamma}_T = \sqrt{(V_{Sh}/d)^2 + (2W/D)^2} \quad (4.22)$$

$$\dot{\gamma}_T = \frac{V_{Sh}}{d} \sqrt{1 + \delta'^2} \quad (4.23)$$

$$Re = \frac{\rho_f d V_{Sh}}{\eta} \quad (4.24)$$

Using the total shear rate in the power-law viscosity function (η), that is, $\eta = k\dot{\gamma}_T^{n-1}$, Re modifies to $Re_U / \sqrt{1 + \delta'^2}^{n-1}$. The total shear rate scale is incorporated to the prediction functional form. Empirical constant, β , was introduced to the dimensionless imposed shear to address the effect of imposed shear for sheared power-law fluids. The final functional form for sheared power-law fluids is given by Equation 4.25. The first two terms in the Equation 4.25 are the same as the functional form of unsheared power-law fluids and sheared Newtonian results. This was kept same so that the results for $\delta' = 0$ or $n = 1$ can be recovered.

$$X/X_{Un} = (1 + A'Re^B)(1 + Re\delta')^b(1 + \beta\delta')^{((n-1)/2)} \quad (4.25)$$

In the process of identifying constant values of β for each n by using non-linear regression, we obtain β , which is tabulated in Table 4.4. In the Table 4.4, for Newtonian fluids ($n = 1$), β disappears, as the power of the third term, $((n - 1)/2)$ becomes zero when $n = 1$. Therefore, the final prediction functional form that incorporates all the four conditions (unsheared Newtonian, sheared Newtonian, unsheared and sheared power-law fluids) is given by Equation 4.26. To demonstrate the accuracy of the functional form in Equation 4.26, we present the graphical representation of the numerical data, and the functional form in Figure 4.25, 4.26, and 4.27. From the Figures 4.25- 4.27, we notice that as n becomes smaller, Re makes less difference.

$$C_D = \frac{24}{Re} X_{Un} (1 + A'Re^B)(1 + Re\delta')^b(1 + \beta\delta')^{((n-1)/2)} \quad (4.26)$$

Table 4.4: Fitting parameter β from the final functional form(Eqn 4.26 for varying flow index n)

n	β
1.0	-
0.9	17.25
0.7	10.09
0.5	7.573

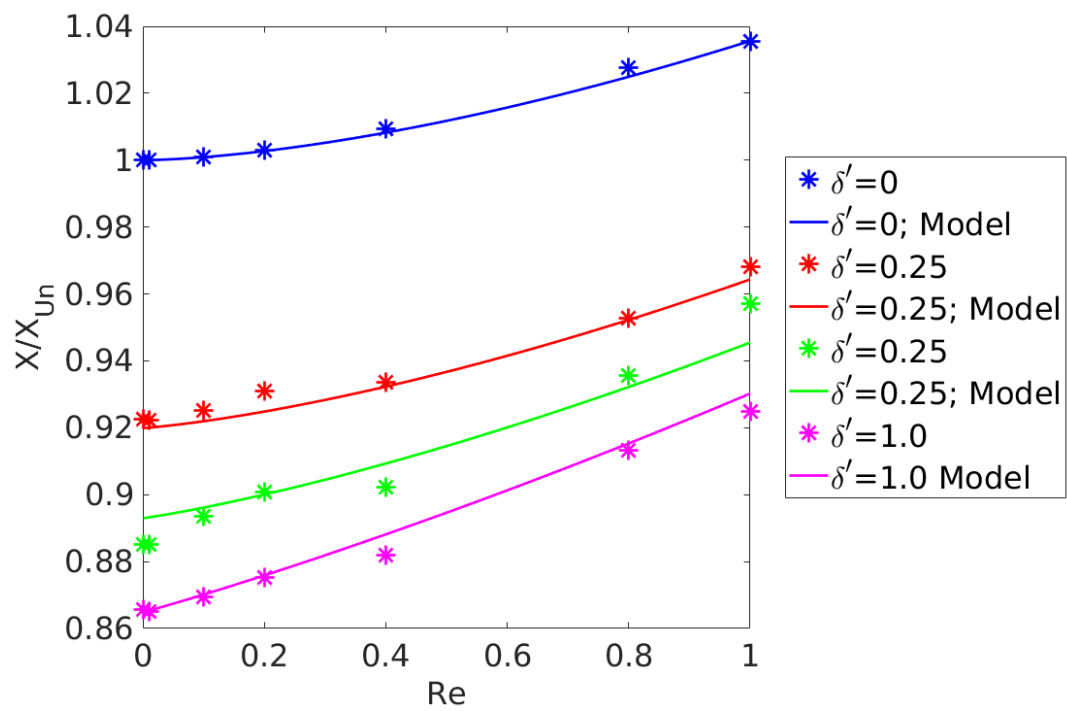


Figure 4.25: Comparison between the predicted functional form in Equation 4.25 versus the numerical data for sheared and unsheared PL fluid $n = 0.9$

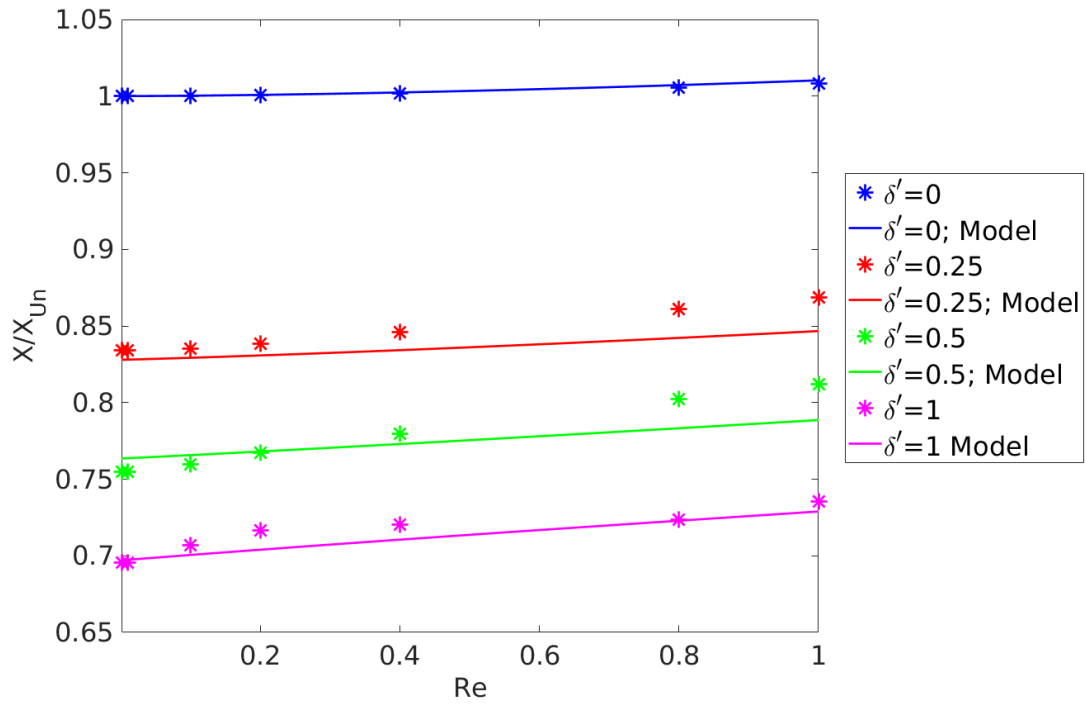


Figure 4.26: Comparison between predicted the functional form in Equation 4.25 versus the numerical data for sheared and unsheared power-law fluid $n = 0.7$

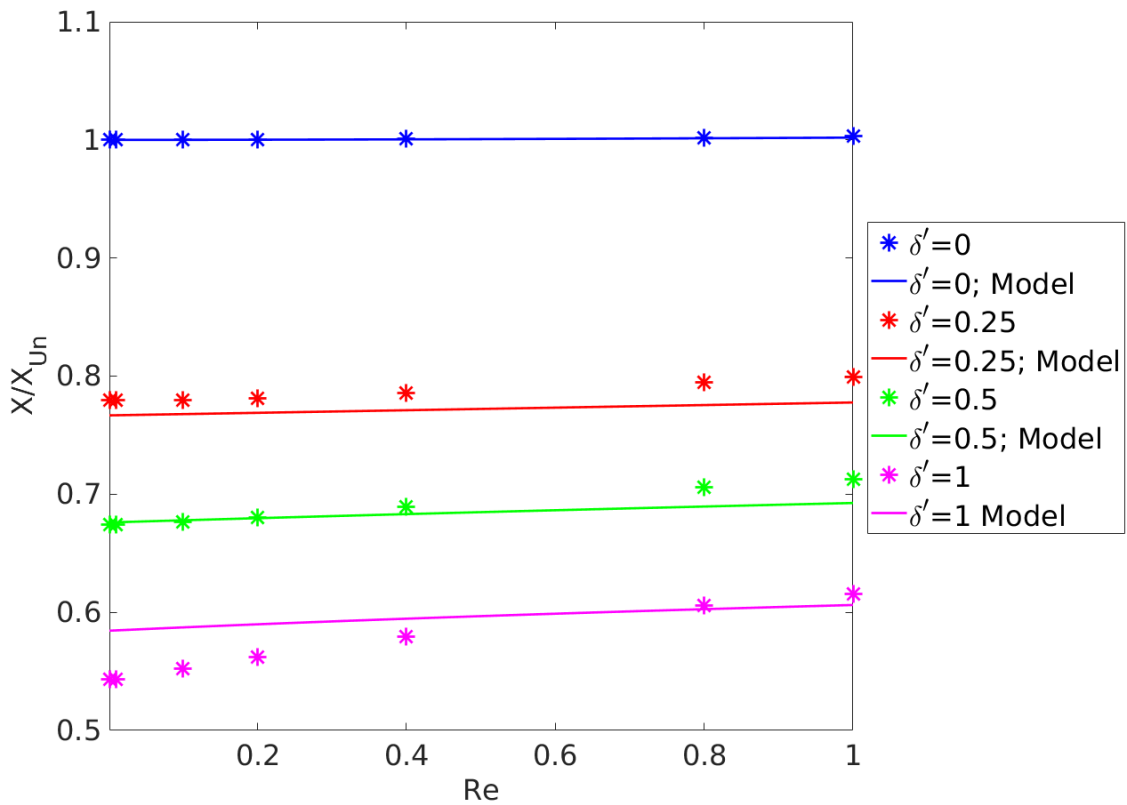


Figure 4.27: Comparison between predicted the functional form in Equation 4.25 versus the numerical data for sheared and unsheared power-law fluid $n = 0.5$

In summary, the results suggested the final equation (Equation 4.25), for the settling velocity of the spherical particle that progressively includes all the unsheared/sheared and Newtonian/power-law results, as can be seen in Figure 4.28. Finally, we compared the final Equation 4.26 and all our data, as shown in Figure 4.29. This final expression was shown to provide a good approximation of the settling velocity over a wide range of $\delta' \leq 1$ and $Re \leq 1$ with 95% accuracy.

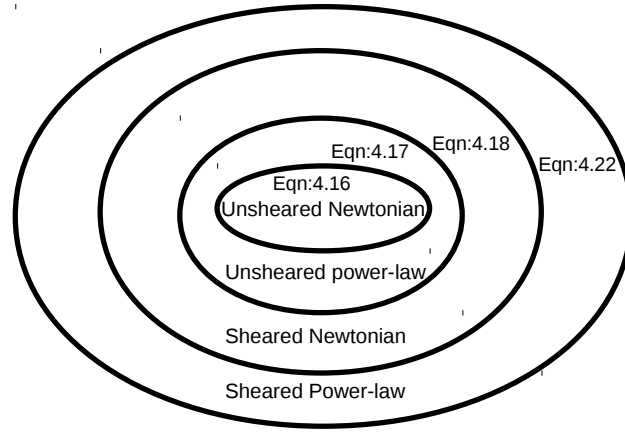


Figure 4.28: The prediction functional form for different conditions.

4.5 Pressure and viscous force

The drag force is a summation of pressure and viscous forces that act on the surface of the particle. We intend to understand the manner in which the pressure (F_p) and viscous (F_v) forces contribute due to the imposed shear. We also see how the different contributions scale differently so that we can possibly understand how to non-dimensionalise our results better. We investigate the individual forces for each case that is considered in this study. The pressure and viscous force coefficients are given by Equation 4.27 and 4.28. Since these coefficients are an inverse function of Re , we remove this effect by representing in terms of $C_p * Re$ and $C_v * Re$, and we term them Z_p and Z_v , respectively.

$$C_p = \frac{2F_p}{\rho V_{sh}^2 A} \quad (4.27)$$

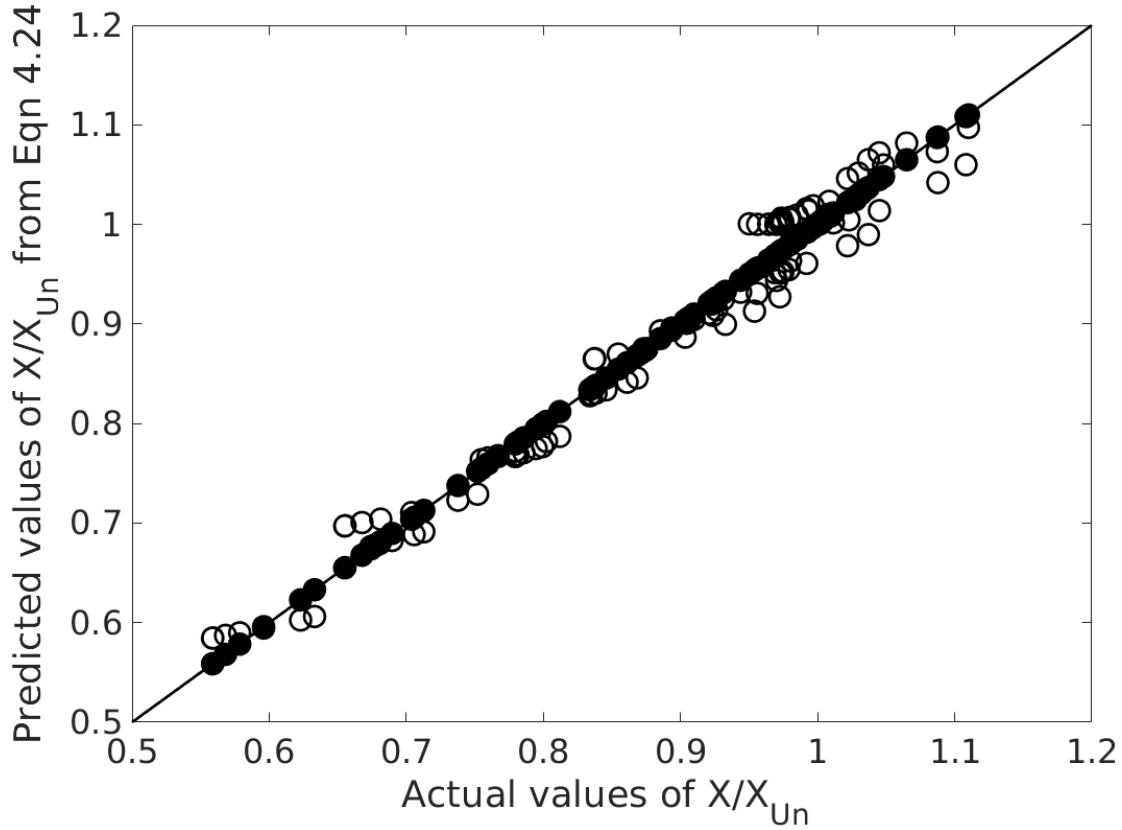


Figure 4.29: Predicted values of X/X_{Un} from Equation 4.25 versus actual values of X/X_{Un} .

$$C_v = \frac{2F_v}{\rho V_{sh}^2 A} \quad (4.28)$$

Firstly, for unsheared Newtonian fluids, the resulting magnitude for $Z_p (= C_p * Re)$ and $Z_v (= C_v * Re)$ is 6 and 18, respectively. This explains the fundamental Stokes solution, $C_D = C_p + C_v = (6 + 18)/Re = 24/Re$, which can be seen in Figure 4.30 for $n = 1$. The value of Z_p and Z_v for power-law fluids decreases in different cases such as for low n and high δ' . This difference in the values of Z_p and Z_v with respect to the flow index and the imposed shear is discussed in this section. From Figure 4.30, we observe that as the shear-thinning behaviour of the fluid increases, the pressure and viscous forces increase as well. For example, in $n = 0.7$, for small Re , $Z_p \approx 12$ and $Z_v \approx 20$, as can be seen in Figure 4.30. Although attempts were made to bring out the expressions separately for pressure and viscous in the sheared case, since both increase with increase in imposed shear, their sum-total drag was found sufficient.

In a sheared Newtonian fluid, Z_p and Z_v decrease very marginally as δ' increases, up to an Re of less than approximately 0.1; they then gradually increase with δ' as Re

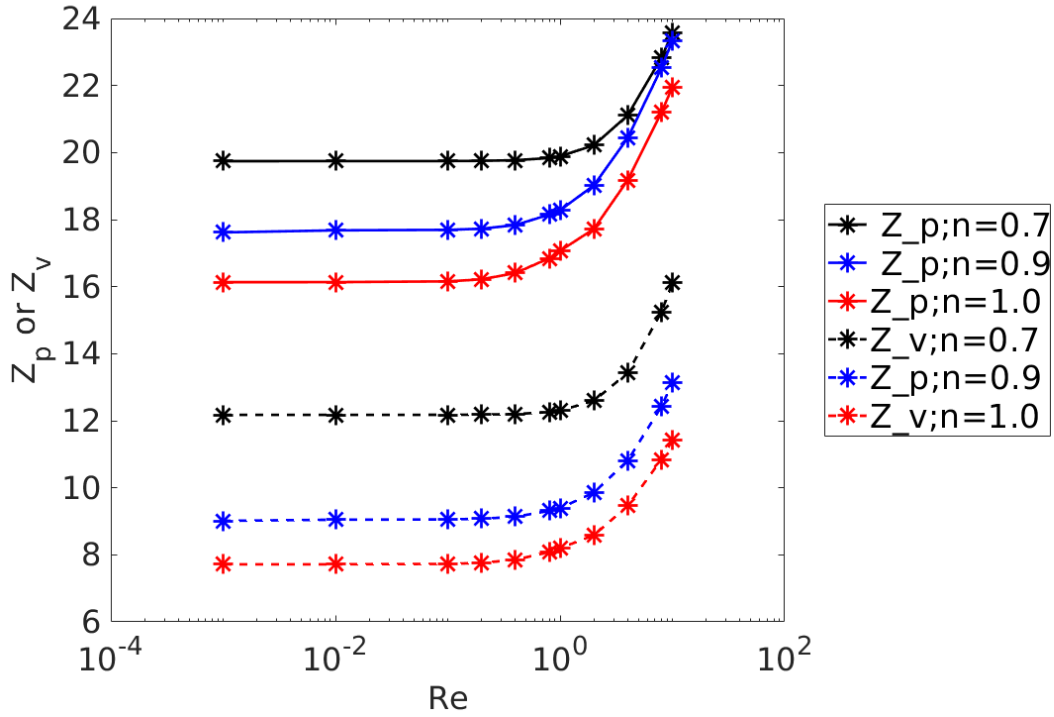


Figure 4.30: Z_p and Z_v values for $0.7 < n < 1$ under unsheared conditions

increases, as can be seen in Figure 4.31. Two things can be observed in this case (see Figure 4.31). Initially, when the Re is low ($Re < 0.1$), the coefficients (Z_p and Z_v) decrease leading to faster settling than that in the unsheared case. When Re is greater than 0.1, the trend of the coefficients reverses due to the changes in the pressure field at higher δ' , which causes a higher drag on the particle.

Lastly, in sheared power-law fluids ($n < 1$), we notice in Figure 4.31, that Z_p and Z_v decrease with δ' for all Re unlike a sheared Newtonian fluid. This is because the applied shear impacts the total shear rate, allowing it to settle consistently for very low Re , and then rapidly for higher Re .

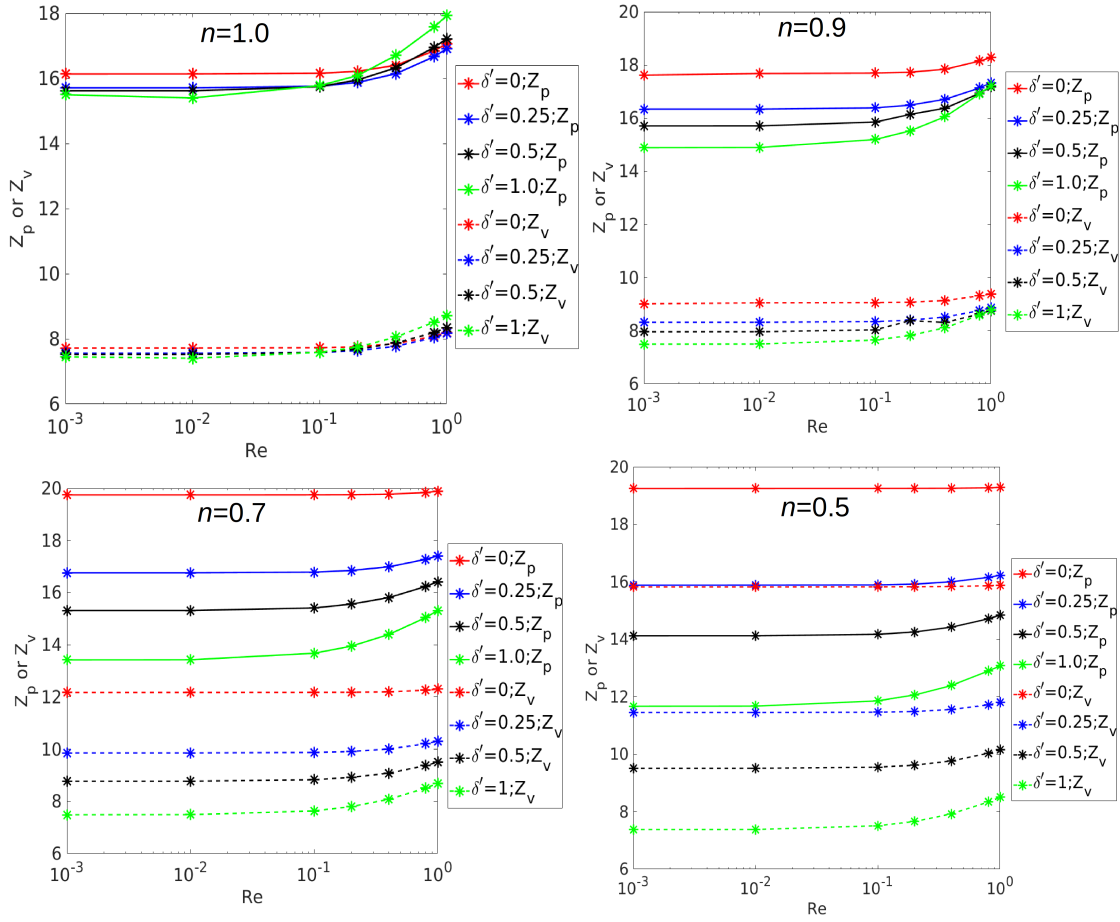


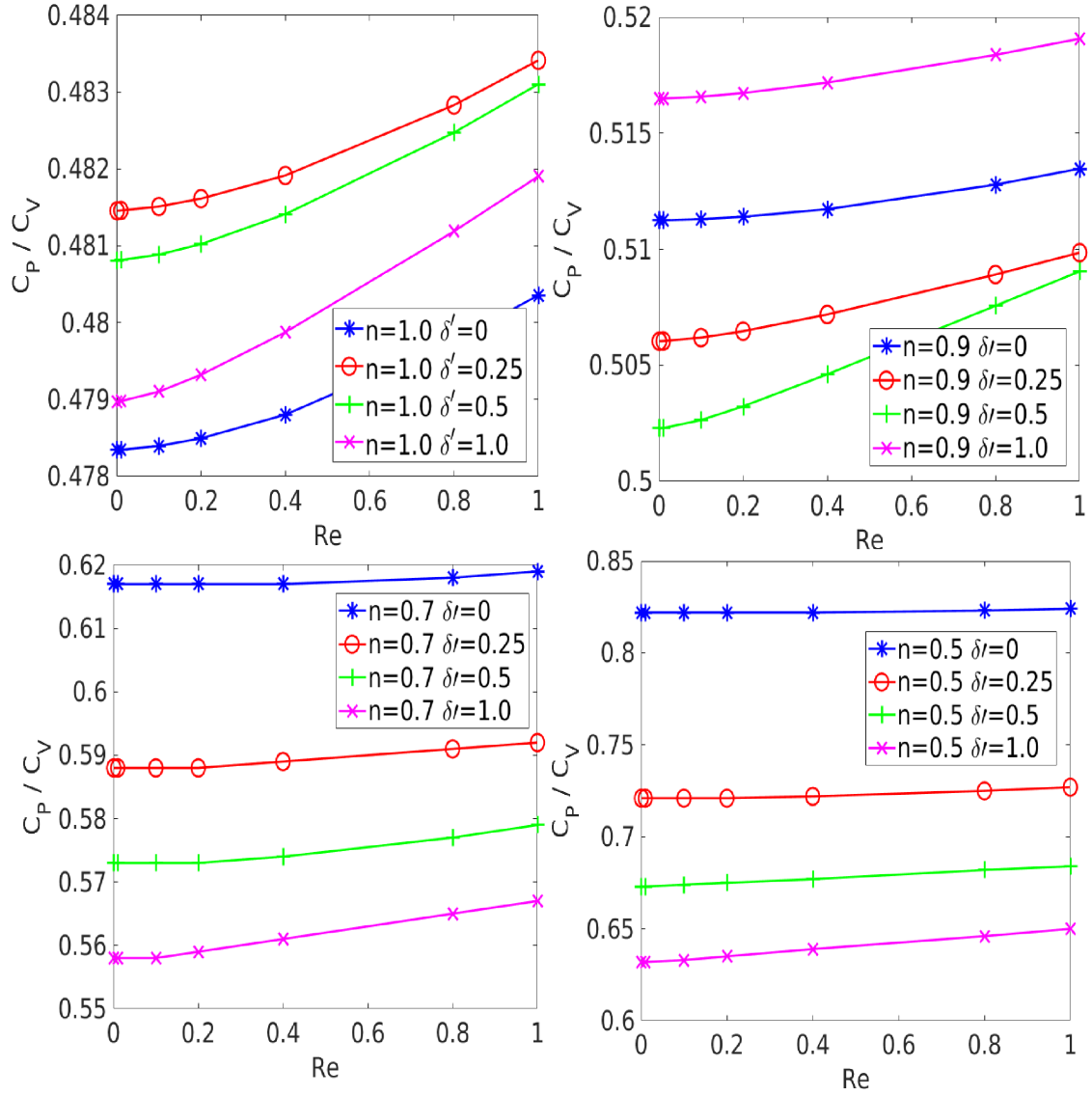
Figure 4.31: Z_p or Z_v values for $n = 1, 0.9, 0.7$ and 0.5 .

4.5.1 Ratio of pressure to viscous force

This section is concerned to illustrate the behavior of dimensionless parameter C_p/C_v . This was intended to understand its dependency on other dimensionless parameters especially Reynolds number. The ratio C_p/C_v shows a weak dependency on Re for all flow indices, as can be seen in Figure 4.32. Additionally, it is also observed that the ratio C_p/C_v is a strong function of δ' and flow index. In the Figure 4.32, we observe that the value of C_p/C_v is higher for small n and much higher as $\delta' \rightarrow 0$.

4.6 Relationship between applied shear rate and ω

A spherical particle in an unbounded inertia-less Newtonian liquid that is subjected to a shear flow was addressed by Einstein (1906, 1911). Particle rotation is predicted due to the shear flow with the rotational speed, ω , dependent on the applied shear rate $\dot{\gamma}$.

Figure 4.32: C_p/C_v values for $n = 1, 0.9, 0.7$ and 0.5 .

The particle rotation rate for the Stokes Newtonian fluid is half the imposed shear rate. However, at higher Reynolds numbers and in non-Newtonian fluids, the value of ω is unknown.

When we examine the particle rotation rate based on the imposed shear rate, ω predicted from simulations for shear imposed settling is found to be approximately equal to half the applied shear rate ($\dot{\gamma}_{imposed}$) for all n and Re that are covered in this study, as shown in Figure 4.33.

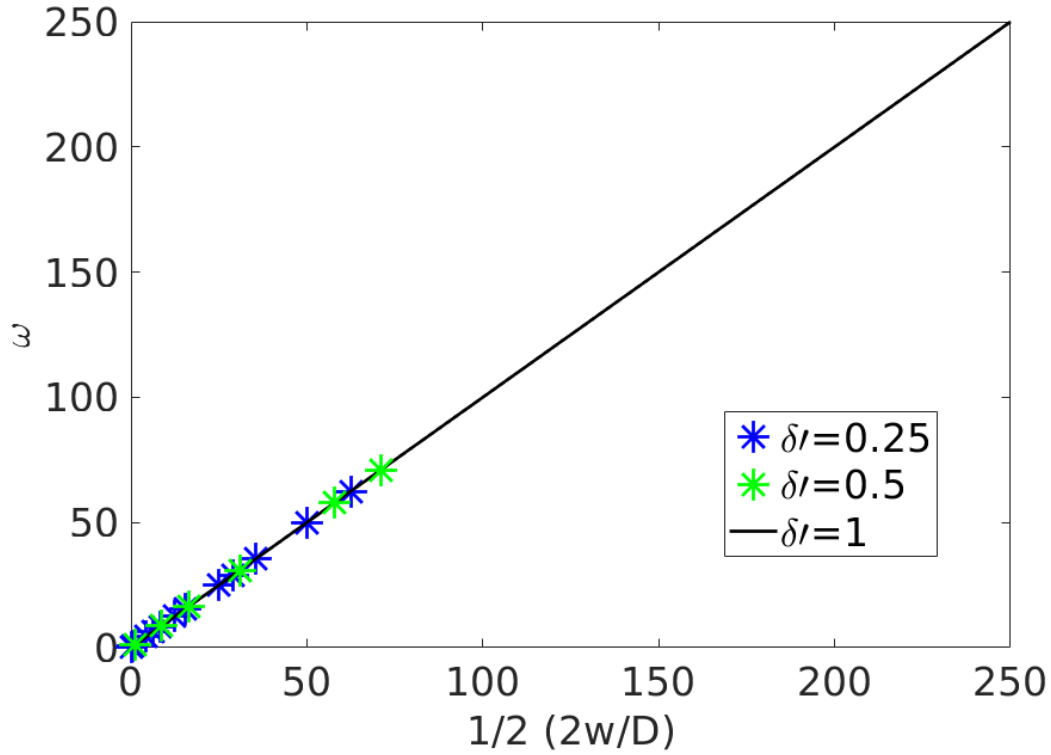


Figure 4.33: Comparison between ω and $1/2(2W/D)$ -half the imposed shear for $0.001 \leq Re \leq 1$ and $0.5 \leq n \leq 1.0$

4.7 Comparison of results in terms of δ and δ'

In our study, the applied shear was scaled was non-dimensionalised in two different ways and a comparison between their prediction was intended. In order to compare the results in terms of δ and δ' , we convert the non-dimensional equation, Equation 4.26 in terms of V_{Sh} . We obtain an implicit expression for settling rate, V_{Sh} , from the C_D , Re , and δ' correlation described in the Eqn 4.26 using a solve function in matlab. The approach to obtain an implicit expression for V_{Sh} is discussed in §A.1. The resulting expression is given in Equation A.9.

For $500 \leq \Delta\rho \leq 4000$, $0.5 \leq n \leq 1.0$, and $k=0.1$ and 2 , the value of V_{Sh} was obtained using the two equations (Eqns A.9 and 4.13) and compared to observe the manner in which they relate. A maximum of 5.32% difference was found between the two equations, as shown in Figure 4.34.

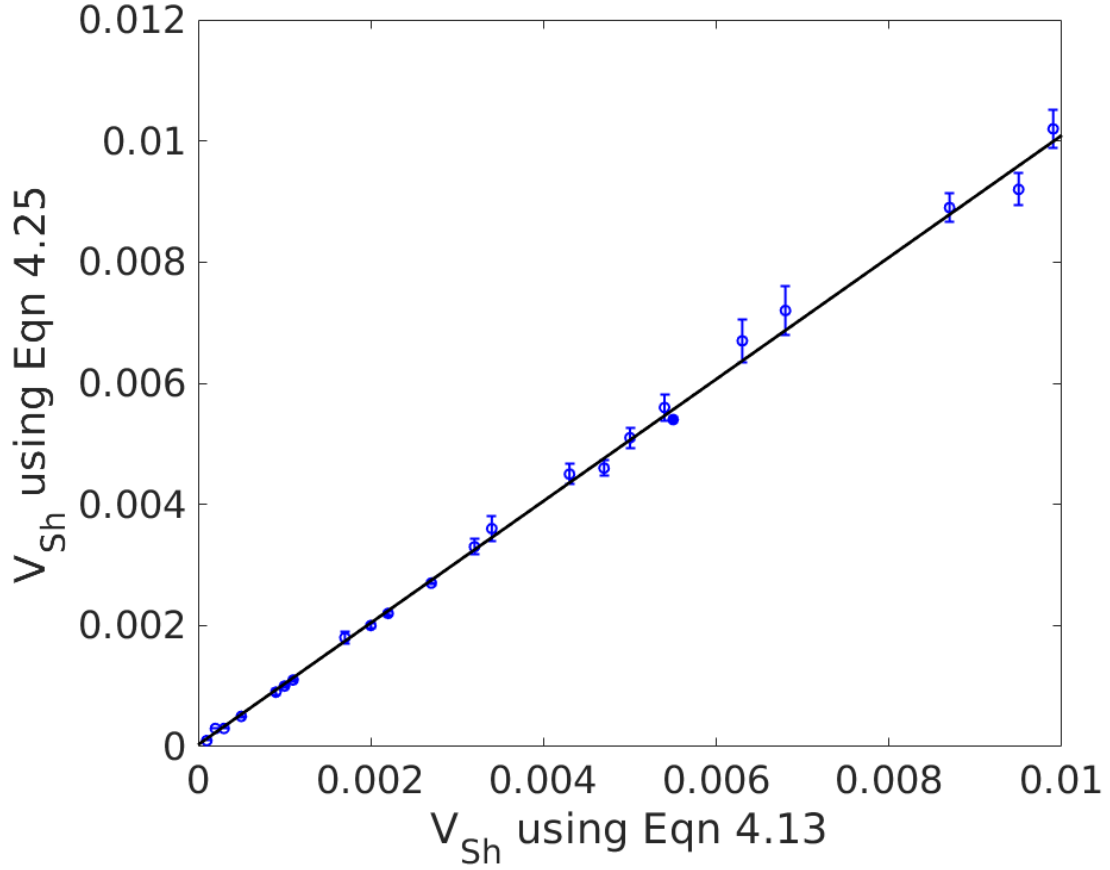


Figure 4.34: Comparison between the prediction in terms of δ (Eqn 4.13) and δ' (Eqn4.26)

4.8 Summary

A detailed investigation of particle settling in unsheared and sheared power-law fluids has been discussed, and it was found that imposed shear plays a significant role in particle settling. Computational predictions by the model for unsheared settling were found to be in good agreement with past studies. For sheared conditions, a stringent comparison between the experimental measurements by CSIRO and our numerical results has been made using the same fluid rheology, and it was found to be in excellent concordance with the measurements. Similarly, a comparison with the analytical solution that is available for non-inertial flow by Childs (2013) was found to produce consistently good results.

Prior to quantifying the settling rate, the flow field is analysed to show the manner in which the imposed shear affects the velocity field. A point wise differencing between the different flow fields of different cases provided an insight into the effect of Re and the imposed shear. With the imposed shear, the particle rotates with a rotational speed that is almost half of that of the imposed shear rate ($=2W/D$) for all n , Re , and δ' .

The validated computational model was then used to investigate a range of n and Re . For unsheared settling in the $Re < 1$ flow regime, the settling velocity data that was obtained was used to provide a prediction based on the Newtonian Stokes flow formulation, as described in Equation 4.11.

An expression for predicting the settling rate in terms of the unsheared settling rate for a given $\Delta\rho$ has been presented for a range of imposed shear δ . In sheared settling, it was observed that the ratio of the settling velocity to the unsheared settling velocity is a strong function of δ and n . It was found that the ratio was a weak function of Re . Therefore, the predicted ratio of V_{sh}/V_U for a range of δ and n was provided in the condensed form presented in Equation 4.13.

The approach to represent drag coefficients in terms of drag correction factor, ' X/X_{Un} ', was obtained from Dazhi and Tanner (1985); the original was subsequently modified to account for imposed shear δ' . The final functional form in Equation 4.26 includes all the different factors that were considered in this study and provides an accurate prediction of settling for $Re \leq 1, 0.5 \leq n \leq 1.0$ and $0 \leq \delta' \leq 1.0$.

This result has implications in the settling time and, importantly, in the settling distance that is required for the stratification of a homogeneous coarse particle suspension. This study will be further extended in the next Chapter to consider the effect of shear rates on the yield-stress fluids.

Chapter 5

Settling in Herschel–Bulkley fluids

Unlike previous studies, there has been little work on yield-stress fluids at high shear rates, and it remains to be fully characterised and understood. The focus of this chapter is the the impact of shear on particle settling in yield stress fluids that can be modeled by the Herschel–Bulkley model. Similar to the previous chapter, the scaling of the governing equations that lead to the dimensionless groups, based on which, results are presented. Firstly, the unsheared settling is discussed in three parts: (i) the condition for settling, (ii) flow visualisation and (iii) settling predictions. Secondly, the sheared settling is discussed in three parts: (i) dimensionless parameters due to the applied shear, (ii) description on the aspects of the flow field and (iii) settling predictions by our computational model. Therefore, in the imposed shear, the manner in which the shear affects the viscous stress in fluids that have a low to high yield stress is examined and discussed in detail in this chapter.

Here, it is shown that the applied shear affects the particle in such a way that it allows to move through the fluid; this is relevant because; the particle, typically, does not move in certain cases. Therefore, determining a critical particle size under sheared conditions is not important. An expression for the prediction of settling velocity for unsheared settling was established using dimensionless numbers that accounts for the yield-stress property of the fluid. Additionally, based on the computational measurements, the expression for sheared settling is developed as a function of the flow index, imposed shear and the dimensionless numbers.

5.1 Domain independence study

Although domain independence has been discussed previously for Newtonian and power-law fluids, it was revisited here for Herschel–Bulkley fluids to ensure the same result was applicable. Therefore, a domain independence study using Herschel–Bulkley model was performed to ensure that result is independent of domain size. A similar grid resolution that was previously used for power-law fluids was considered for the domain independence study.

Firstly, for unsheared particle settling, a known finding from the literature (Tabuteau *et al.* (2007a)) is used to conduct this study. Tabuteau *et al.* (2007a) proposed to express the drag coefficients for the unsheared particle settling without the influence of the boundary walls in creeping flow regime. The difference percentage between Tabuteau *et al.* (2007a) and our numerical model was calculated. It can be seen from Figure 5.1, that the appropriate ratio of domain size (D) to particle diameter (d) is 25 or higher.

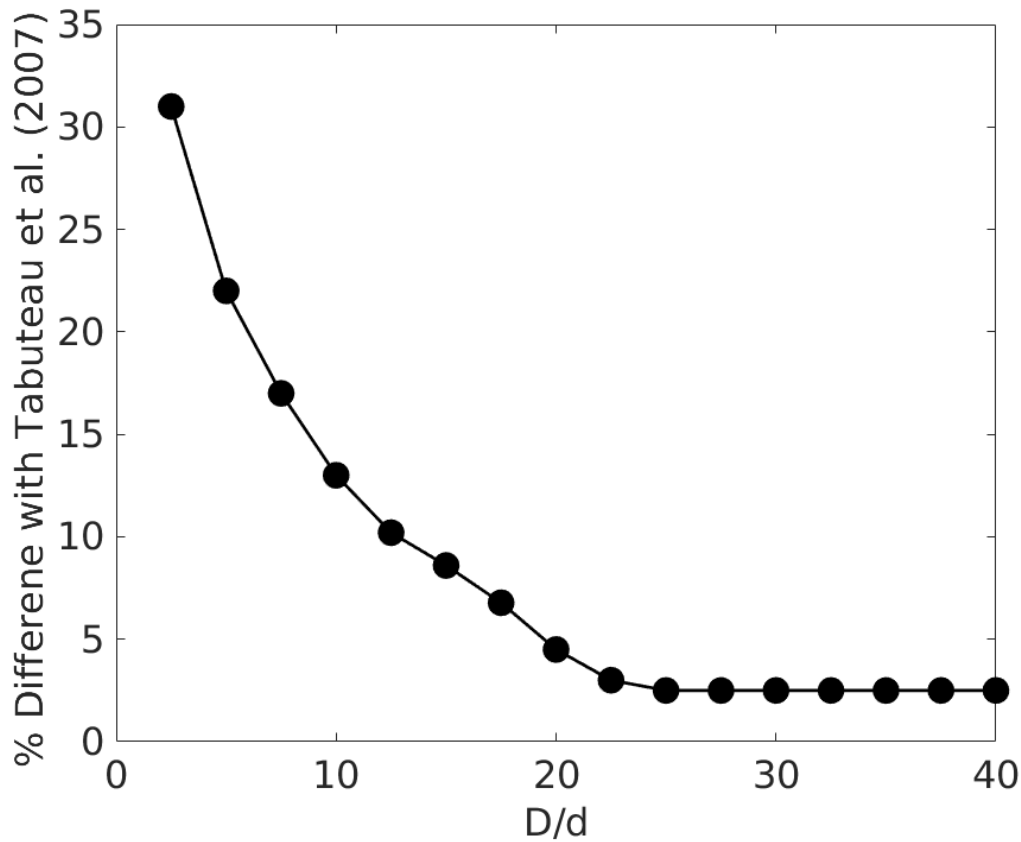


Figure 5.1: Percentage difference of drag prediction with Tabuteau *et al.* (2007a) for increasing domain size.

Secondly, for sheared settling, a set of experimental measurements by CSIRO at different imposed shear are used to conduct the domain independence study. The experimental measurements were made in a sufficiently large container to ensure the influence of the container was absent. For the fluid rheology, $\tau_y = 8.133$; $k = 3.78$; $n = 0.373$, and imposed shear of 16.5 s^{-1} , the drag difference between the experimental measurement and our model is given in Figure 5.2. Therefore, we ascertain from the domain independence study that the appropriate domain to particle size ratio could be 30 or higher. Other grid resolution parameters were the same as those from the previous setup that was used in sheared power-law settling computation. Although Atapattu *et al.* (1995b) found that the settling velocity to be constant when $D/d \geq 15$ within a 10% deviation with the large D/d , in our computational study we consider $D/d = 30$ in order to further reduce the deviation upto 1.2%.

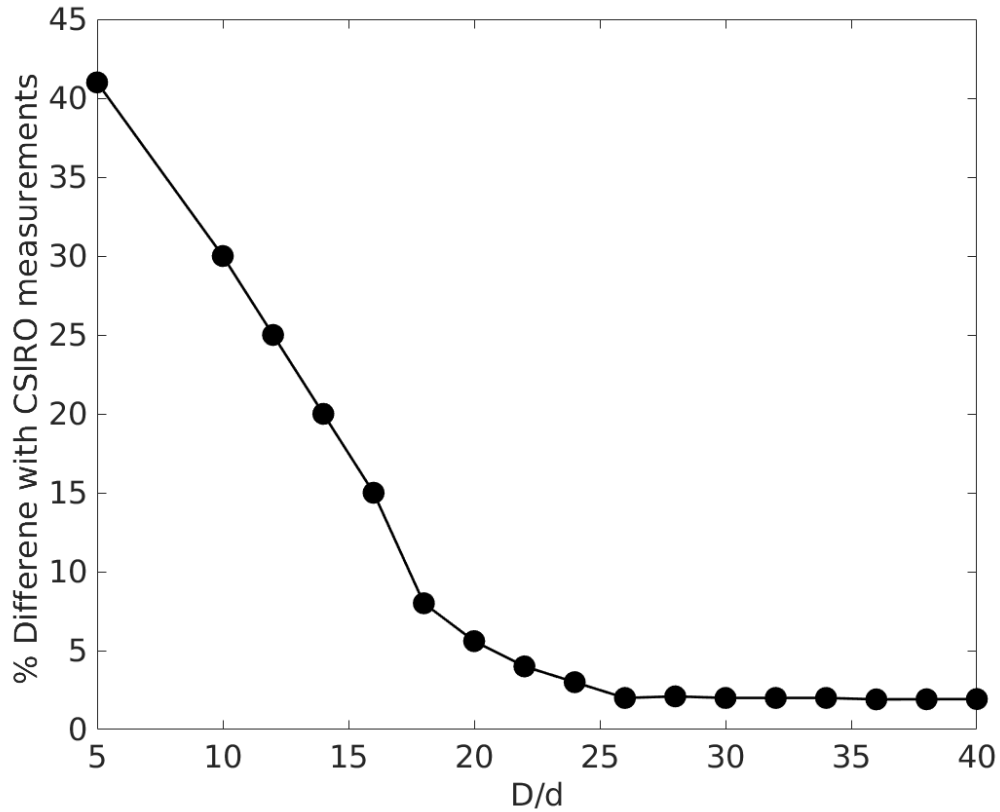


Figure 5.2: Drag prediction for increasing domain size for yield-stress fluid $\tau_y = 8.133$; $k = 3.78$; $n = 0.373$ for imposed shear rate of 16.5 s^{-1}

5.2 Critical particle size

When a particle sits in a quiescent yield stress fluid, if the stress resulting from is less than the fluid's yield stress, then the fluid's deformation rate will be zero and the particle remains stationary. In such cases, the particle is found to be embedded to the fluid and will remain suspended indefinitely. The likely conditions for this phenomenon to occur are low particle size, weight, and high yield stress. Therefore, a critical particle size for particle to settle in a yield stress fluid is investigated.

Previously, the critical particle size for settling was investigated by Dedegil (1987) through analytical methods and Atapattu *et al.* (1995b), Jossic and Magnin (2009), and Tabuteau *et al.* (2007a) through experimental approaches. Yield-stress effects were studied in association with varying particle weights/sizes and fluid density. On the basis of these results, a stability criterion is proposed by Dedegil (1987), as shown in Equation 5.1 and by Atapattu *et al.* (1995b), as given in Equation 5.2.

1. Dedegil (1987) proposed an analytical expression for critical particle size.

$$d_{crit} = \frac{3\pi}{2} \frac{\tau_y}{\Delta\rho g} \quad (5.1)$$

2. Atapattu *et al.* (1995b) proposed another expression for critical particle size through experimental data.

$$d_{crit} = \frac{21}{\Delta\rho g} \tau_y \quad (5.2)$$

The former criterion is five times smaller than the latter. An investigation was carried to determine which criterion the results here most closely follow. To determine the critical particle size for settling, we examine the drag force that is exerted on the particle in a yield stress fluid when the velocities become infinitesimally slow. For a given rheology, the drag was plotted as a function of settling velocity. It has been found that the drag asymptotes to a certain value as the limit $V_s \rightarrow 0$, as can be seen in Figure 5.3 and 5.4. We hypothesise that the drag for infinitesimally slow particle asymptotes to a constant and when this asymptotes, then the critical particle density will be given by buoyancy balance. That is, as the value of drag for the limit as $V_s \rightarrow 0$ exists and is non-zero, we believe this force when balanced with buoyancy will provide the value of $\Delta\rho$ at which the particle will be just suspended. Therefore, from the asymptotic value of the drag, we are

able to identify the critical density difference. A sample calculation for determining $\Delta\rho$ that proves that our model predicts close to the Equation 5.2, is demonstrated in §A.4. Although the works by Dedegil (1987) and Atapattu *et al.* (1995b) are in terms of d_{crit} , we interpret the same criterion but the particle size is considered constant here and $\Delta\rho$ as the varying entity, as shown in Equation 5.3. Therefore, it has been found from our study that, our model predicts close to the stability criterion proposed by Atapattu *et al.* (1995b). Furthermore, Beris *et al.* (1985) and Blackery and Mitsoulis (1997) agreed with Atapattu *et al.* (1995b) through their numerical simulations. This agreement has been proved with the help of examples of two fluid rheologies in section below (§5.2.1).

$$\Delta\rho_{critical} = \frac{21 \tau_y}{dg} \quad (5.3)$$

5.2.1 Calculation of asymptotic force

Normal and tangential forces act opposite to the weight. It is known that the integral that takes over the surface of the normal force due to hydrostatic pressure leads to the buoyant force, which is independent of the particle shape. As mentioned before, we consider the value of drag obtained for the limit as $V_s \rightarrow 0$ and balanced by its buoyancy to obtain the critical density difference. Additionally, in this case, we assume that the wall of the container has no effect on particle settling; that is, we consider the domain size to be unbounded (since we use the domain to particle size ratio D/d equal to 30).

Richardson extrapolation was used to ascertain the value of the drag force of an infinitely slow-moving particle ($V_U \rightarrow 0$) in yield stress fluid. A python algorithm for Richardson extrapolation was used to achieve this, and its output was F_D at $V_U = 0$.

After equating the extrapolated value of drag for $V_U = 0$ with the buoyancy force, we obtain the corresponding $\Delta\rho$. This was the critical $\Delta\rho$ for the particle size and fluid rheology that was considered in the numerical study.

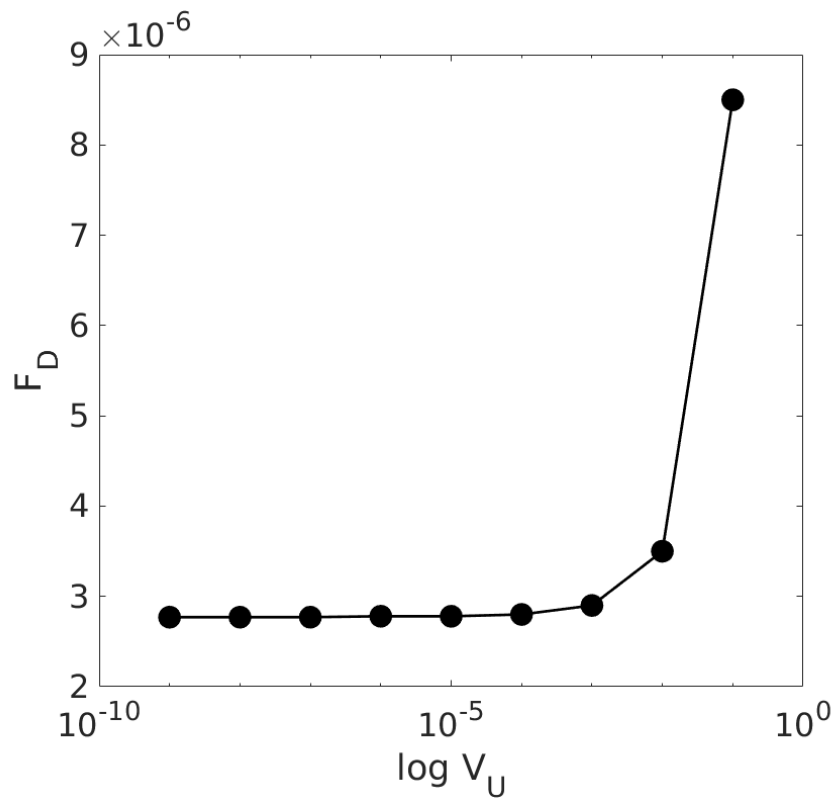


Figure 5.3: Drag force asymptotes as the settling rate decreases for one mm particle for the fluid rheology, $\tau_y = 0.1$ $k = 0.1$ $n = 0.3$

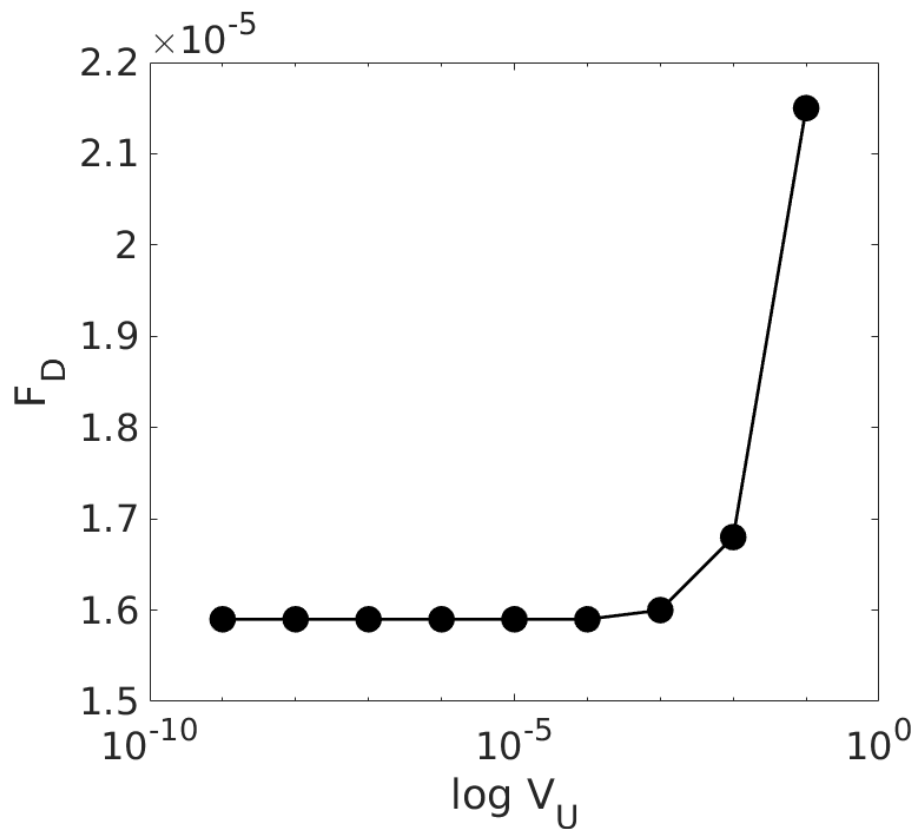


Figure 5.4: Drag force asymptotes as the settling rate decreases for one mm particle for the fluid rheology, $\tau_y = 1$ $k = 0.1$ $n = 0.3$

For the fluid rheologies, $\tau_y = 0.1$ $k = 0.1$ $n = 0.3$ and $\tau_y = 1$ $k = 0.1$ $n = 0.3$, the value of the drag force of an infinitely slow-moving particle ($V_U \rightarrow 0$) is $2.77e^{-6}$ and $1.6e^{-5}$, respectively, as can be seen in Figure 5.3 and 5.4. From our investigation into the determining of the critical density difference ($\Delta\rho_{critical}$) for settling in yield-stress fluids, we have found that our results match well with Equation 5.2, and the numerical tolerance is within 3 % of difference. Therefore, to represent this criterion in terms of the dimensionless parameter, we observe that the Yield-gravity number ‘Y’ (defined as shown in Equation 5.4) should be not greater than $\frac{1}{21}$. Above this yield parameter there is no motion of the particle in the fluid.

$$Y = \frac{\tau_y}{\Delta\rho g d} \quad (5.4)$$

5.3 Definition of Reynolds number

In the process of investigating yield stress fluids, there are two ways of defining Re, one without including the yield stress, which is same as the power-law Re and the other with the inclusion of yield stress.

The definition of Re with the inclusion of yield stress incorporates the Herschel–Bulkley number (HB, defined as shown in Equation 5.5). To define Re including the yield stress, Herschel–Bulkley viscosity model (Eqn 5.6) is used in place of η_{sh} in the definition of Re. Additionally, the total shear rate scale ($\dot{\gamma}_T$) for sheared settling is given by Eqn 5.7, where $\delta' = \frac{2W/D}{V_{sh}/d}$.

$$HB = \frac{\tau_y}{k\dot{\gamma}_T^n} \quad (5.5)$$

$$\begin{aligned} \eta_{sh} &= \frac{\tau_y}{\dot{\gamma}_T} + k\dot{\gamma}_T^{(n-1)} \\ &= k\dot{\gamma}_T^{(n-1)}\left(\frac{\tau_y}{\dot{\gamma}_T} + 1\right) \\ &= k\dot{\gamma}_T^{(n-1)}(HB + 1) \end{aligned} \quad (5.6)$$

$$\dot{\gamma}_T = \frac{V_{Sh}}{d} \sqrt{1 + \delta'^2} \quad (5.7)$$

When η_{Sh} (Eqn 5.6) and $\dot{\gamma}_T$ (Eqn 5.7) is used in the definition of Re , we get Equation 5.8. It can be seen that the resulting Reynolds number (Re_{HB}) is equal to the product of power-law Re and $1/(HB + 1)$. Since, the definition of Re including yielding yield stress (Re_{HB}) incorporates HB explicitly and to be consistent with our power-law results, we intend to use the power-use Re in our investigation. However, the term $1/(HB + 1)$ is included in the correlation that used for the prediction, which is discussed in the later section of the chapter. Certain previous works (Atapattu *et al.* (1995a), Patel and Chhabra (2013), Beaulne and Mitsoulis (1997), Gavrilov *et al.* (2017), Burgos and Alexandrou (1999), and Ahonguio *et al.* (2014)) on the Herschel–Bulkley fluid have also used power-law definition for Reynolds number, that is, without the inclusion of yield stress.

$$\begin{aligned} Re_{HB} &= \frac{dV_{Sh}\rho_f}{\eta_{Sh}} \\ &= \frac{dV_{Sh}\rho_f}{k\dot{\gamma}_T^{(n-1)}(HB + 1)} \\ &= \frac{dV_{Sh}\rho_f}{k\frac{V_{Sh}^{n-1}}{d^{n-1}}(\sqrt{1 + \delta'^2})^{n-1}(HB + 1)} \\ &= \frac{d^n\rho_f V_{Sh}^{2-n}}{k(1 + \delta'^2)^{(n-1)/2}(HB + 1)} \\ &= \frac{Re}{(HB + 1)} \end{aligned} \quad (5.8)$$

OpenFOAM requires dimensional inputs, so for a given simulation, in order to fix Re and HB , one has to set the dimensional parameters and work it backwards. In this case, the dimensional parameters have to be ensured in such a way that they fall under the rheology parameter space as discussed in the Section §2.2.1.1. For $0.001 \leq Re \leq 1$, $0.5 \leq n \leq 1$ and $0.1 \leq HB \leq 10$, we obtain the simulated drag and represent our data as shown in Equation 5.9. When the simulated drag is scaled with Stokes drag coefficient, $24/Re$, we obtain the scale factor for drag, X , as shown in Equation 5.10.

$$\begin{aligned}
C_D &= f(Re, n, \delta', HB) \\
&= C_{DStokes} X_{Un} * f(Re, n, \delta', HB)
\end{aligned} \tag{5.9}$$

$$\frac{C_D}{C_{DStokes}} = X \tag{5.10}$$

$$X/X_{Un} = f(Re, n, \delta', HB) \tag{5.11}$$

The value of X is a function of Re, n, δ' , and HB . We represent our data in terms of X/X_{Un} , where X_{Un} is a function of n . The values of X_{Un} is given by Table 5.1 and is same as the values used for sheared power-law fluids' investigation. Therefore, to quantify the drag on a sphere in yield-stress fluids under sheared conditions, we represent our results in terms of X/X_{Un} , which is a function of imposed shear, flow index and yield stress, as can be seen in Equation 5.11.

Table 5.1: The values of the drag correction factor X_{Un}

n	X_{Un}
1	1.00
0.8	1.24
0.65	1.351
0.5	1.461

5.4 Flow field

Ultimately, the forces on a settling particle arise from the pressure and viscous forces on its surface which in turn depend on velocity and viscosity field. Therefore, an understanding of these is an essential part of the investigation of the results. In the contour plots, we demonstrate the regions of deformation of the fluid around the particle for both unsheared and sheared settling in §5.4.1 and §5.4.2, respectively.

5.4.1 Flow field under an unsheared condition

To illustrate the effect of particle settling other than in terms of drag, we demonstrate the regions of deformation of the fluid around the particle. When a particle's weight is able to overcome the yield stress, it deforms the fluid structure and settles. However, there are some regions on the fluid domain with a zero shear rate, there is no fluid motion in those regions. The solid-like zones are known as the 'unyielded region' in the fluid domain. The main objective of investigating the flow fields under an unsheared condition is to understand the manner in which the undeformed region is dependent on the properties of fluid rheology mainly in terms of the yield-stress property of the fluid (discussed in §5.4.1.1) and the flow index (discussed in §5.4.1.2).

5.4.1.1 In terms of Herschel–Bulkley number

The aspects of the unyielded region in the fluid medium was primarily addressed by Atapattu *et al.* (1995a) through experiments. It was found that the size of the unyielded region increases as the yield stress of the fluid increases. Putz *et al.* (2008) conducted a computational study to understand this behaviour by using polymeric shear-thinning - yield-stress fluids to prove the same. A kidney bean like structure on the sides of the surface of the particle is referred as the unyielded region. The unyielded region appears symmetrical to both the sides around the particle in the fluid domain and its size increases as HB increases, as can be seen in Figure 5.5.

5.4.1.2 In terms of flow index

For a given HB, we examine the effect of flow index on the size of the unyielded region. We observe that for a given HB (here HB=10), the size of the unyielded region decreases as n decreases, as can be seen in Figure 5.6. This is because, when the unyielded region increases, it proves that the viscous deformation that is induced in the flow diminishes at a high n .

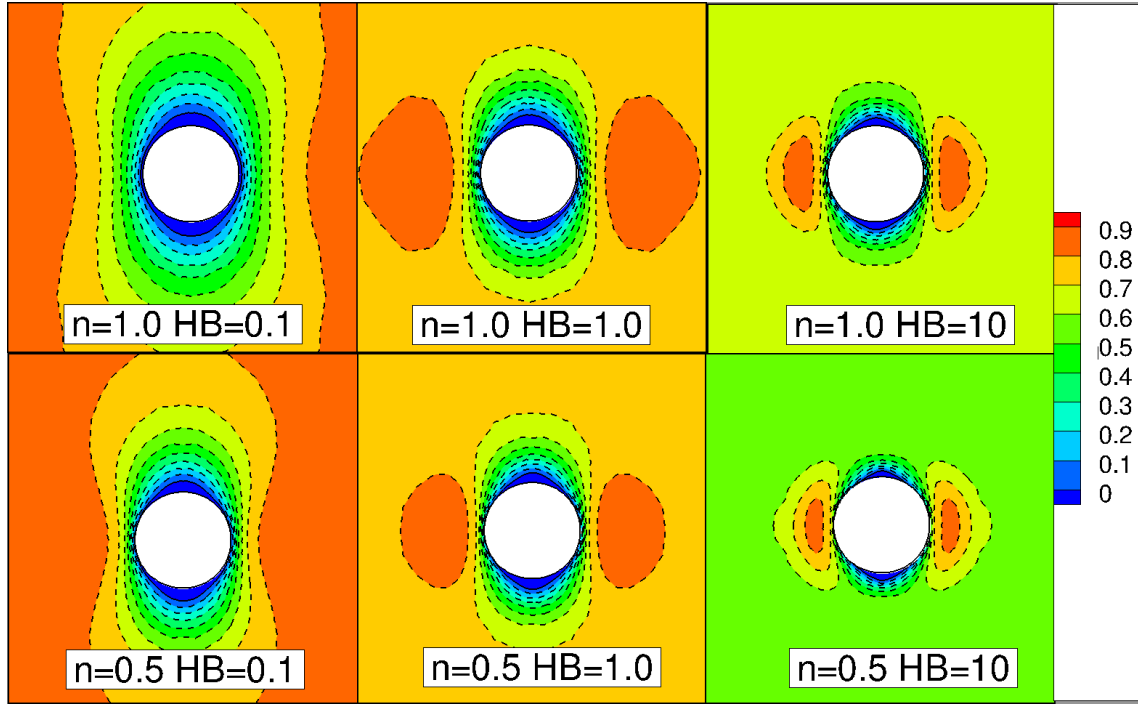


Figure 5.5: Contour of y - component of velocity that represents the yielded and the unyielded regions for $n = 1.0$ and $n = 0.5$ for various HB covered in this study.

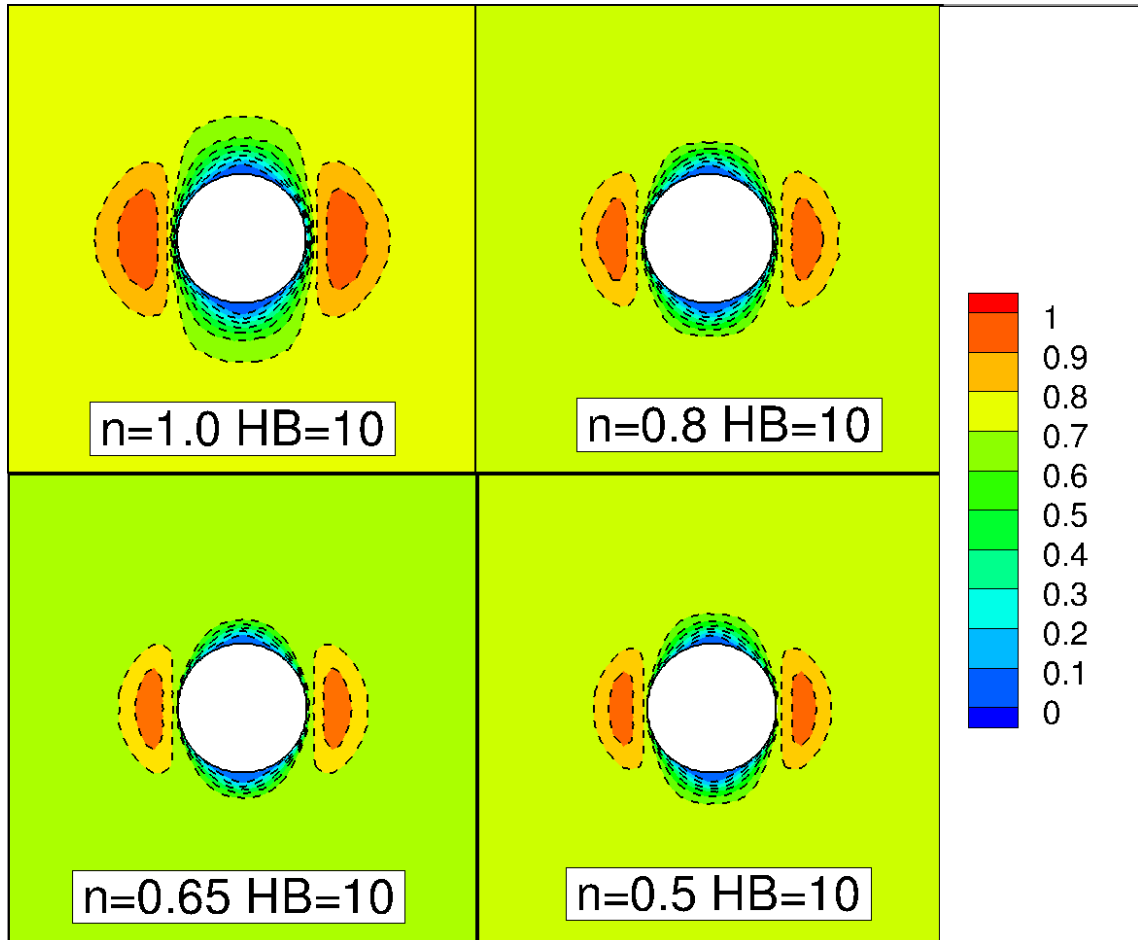


Figure 5.6: Contour of y - component of velocity that represents the yielded and the unyielded regions for range of n covered in this study at $HB = 10$.

Therefore, it is evident that the size of the unyielded region around the particle surface decreases as HB and n decreases. However, the most interesting part is that, in our study, when we apply shear, that is, $\delta' = \epsilon > 0$, the unyielded region disappears and increase the viscous deformation throughout the fluid domain.

5.4.2 Flow field for sheared settling

For a fluid with yield stress, the flow field in unsheared settling shows unyielded and yielded region, as discussed in §5.4.1. When a particle settles under a sheared condition in the yield-stress fluid, the velocity field is not expected to have any apparent unyielded region due to the applied shear. In addition, we expect the region of unyielded zones would disappear as we impose shear (for any value of $\delta' > 0$). In this section, we demonstrate the flow field for Bingham and shear-thinning fluids using a range of yield stress values.

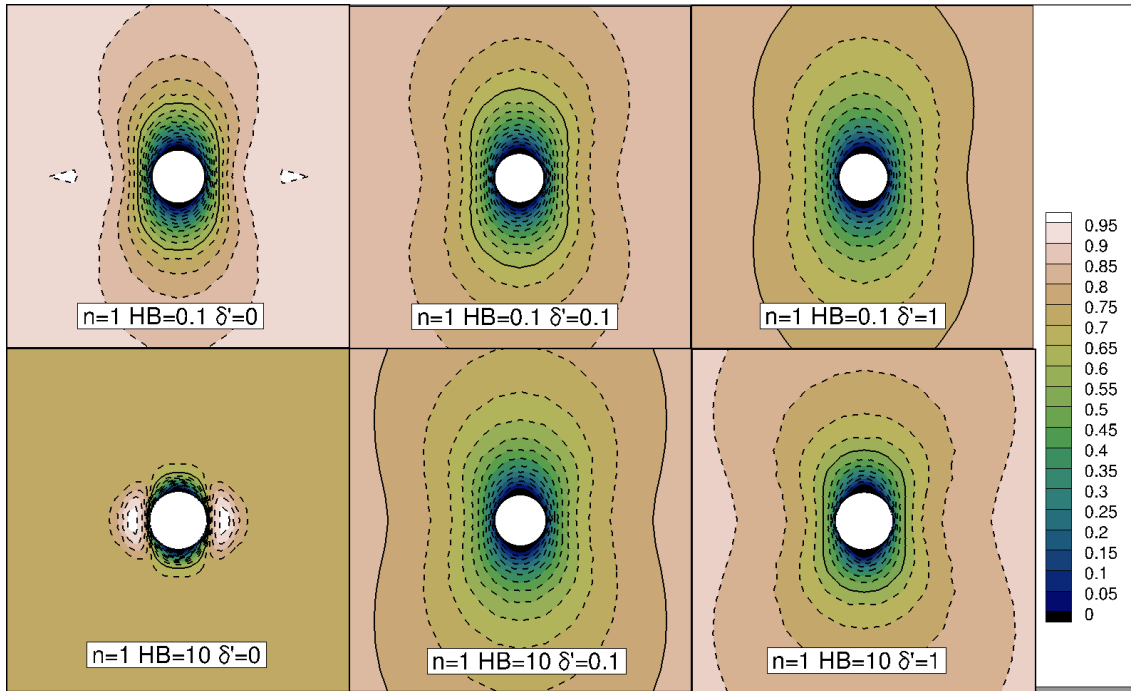


Figure 5.7: Contour of y - component of velocity for Bingham fluids for $0 \leq \delta' \leq 1$ at $HB=0.1$ and 10 .

As soon as the imposed shear of δ' is non-zero, we observe that the region of unyielded zone disappears. This is because the applied shear affects the viscous stress throughout the fluid domain.

At a low flow index, it is interesting to examine the variation in flow fields between unsheared and sheared condition. Two things may be observed in Figure 5.8, a) at a low

HB (here HB=0.1) there is no unyielded zone in the unsheared case and b) gradually, the unyielded zone grows as the yield stress of the fluid increases (see left bottom figure - $n=0.5$, HB=10, and $\delta' = 0$).

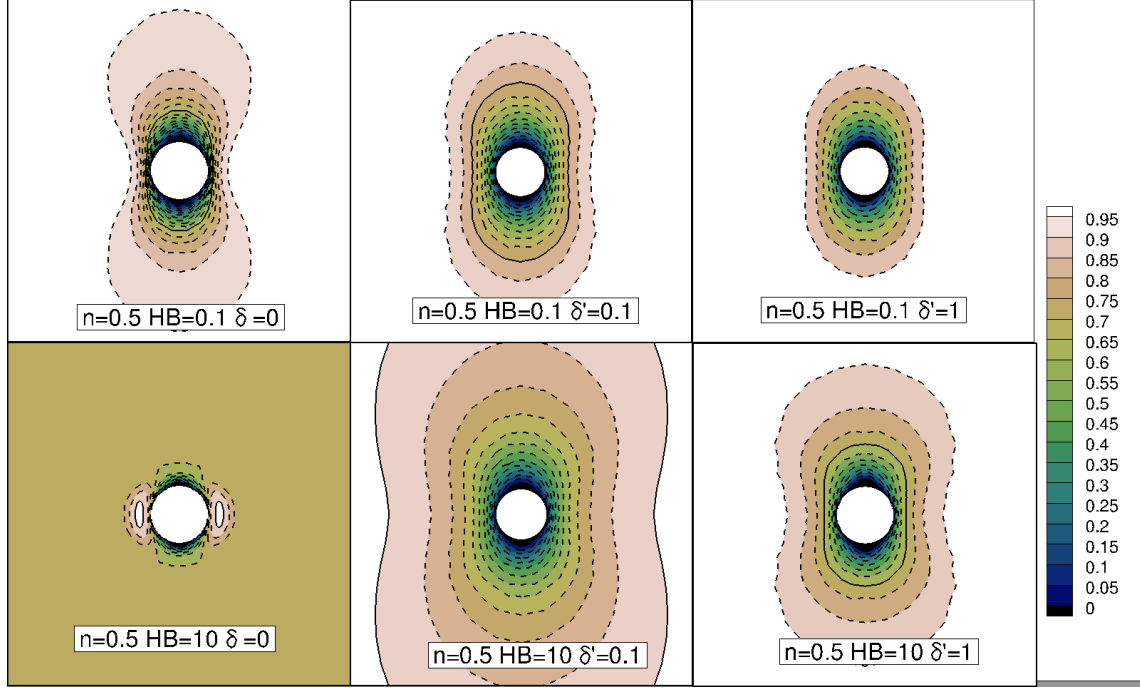


Figure 5.8: Contour of y - component of velocity for $n=0.5$ for $0 \leq \delta' \leq 1$ at HB=0.1 and 10.

5.5 Results

In our investigation, particle settling is quantified under an unsheared and a sheared conditions. Firstly, we illustrate the unsheared particle behaviour for a range of yield stresses in a fluid. We then compare with the data that is available in the literature on creeping flow. Secondly, we analyse the particle settling under imposed shear. The imposed shear significantly influences the particle settling, the effect of imposed shear is quantified and also, investigate the flow field of velocity and viscosity contours for a range of n , Herschel–Bulkley numbers (HB) and imposed shears (δ') covered in this study.

5.5.1 Unsheared settling

A particle can settle under gravity when $Y \leq 1/21 (\sim 0.048)$. In a creeping flow ($Re \ll 1$), we observe the drag force increase for increasing yield-stress in a fluid. As expected, the particle settles more slowly as HB increases.

In order to examine the unsheared case, 168 simulations were run that covered a range of n ($n = 0.5, 0.65, 0.8, \text{ and } 1$), HB ($HB = 0.1, 0.5, 1, 2, 5, \text{ and } 10$) and Re ($Re = 0.001 - 1.0$).

Figure 5.9 represents the unsheared data in terms of X/X_{Un} for the range of HB and n covered in this study. It is found that the value of X/X_{Un} is the same for all Re ($Re = 0.001 - 1.0$). Therefore, X/X_{Un} is not a function of Re over the range of Re covered in this study.

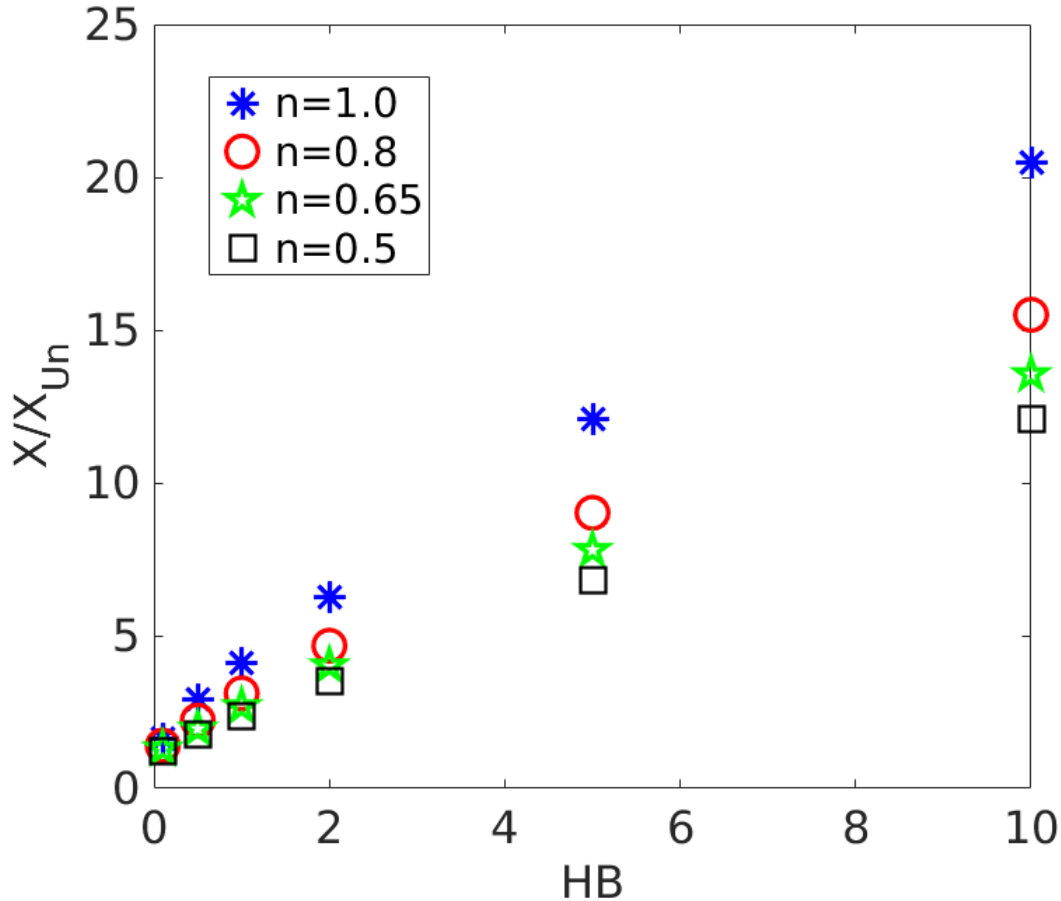


Figure 5.9: Unsheared settling for various n and HB represented in terms of X/X_{Un}

Ansley and Smith (1967b) proposed the value of drag coefficient for unsheared settling in creeping flow regime. It is given by the product of power-law drag co-efficient

($C_D = 24X_{Un}/Re$) and $(1 + a HB)$. The value of ‘a’ to be $7\pi/24 \sim 0.916$ for Bingham fluids (Ansley and Smith (1967b)) and 0.823 for Herschel–Bulkley fluids (Tabuteau *et al.* (2007a)).

From the scaling, $(1 + HB)$ was initially formulated to express our data. It has been found that the slope varies for each n . Hence, the functional form was modified to $(1 + a n HB)$. From our data, we also noticed that the behaviour of X/X_{Un} with HB appeared slightly concave upward and hence, in the functional form, $HB^{constant}$ was intended. Therefore, the final functional form used to represent unsheared settling was $(1 + a n HB^b)$. Using our computational measurements and non-linear regression fit, we obtain the value of empirical constants ‘a’ and ‘b’. The unsheared data fit in Equation 5.12 is in excellent agreement with our numerical measurements. As can be seen from Figure 5.10, the numerical measurements are represented by an asterisk (*) and the model fit, which is (Equation 5.12) represented by solid lines. Therefore, for shear-thinning yield stress fluids, we express the drag coefficient as $24X_{Un}(1 + a n HB^b)/Re$. It has been found that this is the best form that predicts the drag on the sphere for the various HB that have been covered in this study as its accuracy in predicting our data was above 97 % ($R^2 = 0.97$). A comparison between the predicted and actual values of X/X_{Un} is shown in Figure 5.11.

$$X/X_{Un} = (1 + a n HB^b) \quad (5.12)$$

where $a = 2.793$ and $b = 0.8404$

5.6 Drag prediction for sheared settling

When $\delta' \neq 0$, we represent the drag as X/X_{Un} , that is, a function of δ' and other parameters such as Re , n , and HB . When we analyse the data, we observe that the drag coefficients or X/X_{Un} appear to be a constant for the range of Re that is covered in this study within the minimum permissible range. Therefore, we consider $X/X_{Un} = f(n, \delta', HB)$; hence, X/X_{Un} is considered a constant for $0.001 \leq Re \leq 1$, as can be seen in Figure 5.13 and 5.14.

As per the scaling analysis, the dependency of the settling rate is assumed to be of the form, $(1 + a n HB^b)(1 + c\delta'^d)$. The first term in the form, $(1 + a n HB^b)$, was chosen because when $\delta' = 0$, the model asymptotes to unsheared settling prediction (Equation 5.12). The

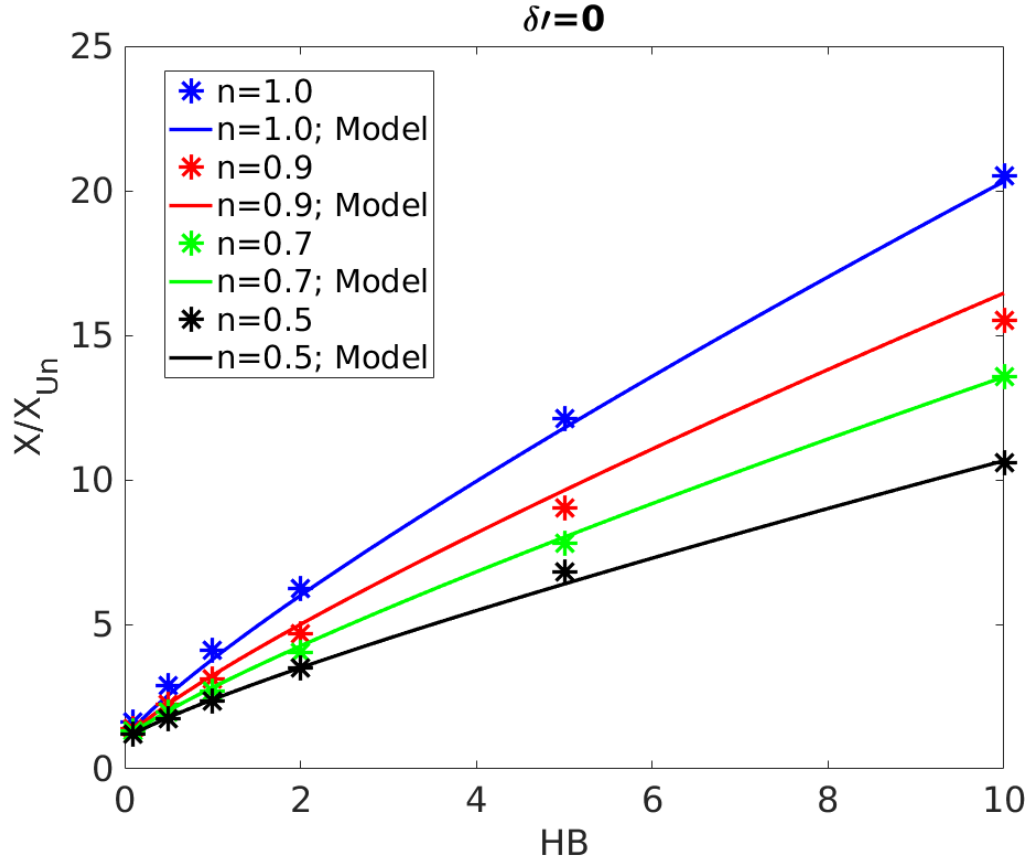


Figure 5.10: Comparison between model in Equation 5.12 and calculated data(*)

second term in the form, $(1+c\delta'^d)$ was chosen from the total shear rate scale. The constants 'c' and 'd' were introduced to improve the accuracy. We use the non-linear regression fit to provide a prediction that accurately predicts the drag on a sphere at different imposed shears. The resulting equation is given in Eqn 5.13, which predicts the observed data with an accuracy of 96 % ($R^2 = 0.96$). The comparison between the predicted and the actual values of X/X_{Un} is shown in Figure 5.12. Therefore, the final expression for C_D is given in Equation 5.14. The final step of consolidating the whole range of 680 data points that was valid for $0.001 \leq Re \leq 1$ constitutes in concisely providing a functional form that allows precise predictions, as in Equation 5.13 and 5.14.

$$X/X_{Un} = (1 + a n HB^b)(1 + c\delta'^d) \quad (5.13)$$

$$C_D = \frac{24}{Re} X_{Un} (1 + a n HB^b)(1 + c\delta'^d) \quad (5.14)$$

a=2.793, b=0.84, c=-0.5 and d=0.258

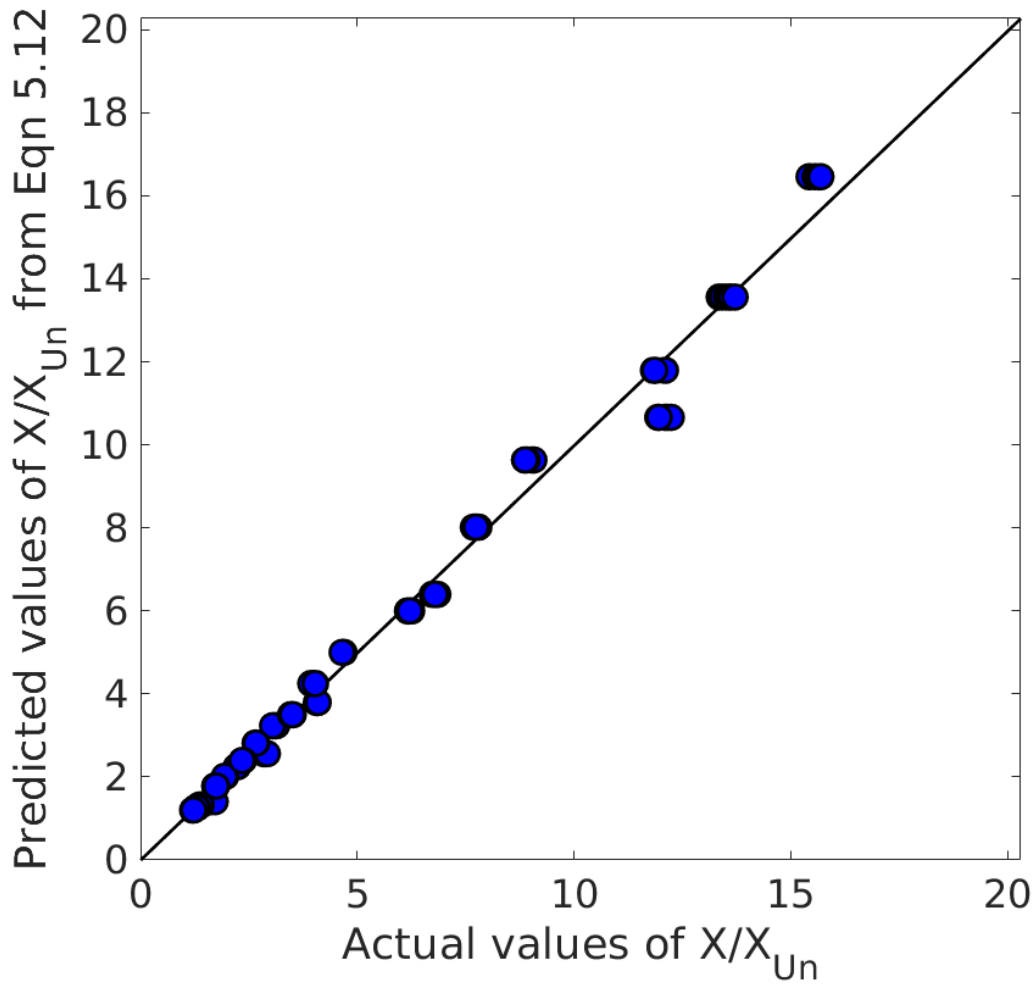


Figure 5.11: Predicted values of X/X_{Un} from Equation 5.12 versus actual values of X/X_{Un}

From the model that is obtained using the non-linear regression fit for sheared settling, which is given in Equation 5.13, we compare with our numerical measurements. This comparison is expected to show a good agreement between the calculated data and the model. However, it is much more interesting to observe the behaviour of the model for a range of different parameters covered in this study.

Firstly, we begin by examining as a function of Re for various HB . For $\delta' = 0.1, 0.5$ and 1.0 , the value of X/X_{Un} against the range of Re shows consistent agreement, as can be seen in Figure 5.13 and 5.14.

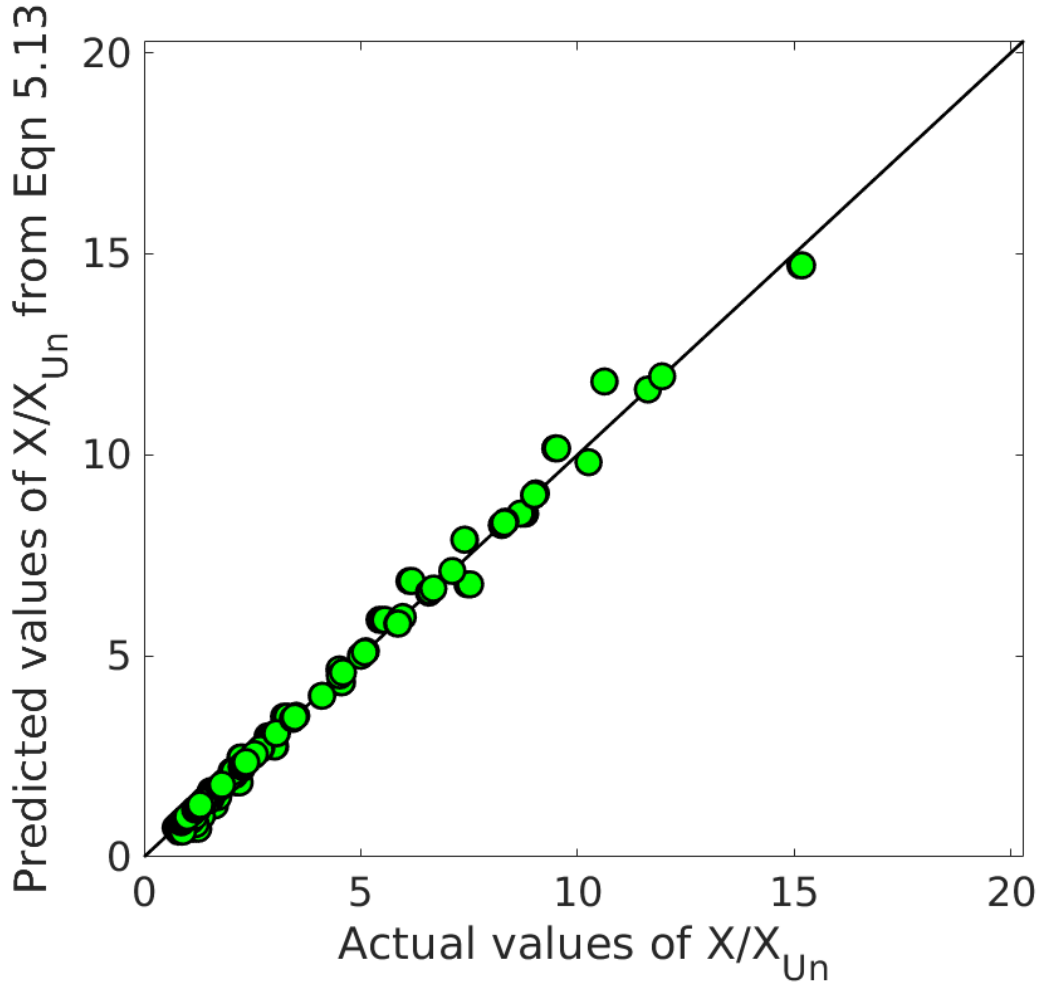


Figure 5.12: Predicted values of X/X_{Un} from Equation 5.13 versus actual values of X/X_{Un}

5.7 Drag variation in terms of imposed shear

We now examine the behaviour of the model with the data as a function of δ' . As expected, the value of X/X_{Un} decreases as the values of imposed shear increase. We begin by considering Bingham fluids ($n=1.0$). For various HB, in Figure 5.15, we clearly see a trend of decreasing drag force, which is as expected.

For shear-thinning fluids ($n < 1$), the value of X/X_{Un} is examined as function of δ' . The trend is similar for all other flow indices covered in this study. The variation of X/X_{Un} with δ' is shown for $n = 0.8, 0.65$, and 0.5 . For various HB, in Figures 5.15, the drag decreases as δ' increases for all Re covered in this study.

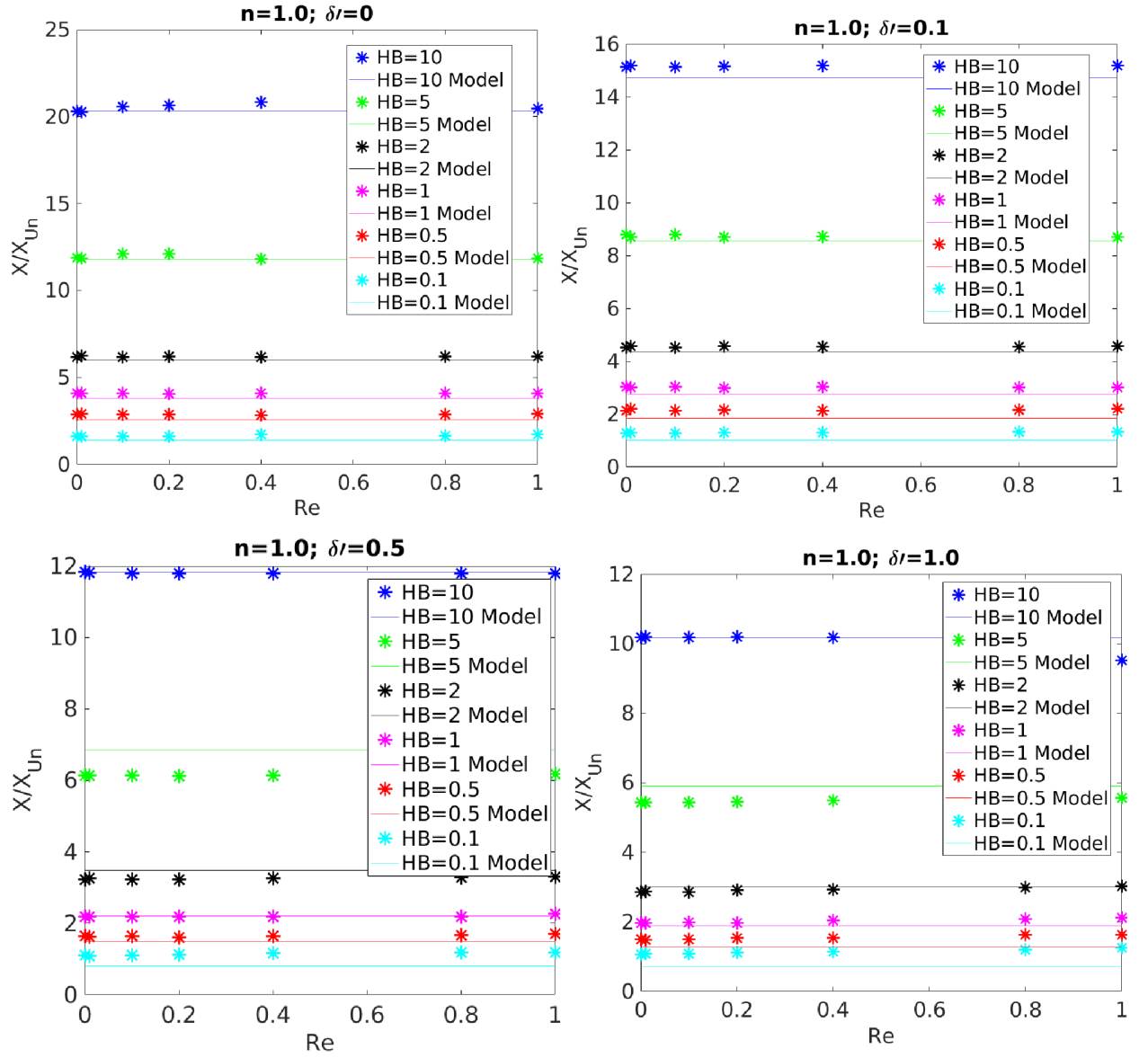


Figure 5.13: Comparison between calculated data of X/X_{Un} and prediction model using Equation 5.13 for $n = 1.0$, various HB and $\delta l'$

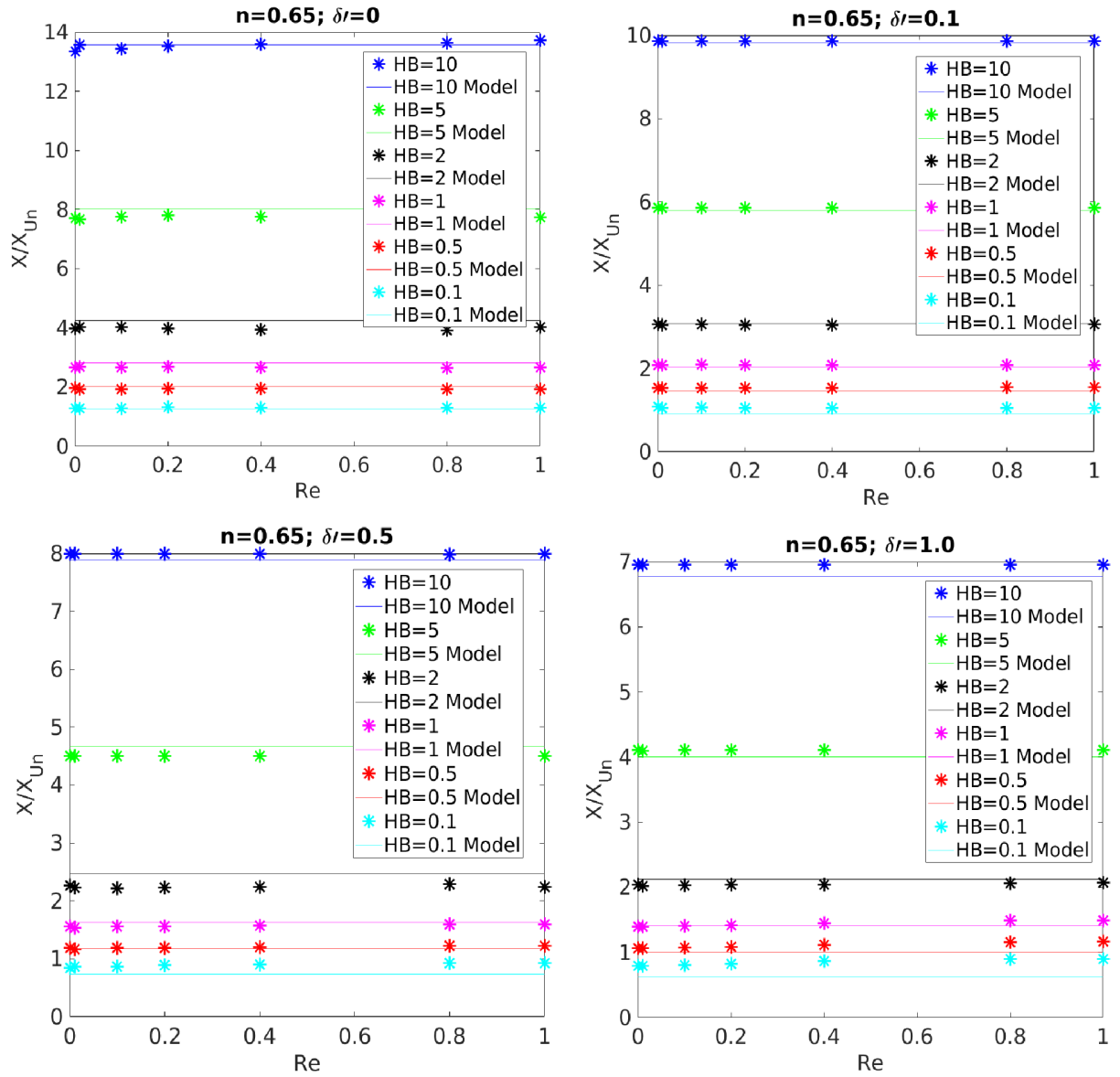


Figure 5.14: Comparison between calculated data of X/X_{Un} and prediction model using Equation 5.13 for $n = 0.65$ and various HB and δl

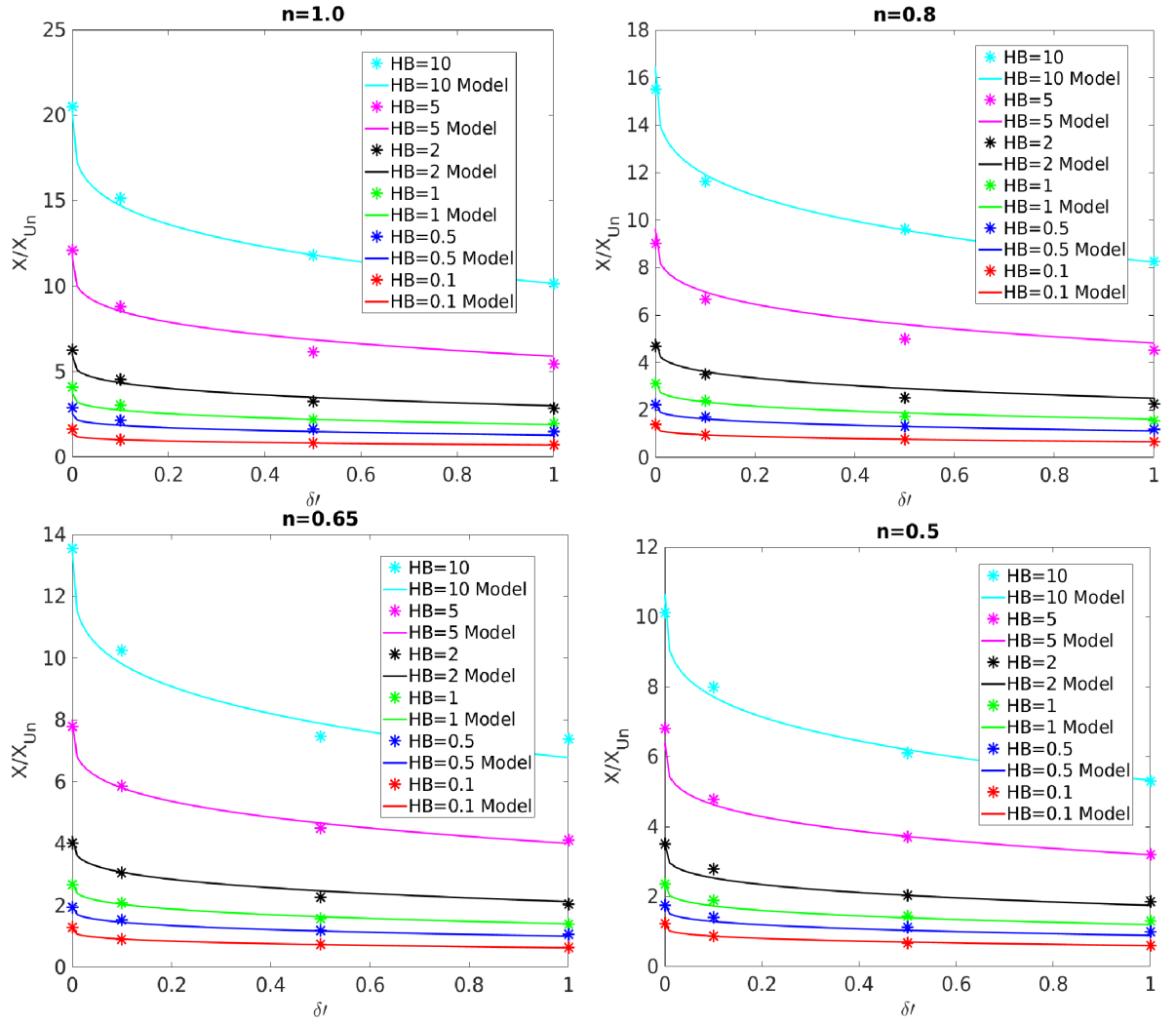


Figure 5.15: X/X_{Un} versus $\delta\tau$ for $0.1 \leq HB \leq 10$ for $n=1.0, 0.8, 0.65$, and, 0.5

5.8 Drag variation in terms of Herschel–Bulkley number

For a given n , for $0.1 \leq \delta' \leq 1$ and $0.1 \leq HB \leq 10$, we investigate the value of X/X_{Un} . The increase in the value of δ' implies that the imposed shear at each stage increases. At a high value of the yield stress, the settling rate decreases for a given δ' . The prediction was begun by the break down of the results from unsheared settling to settling under the maximum applied shear that is covered in this study, that is, $\delta' = 0-1.0$. From unsheared settling ($\delta' = 0$) to sheared settling, we can clearly observe that the value of X/X_{Un} gradually decreases as n decreases and as δ' increases. This phenomenon can be observed in Figure 5.16.

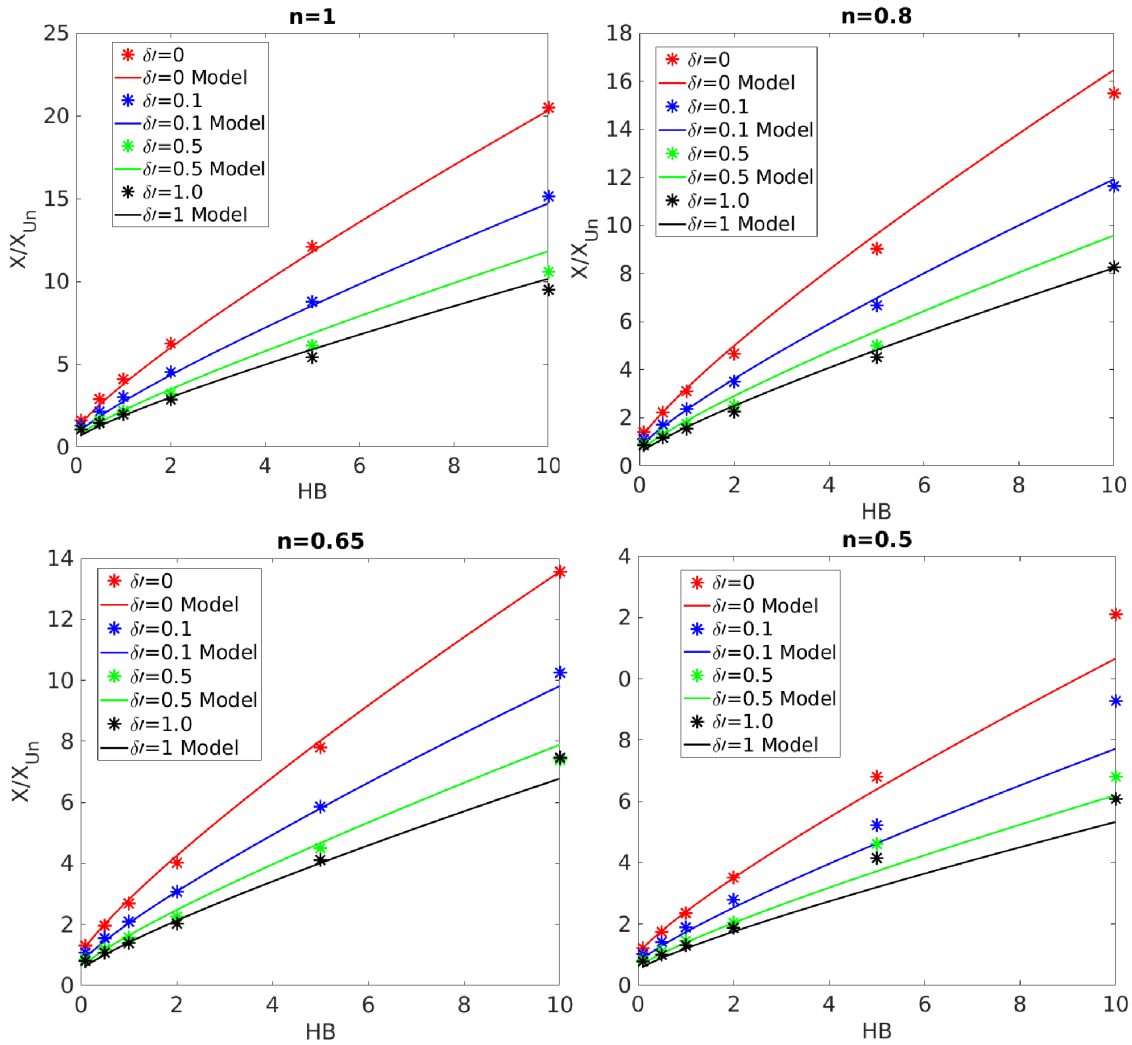


Figure 5.16: X/X_{Un} versus HB for various δ' and n

5.9 In terms of flow index

It was shown from the previous sections that for increasing imposed shear the drag reduces. However, the effect of n for a given imposed shear needs to be investigated. For various HB, we observe that as flow index n decreases the drag decreases. The dependency on n is not strong over $0.5 \leq n \leq 1$ when HB is small. This phenomenon can be observed in Figure 5.18. We also notice that for a given δ' , the slope gets steeper as HB increases. For this reason, the form: $(1 + a n HB^b)$ is used as the best estimation for the prediction of unsheared settling.

5.10 Comparison with power-law results

When power law results (that is, when HB=0) is included to the yield stress fluids, we observe a non-linear trend line between $\log HB$ and $\log X/X_{Un}$ as can be seen in Figure 5.17. The drag behavior cuts off into two different slopes at high HB and low HB. Due to this, the expression for predicting yield stress results (Eqn 5.14) does not asymptote to power-law results.

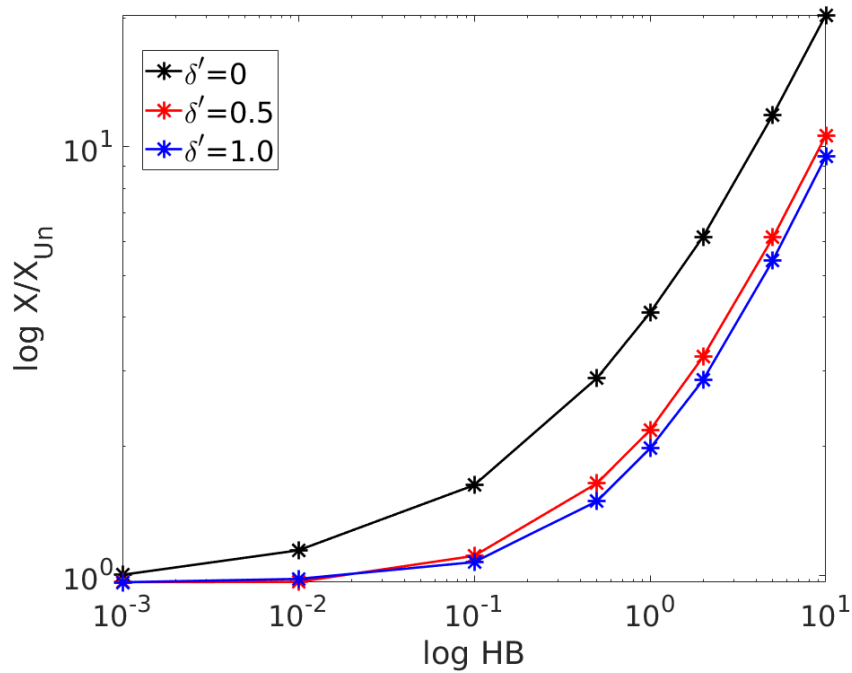
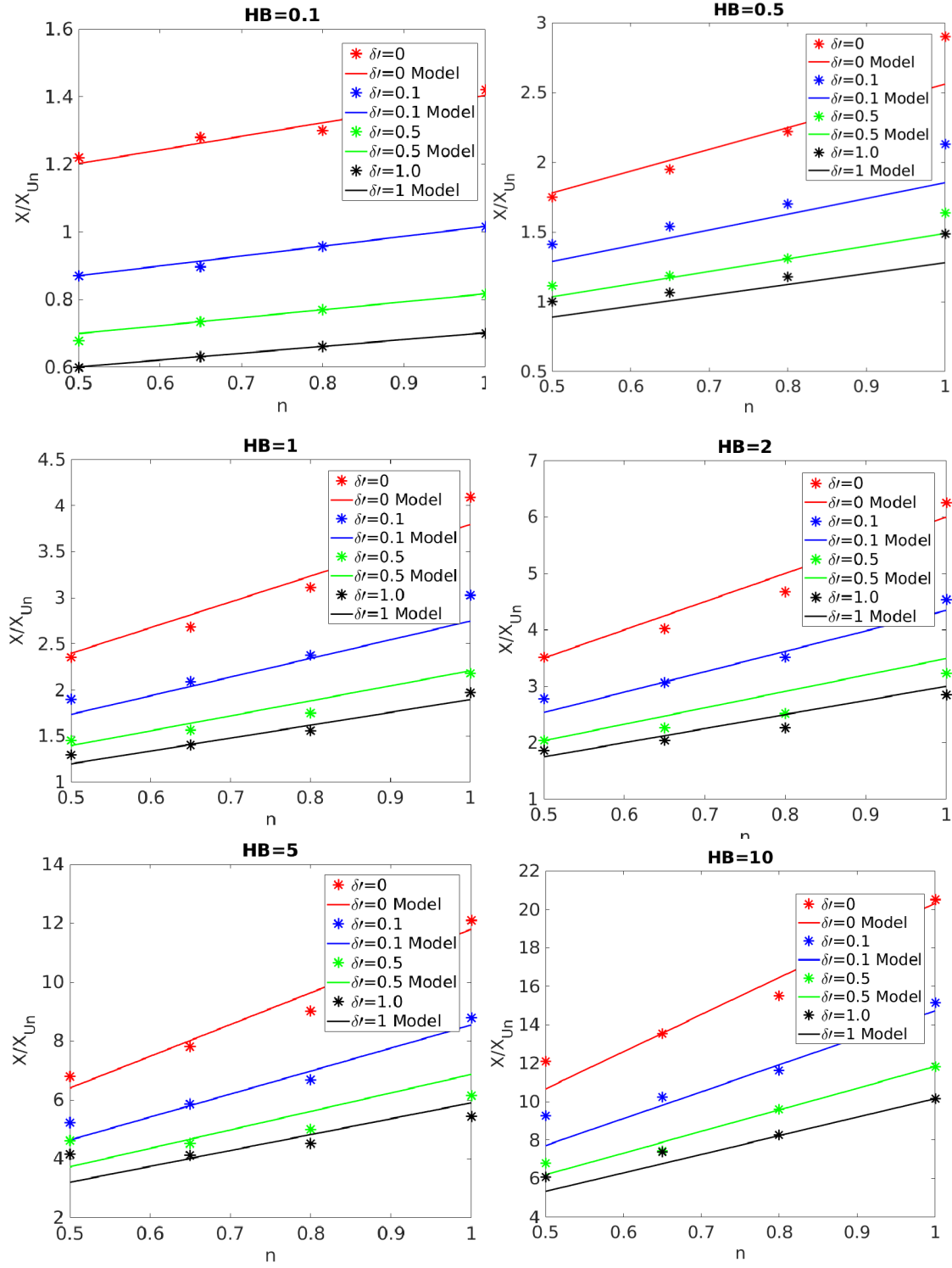


Figure 5.17: $\log HB$ versus $\log X/X_{Un}$ for $n=1$ and $\delta' = 0 - 1$

Figure 5.18: X/X_{Un} versus n for $0 \leq \delta\gamma \leq 1$ at various HB

5.11 Summary

In this chapter, the unsheared and sheared settling behaviour of a particle in shear-thinning yield-stress fluids was investigated. This part of the study began with a domain independence study to provide a solution that was equivalent to the unbounded medium. It was found that the ratio of the domain size to the particle diameter needed to be greater than 20. In addition, other grid-controlling parameters such as the number of particle surface elements and the number of layers around the surface of the particle were maintained same as power-law fluids. Therefore, the domain independence study was conducted, and a cost-effective mesh was developed.

Firstly, in unsheared particle settling, in some cases, the yield-stress property of the fluid suspends the particle and it stays embedded in the fluid. In this case, the particle weight was low and could not overcome the yield stress of the fluid. Therefore, a critical condition accounted for when the particle is still. The critical particle size for a given yield stress was presented in the literature using experimental methods (Atapattu *et al.* (1995b), Equation 5.2) and analytical approaches (Dedegil (1987), Equation 5.1). From our numerical approach, it was found that the criterion that was proposed by Atapattu *et al.* (1995b) matched with ours. A method to determine the critical particle size or a critical density difference for a given particle size was discussed in detail.

Secondly, we examined the flow field for particle under the sheared and the unsheared conditions. For the unsheared settling, the size of the unyielded region decreased as n decreased and increased as HB increased. For the sheared settling, it was observed that the unyielded zone disappeared at an increasing imposed shear and that the zone did not exist at low HB or in fluids that were close to power-law fluids.

Finally, we quantify the settling results. To represent yield stress results, it was found that apart from Re and n , two more dimensionless parameter Herschel–Bulkley number (HB) and Yield-gravity number (Y), were required to quantify the yield stress of the fluid and the particle-fluid density, respectively. The results of the particle settling in unsheared conditions were obtained and validated against Tabuteau *et al.* (2007a) and experimental measurements of the sheared case (conducted by CSIRO). After successful validation of the model, we proceeded to investigate a range of parameters Re , HB, n , and δ' . The effect of shear that is imposed on the particle was examined, and a model was proposed

to predict the total drag force that acts on the particle. An expression for C_D , as given in Equation 5.14 with empirical fitting constants that fit the range of Re ($0.001 \leq Re \leq 1$), HB ($0.1 \leq HB \leq 10$), $0.5 \leq n \leq 1.0$ and $0 \leq \delta' \leq 1$ that was covered in this study was proposed.

Chapter 6

Conclusions and Future Work

IN this study, a CFD model in OpenFOAM was developed. Along with the CFD model, a newly developed numerical algorithm was combined in such a way that the model could identify the rotation and the settling rate of a particle in non-Newtonian fluids. The model was validated by comparing it with the previously published predictions for particle settling in unsheared non-Newtonian fluids (power-law and yield stress fluids). After rigorous validation for the unsheared case in power-law fluids using works by Dhole *et al.* (2006), Graham and Jones (1994) and Dazhi and Tanner (1985) and in Herschel–Bulkley fluids using work by Tabuteau *et al.* (2007b) was considered. In the model developed for sheared case, shear was applied by adding a planar shear boundary condition. A review of the literature showed that little or no quantitative experimental data was available to validate the model in the sheared case. However, the model was validated against the available analytical solution for sheared power-law fluids under negligible inertial effects Childs (2013) and our model showed good agreement with Childs (2013). In yield-stress fluids, the model was validated using experimental measurements (conducted by CSIRO, Australia) in a purpose-built shear rig. Predictions of the settling rate by the CFD model were compared to the experiments by CSIRO and found that the measurements matched well, and the difference percentage fall within 10 %. Once the confidence in the model is developed, useful predictions about the flow behaviour in different cases was presented in two parts for power-law and Herschel–Bulkley fluids.

Firstly, predictions for particle settling in power-law fluids for $Re \leq 1$ were proposed that includes the unsheared and the sheared conditions. The predictions for particle settling in power-law fluids were presented in two different ways by using different scale

factor to non-dimensionalise the imposed shear, that is, δ (= applied shear/ unsheared settling shear rate = $\frac{2W/D}{V_U/d}$) and δ' (= applied shear/ sheared settling shear $\frac{2W/D}{V_{Sh}/d}$). Using δ , the prediction was made in terms of ratio of the sheared settling velocity to the unsheared settling velocity V_{Sh}/V_U , as shown in Equation 6.1. It was observed that the ratio is a strong function of δ and n . Additionally, the ratio was only a weak function of Re . Using δ' , the prediction was made in terms of dimensionless numbers such as C_D , Re and n . The drag coefficient is scaled with Stokes drag coefficient to obtain X , that is equal to C_D/C_{St} . Also, drag correction factor, $X_{Un} = f(n)$ was incorporated to present our results. The mechanism to represent drag coefficients in terms of ' X_{Un} ' was obtained from Dazhi and Tanner (1985); it was subsequently used to present our results in terms of imposed shear δ' . Although the values of X_{Un} that was given by Dazhi and Tanner (1985) and our results agreed with a maximum difference of $\sim 5.06\%$ between them, we presented the values of X_{Un} (in Table 4.2) that were more close to our model's prediction for accuracy. The final functional form in Equation 6.2 combines all the different conditions ($\delta' = 0, \delta' \neq 0, n = 1$, and $n \neq 1$) that were considered in this study and provided an accurate prediction. A maximum of 5.32% difference was found between the two predictions in Equation 6.1 and 6.2 for power-law fluids.

$$\boxed{\frac{V_{Sh}}{V_U} = (1 + 0.003\delta)(1 + 1.56\delta)^{(1-n)} \quad Re \leq 1} \quad (6.1)$$

$$\boxed{C_D = \frac{24}{Re} X_{Un} (1 + A' Re^B) (1 + Re\delta')^b (1 + \beta\delta')^{((n-1)/2)} \quad Re \leq 1} \quad (6.2)$$

$A' = 0.06 n^{4.947}, B = 1.6, b = 0.05$, and β in Table 4.4

Secondly, predictions for particle settling in the Herschel–Bulkley fluids for $Re \leq 1$ were proposed. A wide range of parameters (Re , HB , n , and δ') were investigated. The effect of imposed shear was examined, and our model predicts the force that acts on the particle from which the total drag is identified. An expression for C_D , as given in Equation 6.3, with empirical fitting constants that fit the range of Re ($0.001 \leq Re \leq 1$), HB ($0.1 \leq HB \leq 10$), $0.5 \leq n \leq 1.0$ and $0 \leq \delta' \leq 1$ that was covered in this study was proposed.

$$\begin{aligned}
C_D &= \frac{24}{Re} X_{Un} (1 + a n H B^b) (1 + c \delta'^d) & Re \leq 1 \\
a &= 2.793, b = 0.84, c = -0.5, \text{ and } d = 0.258
\end{aligned}
\tag{6.3}$$

In summary, predictions were made for unsheared and sheared settling in the power-law and yield stress for $Re \leq 1$. These predictions have implications in settling time and more importantly, in the settling distance that is required for a homogeneous coarse particle suspension to become stratified.

6.1 Future work

Although shear-induced settling in power-law and yield-stress fluids has been explored to understand the changes in their flow behaviour, future research directions to understand sheared settling are discussed in the section below.

6.1.1 New rheology models

Although sheared settling in non-Newtonian fluids, the rheology of which is fitted by the power-law and Herschel–Bulkley fluid has been examined in this PhD, the investigation of sheared settling using more recent rheology models such as Carreau model and Cross model that claim to predict fluid rheology with greater accuracy would be a significant contribution.

6.1.2 Orientation of planar shear/ geometry

To address the problem of a large particle in viscoplastic fluids, future research aims to investigate the effect of particle settling when the orientation of the applied shear changes (planar shear), that is, along the Y-plane.

6.1.3 Volume-fraction of solids

While this study has examined a single isolated particle settling in sheared non-Newtonian fluids, there is still a vast gap in the understanding of particle interaction and the effect of volume fractions of solids that are of practical relevance.

6.1.4 Unsteady flows

While the current study has examined some of the possibilities of steady state sheared settling, further study is required to gain a understanding of unsteadiness in sheared flows. There is a vast gap in the understanding of the possible mechanisms for unsteady sheared flows that would aid in designing the transportation of multi-phase mixtures in a pipeline or an open channel.

Appendices

Appendix A

Appendix A

A.1 Expression for V_{Sh} for power-law fluids

In this section, an approach to obtain an expression for settling rate from the C_D , Re , and δ' correlation is described. The drag coefficient is given by $F_D/(1/2)\rho V_{Sh}^2 \pi r^2$. In steady state, the drag force F_D is equal to the buoyancy, $4/3\pi r^3 \Delta \rho g$. When we substitute the value of F_D with buoyancy, we get the expression for C_D , as shown in Equation A.1. Additionally, from the sheared settling in power-law fluids study, an expression for the prediction of drag was proposed (discussed in Chapter 4, Eqn 4.26). We equate the Equations A.1 and A.2 to obtain an implicit expression for predicting particle settling rate V_{Sh} in sheared power-law fluids, as can be seen in Equation A.9.

$$\begin{aligned} C_D &= \frac{4/3\pi r^3 \Delta \rho g}{1/2 \rho V_{Sh}^2 \pi r^2} \\ &= \frac{4 \Delta \rho g d}{3 \rho V_{Sh}^2} \end{aligned} \quad (A.1)$$

$$C_D = \frac{24}{Re} X_{Un} (1 + A' Re^B) (1 + Re \delta')^b (1 + \beta \delta')^{((n-1)/2)} \quad (A.2)$$

Equating Eqn A.1 and Eqn A.2, we get

$$\frac{4 \Delta \rho g d}{3 \rho V_{Sh}^2} = \frac{24}{Re} X_{Un} (1 + A' Re^B) (1 + Re \delta')^b (1 + \beta \delta')^{((n-1)/2)} \quad (A.3)$$

On re-arranging and replacing Re with $\rho V_{Sh}^{2-n} d^n / k$, we get

$$\Delta \rho g d = \frac{18kX_{Un}(1 + A'Re^B)(1 + Re\delta')^b(1 + \beta\delta')^{(n-1)/2}}{V_{Sh}^{-n}d^n} \quad (A.4)$$

$$V_{Sh}^{-n} = \frac{18kX_{Un}(1 + A'Re^B)(1 + Re\delta')^b(1 + \beta\delta')^{(n-1)/2}}{\Delta \rho g d^{n+1}} \quad (A.5)$$

Say,

$$X_1 = (1 + A'Re^B) = 1 + A'(V_{Sh}^{2-n}d^n\rho/k)^B \quad (A.6)$$

$$X_2 = (1 + Re\delta')^b = (1 + (V_{Sh}^{2-n}d^n\rho/k)\delta')^b \quad (A.7)$$

$$X_3 = (1 + \beta\delta')^{(n-1)/2} = (1 + \beta\frac{2W/D}{V_{Sh}/d})^{(n-1)/2} \quad (A.8)$$

Then,

$$V_{Sh} = \left[\frac{\Delta \rho g d^{n+1}}{18kX_{Un}X_1X_2X_3} \right]^{1/n} \quad (A.9)$$

A.2 Expression for V_{Sh} for Herschel–Bulkley fluids

A similar approach that was carried out for power-law fluids was used here in Herschel–Bulkley fluids to obtain an expression for settling rate prediction under sheared conditions. We consider the expression for drag coefficient as described in previous section §A.1, Equation A.10 and the proposed drag correlation for Herschel–Bulkley fluids as discussed in Chapter 5, Eqn 5.14. When we equate these equations as shown below in Equations A.10 and A.11, we get an implicit expression for determining the particle settling rate V_{Sh} , as can be seen in Equation A.16.

$$C_D = \frac{4 \Delta \rho g d}{3\rho V_{Sh}^2} \quad (A.10)$$

$$C_D = \frac{24}{Re} X_{Un}(1 + a n HB^b)(1 + c\delta'^d) \quad (A.11)$$

a=2.793, b=0.84, c=-0.5 and d=0.258

$$\frac{4 \Delta \rho g d}{3 \rho V_{Sh}^2} = \frac{24}{Re} X_{Un} (1 + a n H B^b) (1 + c \delta'^d) \quad (A.12)$$

$$V_{Sh}^{-n} = \frac{18k}{\Delta \rho g d^{n+1}} X_{Un} (1 + a n H B^b) (1 + c \delta'^d) \quad (A.13)$$

Say,

$$C_1 = (1 + a n H B^b) \quad (A.14)$$

$$C_2 = (1 + c \delta'^d) \quad (A.15)$$

Then,

$$V_{Sh} = \left[\frac{\Delta \rho g d^{n+1}}{18k X_{Un} C_1 C_2} \right]^{1/n} \quad (A.16)$$

A.3 Matlab code to determine V_{Sh} implicitly

From C_D, Re, δ' correlation described in Chapter 4, an implicit expression for settling rate was derived, as shown in Equation A.9. To determine V_{Sh} implicitly, matlab code was used. The code is elaborated here for $n=0.5$.

```

d=0.001;
k=0.1;
rho=1000;
del_rho=1000 m1=(d^n * rho)/k;
n = 0.5; xun = 1.461; vun = (del_rho * 9.81 * d^(n + 1))/(18 * k * xun);
A = 0.06 * n^4.947;
B = 1.6;
b = 0.05;
beta = 17.25;
p = 2 - n;
p1 = (n - 1)/2;
for i = 1 : 12

```

```

vguess = vg(i);
vsh(i) = 0;
vun = vu(i);
wall = W(i);
fcn = @(v)(v - (vun/((1 + A * (vp * m1)B)). * ((1 + ((vp * m1 * wall)/(15 * v)))b) * ((1 + beta *
(wall/(15 * v)))p1)))));
v = fzero(fcn, vun);
vsh(i) = v
end

```

A.4 Sample calculation to calculate $\Delta\rho$

A typical example of the determining of the critical particle size or critical particle density is explained here. For the fluid rheology $\tau_y = 0.1$, $k=0.1$, $n=0.3$ and $d= 1$ mm, the extrapolated drag force for $V_U = 0$ is $1.1396e^{-6}$. The calculation to determine the critical $\Delta\rho$ is shown below.

$$\begin{aligned}
 F_D &= F_B \\
 &= \pi/6d^3\Delta\rho g
 \end{aligned}$$

$$\Delta\rho_{critical} = 219.94kg/m^{-3} \quad (A.17)$$

Similarly the experimental criterion from the Equation 5.2 is used to find the critical $\Delta\rho$.

$$\Delta\rho_{critical} = \frac{21\tau_y}{d g} = 214kg/m^{-3} \quad (A.18)$$

We clearly see from Equations A.17 and A.18, that the percentage difference falls within 3% and, hence, it can be said that the critical criterion provided by Jossic and Magnin (2009) and Tabuteau *et al.* (2007a) compares well with our results and has reasonable accuracy.

References

- , 1980, “Wall effect for high reynolds number motion of spheres in shear thinning fluids,” *Chemical Engineering Communications* **5**, 115–124.
- Ahonguio, F., Jossic, L., and Magnin, A., 2014, “Influence of surface properties on the flow of a yield stress fluid around spheres,”
- Alehossein, H., Shen, B., Qin, Z., and Huddleston-Holmes, C., 2012, “Flow analysis, transportation, and deposition of frictional viscoplastic slurries and pastes in civil and mining engineering,” *Journal of Materials in Civil Engineering* **24**, 644–657.
- Andres, 1961, “Equilibrium and motion of spheres in a viscoplastic liquid,” *Soviet Physics Doklady* **5**, 723–730.
- Ansley, R. W., and Smith, T. N., 1967a, “Motion of spherical particles in a bingham plastic,” *AIChE Journal* **13**, 1193–1196.
- Ansley, R. W., and Smith, T. N., 1967b, “Motion of spherical particles in a bingham plastic,” *AIChE Journal* **13**, 1193–1196.
- Astruc, M., Vervoort, S., Nouatin, H., Coupeuz, T., De Puydt, Y., Navard, P., and Peuvrel-Disdier, E., 2003, “Experimental and numerical study of the rotation and the erosion of fillers suspended in viscoelastic fluids under simple shear flow,” *Rheologica Acta* **42**, 421–431.
- Atapattu, D., Chhabra, R., and Uhlherr, P., 1995a, “Creeping sphere motion in herschel-bulkley fluids: flow field and drag,” *Journal of Non-Newtonian Fluid Mechanics* **59**, 245 – 265.

- Atapattu, D., Chhabra, R., and Uhlherr, P., 1995b, "Creeping sphere motion in herschel-bulkley fluids: flow field and drag," *Journal of Non-Newtonian Fluid Mechanics* **59**, 245 – 265.
- Avino, G. D., and Maffettone, P., 2015, "Particle dynamics in viscoelastic liquids," *Journal of Non-Newtonian Fluid Mechanics* **215**, 80 – 104.
- Bakker, C., Meyer, C., and Deglon, D., 2009, "Numerical modelling of non-newtonian slurry in a mechanical flotation cell," *Minerals Engineering* **22**, 944 – 950.
- Bartosik, A., 2010 Mar, "Application of rheological models in prediction of turbulent slurry flow," *Flow, Turbulence and Combustion* **84**, 277–293.
- Beaulne, M., and Mitsoulis, E., 1997, "Creeping motion of a sphere in tubes filled with herschel–bulkley fluids," *Journal of Non-Newtonian Fluid Mechanics* **72**, 55 – 71.
- Beris, A. N., Tsamopoulos, J. A., Armstrong, R. C., and Brown, R. A., 1985, "Creeping motion of a sphere through a bingham plastic," *Journal of Fluid Mechanics* **158**, 219–244.
- Blackery, J., and Mitsoulis, E., 1997, "Creeping motion of a sphere in tubes filled with a bingham plastic material," *Journal of Non-Newtonian Fluid Mechanics* **70**, 59 – 77.
- Boardman, G., and Whitmore, R., 1961, "The static measurement of yield stress," *Laboratory Practice* **10**, 782–785.
- Brookes, and Whitmore, R. L., 1969, "Drag forces in bingham plastics," *Rheologica Acta*, Band 8 Heft 4
- Brookes, G., and Whitmore, R., 1968, "The static drag on bodies in bingham plastics," *Rheologica Acta* **7**, 188–196.
- Burgos, G. R., and Alexandrou, A. N., 1999, "Flow development of herschel-bulkley fluids in a sudden three-dimensional square expansion," *Journal of Rheology* **43**, 485–498.
- Chhabra, R. P., Tiu, C., and Uhlherr, P. H. T., 1980, "Shear-thinning effects in creeping flow about a sphere," in *Rheology: Volume 2: Fluids*, edited by Astarita, G., Marrucci, G., and Nicolais, L. (Springer US, Boston, MA). ISBN 978-1-4684-3743-0, pp. 9–16.

- Chhabra, R. P., Comiti, J., and Machač, I., 2001, “Flow of non-newtonian fluids in fixed and fluidised beds,” *Chemical Engineering Science* **56**, 1 – 27.
- Chhabra, R., 2006, *Bubbles, Drops, and Particles in Non-Newtonian Fluids*, 2nd ed. (Taylor & Francis, Boca Raton).
- Childs, L. H., 2013 9, *Low Reynolds number flows of generalized non-Newtonian fluids*, Ph.D. thesis (University of Bristol).
- Cho, Y., and Hartnett, J., 1983, “Drag coefficients of a slowly moving sphere in non-newtonian fluids,” *Journal of Non-Newtonian Fluid Mechanics* **12**, 243 – 247.
- Clift, R. R., Grace, j. a., John R, and Weber, j. a., Martin E, 1978, *Bubbles, drops, and particles* (New York ; London : Academic Press). ISBN 012176950X
- Coleman, I. B. C. U. G. P. J. R. C. J. F. H., and Raad, P. E., 2008, “Procedure for estimation and reporting of uncertainty due to discretization in cfd applications,” *Journal of Fluids Engineering* **130**, 078001–078001.
- Coussot, P., Laigle, D., Arattano, M., Deganutti, A., and Marchi, L., 1998, “Direct determination of rheological characteristics of debris flow,” *Journal of Hydraulic Engineering* **124**, 865–868.
- Dazhi, G., and Tanner, R., 1985, “The drag on a sphere in a power-law fluid,” *Journal of Non-Newtonian Fluid Mechanics* **17**, 1 – 12.
- Dedegil, M. Y., 1987, “Drag coefficient and settling velocity of particles in non-newtonian suspensions,” *Journal of Fluids Engineering* **109**, 319–323.
- Dennis, S. C. R., and Walker, J. D. A., 1971, “Calculation of the steady flow past a sphere at low and moderate reynolds numbers,” *Journal of Fluid Mechanics* **48**, 771–789.
- Dhole, S. D., , Chhabra, R. P., and Eswaran, V., 2006, “Flow of power-law fluids past a sphere at intermediate reynolds numbers,” *Ind. Eng. Chem. Res.* **45**, 4773–4781.
- Dou, H.-S., Khoo, B. C., and Yeo, K. S., 2007, “Turbulent transition in plane couette flows,” in *Proceedings of the Fifth International Conference on Fluid Mechanics*, edited by Zhuang, F. and Li, J. (Tsinghua University Press, Springer-Verlag, Shanghai).

- Einstein, A., 1906, “Eine neue bestimmung der moleküldimensionen,” *Ann. Phys.* **19**, 289 – 306.
- Einstein, A., 1911, “Berichtigung zu meiner arbeit: Eine neue bestimmung der moleküldimensionen,” *Ann. Phys.* **34**, 591 – 592.
- Ezekiel, E. E., and Akpabio, J. U., 2014, “Particle settling in power law fluids,” *Elixir Petrol. Engg* **76**, 28733–28739.
- Felice, R. D., and Parodi, E., 1996, “Wall effects on the sedimentation velocity of suspensions in viscous flow,”
- Frey, S., Link, F. B., Naccache, M. F., and Fonseca, C., 2016 Apr, “Finite element investigation of inertia and viscous effects on regularized herschel–bulkley flows,” *Journal of the Brazilian Society of Mechanical Sciences and Engineering* **38**, 1291–1298.
- Gavrilov, A. A., Finnikov, K. A., and Podryabinkin, E. V., 2017 Apr, “Modeling of steady herschel–bulkley fluid flow over a sphere,” *Journal of Engineering Thermophysics* **26**, 197–215.
- Gheissary, G., and van den Brule, B., 1996, “Papers presented at the workshop on ‘unresolved experimental dilemmas in the dynamics of complex fluids’ unexpected phenomena observed in particle settling in non-newtonian media,” *Journal of Non-Newtonian Fluid Mechanics* **67**, 1 – 18.
- Godinez, F. A., de la Calleja, E., Lauga, E., and Zenit, R., 2014, “Sedimentation of a rotating sphere in a power-law fluid,” *Journal of Non-Newtonian Fluid Mechanics* **213**, 27 – 30.
- Graham, D., and Jones, T., 1994, “Settling and transport of spherical particles in power-law fluids at finite reynolds number,” *Journal of Non-Newtonian Fluid Mechanics* **54**, 465 – 488.
- Greco, F., D’Avino, G., and Maffettone, P., 2007, “Rheology of a dilute suspension of rigid spheres in a second order fluid,” *Journal of Non-Newtonian Fluid Mechanics* **147**, 1 – 10.

- Gumulya, M., Horsley, R., and Wilson, K., 2007, "The settling of consecutive spheres in viscoplastic fluids," *International Journal of Mineral Processing* **82**, 106 – 115.
- Horsley, M., Horsley, R., Wilson, K., and Jones, R., 2004, "Non-newtonian effects on fall velocities of pairs of vertically aligned spheres," *Journal of Non-Newtonian Fluid Mechanics* **124**, 147 – 152.
- Jossic, L., and Magnin, A., 2009, "Drag of an isolated cylinder and interactions between two cylinders in yield stress fluids," *Journal of Non-Newtonian Fluid Mechanics* **164**, 9 – 16.
- Kelessidis, V. C., 2004, "An explicit equation for the terminal velocity of solid spheres falling in pseudoplastic liquids," *Chemical Engineering Science* **59**, 4437 – 4447.
- Kelessidis, V., and Mpandelis, G., 2004, "Measurements and prediction of terminal velocity of solid spheres falling through stagnant pseudoplastic liquids," *Powder Technology* **147**, 117 – 125.
- Koziol, K., and Glowacki, P., 1988, "Determination of the free settling parameters of spherical particles in power law fluids," *Chemical Engineering and Processing: Process Intensification* **24**, 183 – 188.
- Lali, A., Khare, A., Joshi, J., and Nigam, K., 1989, "Behaviour of solid particles in viscous non-newtonian solutions: Settling velocity, wall effects and bed expansion in solid-liquid fluidized beds," *Powder Technology* **57**, 39 – 50.
- Laruccia, M., Santana, C., and Maidla, E., 1990, "Velocity of variously shaped particles settling in non-newtonian fluids," *Advances in Fine Particles Processing*, 103–119.
- Liu, B. T., Muller, S. J., and Denn, M. M., 2003, "Interactions of two rigid spheres translating collinearly in creeping flow in a bingham material," *Journal of Non-Newtonian Fluid Mechanics* **113**, 49 – 67.
- MacSporran, W., 1986, "Direct numerical evaluation of shear rates in concentric cylinder viscometry," *J. Rheology* **30**, 125–132.
- McLaughlin, J. B., 1991, "Inertial migration of a small sphere in linear shear flows," *Journal of Fluid Mechanics* **224**, 261–274.

- Mendes, P. R. S., and Dutra, E. S. S., 2019, “Viscosity function for yield-stress liquids,” *Applied Rheology* **14**, 296–302.
- Merkak, O., Jossic, L., and Magnin, A., 2006, “Spheres and interactions between spheres moving at very low velocities in a yield stress fluid,” *Journal of Non-Newtonian Fluid Mechanics* **133**, 99 – 108.
- Missirlis, K., Assimacopoulos, D., Mitsoulis, E., and Chhabra, R., 2001, “Wall effects for motion of spheres in power-law fluids,” *Journal of Non-Newtonian Fluid Mechanics* **96**, 459 – 471.
- Nguyen, Q., and Boger, D., 1998, “Application of rheology to solving tailings disposal problems,” *International Journal of Mineral Processing* **54**, 217 – 233.
- Nirmalkar, N., and Chhabra, R., 2014, “Momentum and heat transfer from a heated circular cylinder in bingham plastic fluids,” *International Journal of Heat and Mass Transfer* **70**, 564 – 577.
- Ovarlez, G., Bertrand, F., Coussot, P., and Chateau, X., 2012, “Shear-induced sedimentation in yield stress fluids,” *Journal of Non-Newtonian Fluid Mechanics* **177 - 178**, 19 – 28.
- Patel, S., and Chhabra, R., 2013, “Steady flow of bingham plastic fluids past an elliptical cylinder,” *Journal of Non-Newtonian Fluid Mechanics* **202**, 32 – 53.
- Putz, A. M. V., Burghilea, T. I., Frigaard, I. A., and Martinez, D. M., 2008, “Settling of an isolated spherical particle in a yield stress shear thinning fluid,” *Physics of Fluids* **20**, 033102.
- S. Caserta, S., D’Avino, G., Greco, F., Guido, S., and Maffettone, P. L., 2011, “Migration of a sphere in a viscoelastic fluid under planar shear flow: Experiments and numerical predictions,” *Soft Matter* **7**, 1100–1106.
- Saha, G., Purohit, N., and Mitra, A., 1992, “Spherical particle terminal settling velocity and drag in bingham liquids,” *International Journal of Mineral Processing* **36**, 273 – 281.

- Shi, F., and Napier-Munn, T., 1996, "A model for slurry rheology," *International Journal of Mineral Processing* **47**, 103 – 123.
- Slatter, P., 1997, "The rheological characterisation of sludges," *Water Science and Technology* **36**, 9 – 18.
- Snijkers, F., D'Avino, G., Maffettone, P., Greco, F., Hulsen, M., and Vermant, J., 2009, "Rotation of a sphere in a viscoelastic liquid subjected to shear flow. part ii. experimental results," *Journal of Rheology* **53**, 459–480.
- Snijkers, F., D'Avino, G., Maffettone, P., Greco, F., Hulsen, M., and Vermant, J., 2011, "Effect of viscoelasticity on the rotation of a sphere in shear flow," *Journal of Non-Newtonian Fluid Mechanics* **166**, 363–372.
- Sofrá, F., and Boger, D. V., 2002, "Environmental rheology for waste minimisation in the minerals industry," *Chemical Engineering Journal* **86**, 319 – 330.
- Song, D., and Gupta, R., 2009 06, "Wall effects on a sphere falling in quiescent power law fluids in cylindrical tubes," *Industrial Engineering Chemistry Research - IND ENG CHEM RES* **48**, doi:\bibinfo{doi}{10.1021/ie900176y}
- de Souza Mendes, P. R., 2007, "Dimensionless non-newtonian fluid mechanics," *Journal of Non-Newtonian Fluid Mechanics* **147**, 109 – 116.
- Tabuteau, H., Coussot, P., and de Bruyn, J. R., 2007a, "Drag force on a sphere in steady motion through a yield-stress fluid," *Journal of Rheology* **51**
- Tabuteau, H., Coussot, P., and de Bruyn, J. R., 2007b, "Drag force on a sphere in steady motion through a yield-stress fluid," *Journal of Rheology* **51**, 125–137.
- Taibi, H., and Messelmi, F., 2018, "Effect of yield stress on the behavior of rigid zones during the laminar flow of herschel-bulkley fluid," *Alexandria Engineering Journal* **57**, 1109 – 1115.
- Talmon, A. M., and Huisman, M., 2005, "Fall velocity of particles in shear flow of drilling fluids," *Tunneling and Underground Space Technology* **20**, 193–201.
- Taylor, G., 1923, "Stability of a viscous liquid contained between two rotating cylinders," *Philos. Trans. R. Soc. Lond. series A* **223**, 289–343.

- Tran, Q., and Horsley, R., 1993, "Drag coefficient and settling velocities of spheres in yield-pseudoplastic slurries," *Developments in Non-Newtonian Flows (ASME)* **175**, 131.
- Trevelyan, B., and Mason, S., 1951, "Particle motions in sheared suspensions. i. rotations," *Journal of Colloid Science* **6**, 354 – 367.
- Tripathi, A., Chhabra, R. P., and Sundararajan, T., 1994, "Power law fluid flow over spheroidal particles," *Industrial & Engineering Chemistry Research* **33**, 403–410.
- Turian, R. M., Attal, J. F., Sung, D.-J., and Wedgewood, L. E., 2002, "Properties and rheology of coal–water mixtures using different coals," *Fuel* **81**, 2019 – 2033.
- Valentik, L., and Whitmore, R. L., 1965, "The terminal velocity of spheres in bingham plastics," *British Journal of Applied Physics* **16**, 1197.
- V.Boger, D., 2013, "Rheology of slurries and environmental impacts in the mining industry," *Annual review of chemical and biomolecular engineering* **4**, 239–57.
- Wang, X.-m., Li, J.-x., Xiao, Z.-z., and Xiao, W.-g., 2004 Mar, "Rheological properties of tailing paste slurry," *Journal of Central South University of Technology* **11**, 75–79.
- Wasserman, M. L., and Slattery, J. C., 1964, "Upper and lower bounds on the drag coefficient of a sphere in a power-model fluid," *AIChE Journal* **10**, 383–388.
- WHITMORE, R. L., and BOARDMAN, G., 1962/04/21/online, "Yield stress exerted on a body immersed in a bingham fluid," *Nature Publishing Group* **194**
- Wilson, K., Horsley, R., Kealy, T., Reizes, J., and Horsley, M., 2003, "Direct prediction of fall velocities in non-newtonian materials," *International Journal of Mineral Processing* **71**, 17 – 30.
- Wilson, K. C., 2000, "Particle motion in sheared non-newtonian media," in *3rd Israeli Conference for Conveying and Handling of Particulate Solids* (Dead Sea, Israel). pp. 12.9–12.13.
- Zhu, H., Kim, Y., and Kee, D. D., 2005, "Non-newtonian fluids with a yield stress," *Journal of Non-Newtonian Fluid Mechanics* **129**, 177 – 181.